DEPARTMENT OF PHYSICS
UNIVERSITY OF JYVÄSKYLÄ
RESEARCH REPORT No. 8/2018

TRANSITION-EDGE SENSORS FOR PARTICLE-INDUCED X-RAY EMISSION SPECTROMETRY

BY

MARKO KÄYHKÖ

Academic Dissertation
for the Degree of
Doctor of Philosophy

To be presented, by permission of the
Faculty of Mathematics and Science
of the University of Jyväskylä,
for public examination in Auditorium FYS1 of the
University of Jyväskylä on August 22nd, 2018
at 12 o'clock noon

Jyväskylä, Finland
August 2018

ABSTRACT

Käyhkö, Marko
Transition-edge sensors for particle-induced X-ray emission spectrometry
Jyväskylä: University of Jyväskylä, 2018, 76 p. (+included articles)
Department of Physics Research Report No. 8/2018
ISSN 0075-465X
ISBN 978-951-39-7524-1 (paper copy)
ISBN 978-951-39-7525-8 (PDF)
Diss.

A transition-edge sensor array has been applied to particle-induced X-ray emission. We have characterized the detector for quantitative analysis and obtained minimum detection limit over two orders of magnitude better compared to a silicon drift detector. We have also studied chemical effects in analysis of Ti, TiO_2 and TiN using proton and heavy ion beams. A chemical shift for TiO_2 was observed in proton measurements, and relative multiple ionization X-ray satellite line intensities changed between metallic Ti and other compounds with heavy ions. Detection of low energy X-rays down to 0.5 keV was achieved by installing a polycapillary lens in front of the transition-edge sensor array in external beam measurement setup. We developed a software for TES data analysis, including features such as graphical user interface, automated energy calibration, fitting of high-resolution spectra, and quantitative elemental analysis.

Keywords: Particle-induced X-ray emission, Transition-Edge sensor, High energy resolution, Chemical speciation

Author
Marko Käyhkö
Department of Physics
University of Jyväskylä
Jyväskylä, Finland

Supervisor
Prof. Timo Sajavaara
Department of Physics
University of Jyväskylä
Jyväskylä, Finland

Supervisor
Dr. Kai Arstila
Department of Physics
University of Jyväskylä
Jyväskylä, Finland

Reviewers
Dr. Stjepko Fazinić
Rudjer Boskovic Institute
Zagreb, Croatia

Prof. Jyrki Räisänen
Department of Physics
University of Helsinki
Helsinki, Finland

Opponent
Dr. Primož Pelicon
Department of Low and Medium Energy Physics
Jožef Stefan Institute Reactor Center
Ljubljana, Slovenia

TIIVISTELMÄ (ABSTRACT IN FINNISH)

Transitioreunailmaisin (TES-ilmaisin) asennettiin hiukkasherätteisellä röntgenemis-siolla tehtäviä mittauksia varten. Olemme karakterisoineet ilmaisimen tehokkuuden kvantitatiivisia mittauksia varten ja saavuttaneet jopa kaksi kertaluokkaa paremman havaintoherkkyyden verrattuna pii-drift-ilmaisimeen (silicon drift detector). Tutkimme eri titaaniyhdisteiden, Ti, TiN ja TiO_2, vaikutusta röntgenspektriin käyttäen sekä protoni- että raskasionisuihkuja. Protonimittauksissa havaittiin kemiallinen energiasiirtymä TiO_2 yhdisteellä verrattuna metalliseen titaaniin, ja raskasionisuihkumittauksissa havaittiin eroavaisuuksia röntgenspetkrin hienorakenteessa (satelliittipiikeissä) metallisen titaanin ja muiden näytteiden välillä. Matalaenergisten röntgeneiden havaitseminen 0.5 keViin asti saavutettiin asentamalla polykapillaarilinssi transitioreunailmaisimen eteen ulkoisessa mittausasetelmassa. Kehitin ohjelmiston TES-datan analyysiä varten, mihin sisältyy graafinen käyttöliittymä, automaattinen energiakalibraatio, korkearesoluutioisten piikkien sovitus ja kvantitatiivinen alkuaineanalyysi.

PREFACE

The work presented in this thesis has been carried out at the Department of Physics, University of Jyväskylä, during the years 2014–2018.

I would like to thank my supervisors Prof. Timo Sajavaara, and Dr. Kai Arstila. I met first Timo at 2011 during the interview for internship at imec, Belgium, and during the interview Timo's enthusiasm to the field and positive attitude towards a young researcher became clear. Since, then we have been working together, and Timo has provided nessecary guidance needed for young researcher. I met Kai first time during my internship at imec. He was then a helpful assistance for me to get familiar with a new work environment. When I become a PhD student 2014, Kai had moved also to Jyväskylä and he becoming my second supervisor was a pleasant surprise. Even though, I have been more guided by Timo, Kai has also taught me many things and also together we have worked with IAEA project (F11019), which has been a nice experience for me.

I am also very grateful for Dr. Mikko Palosaari. During my first summer project in 2010, Mikko taught me how to work with different clean room tools, like uv-lithography and electron beam microscopy. The work was related to the properties of transition-edge sensors, absorber material, and was a good introduction to the field of TES. During my first years as a PhD student Mikko was my instructor for all things related to TES, and without his past work also my thesis would not be possibly.

I also want to thank our other current and past group members. Mikko Laitinen has been a great help in the laboratory both teaching me the use of an accelerator, and countless of practical things. I would also like to thank Jaakko Julin, Sami Kinnunen, Laura Mättö, and Mari Napari. In general, the atmosphere in the group, and in the whole department has been very good, and if some problems occur (like they usually do) there is always some willing to help with the issue.

Thanks for my friends and other colleagues. Especially Mikko Konttinen, Johannes Nokelainen, Teemu Parviainen and Sampsa Vihonen have been great friends outside the University, whether it is company for board games, disc golf, or gym etc.

Lastly I would like to thank my family. My parents have always encouraged to educate myself. And of course, I want to thank Hanna for her endless support and love.

Jyväskylä, August 2018,

Marko Käyhkö

The work presented in this thesis was supported by Academy of Finland Center of Excellence in Nuclear and Accelerator Based Physics (Ref. 251353) and Doctoral Programme in Nuclear and Particle Physics (University of Jyväskylä).

ACRONYMS AND NOMENCLATURE

ADR	Adiabatic demagnetization refrigerator
BPM	Beam profile meter
DFT	Density functional theory
ERDA	Elastic recoil detection analysis
PIXE	Particle-induced X-ray emission
RBS	Rutherford backscattering spectrometry
SEB	Secondary electron bremsstrahlung
SEM	Scanning electron microscope
SDD	Silicon drift detector
SQUID	Superconducting QUantum Interference Device
TES	Transition-edge sensor
WDX	Wavelength-dispersive X-ray detector
XANES	X-ray absorption near edge structure
XPS	X-ray photoelectron spectroscopy
XRF	X-ray fluorescence

LIST OF INCLUDED ARTICLES

PI M. R. J. Palosaari, M. Käyhkö, K. M. Kinnunen, M. Laitinen, J. Julin, J. Malm, T. Sajavaara, W. B. Doriese, J. Fowler, C. Reintsema, D. Swetz, D. Schmidt, J. N. Ullom, and I. J. Maasilta. Broadband Ultrahigh-Resolution Spectroscopy of Particle-Induced X Rays: Extending the Limits of Nondestructive Analysis. *Physical review applied - 6, 024002 (2016)*.

PII M. Käyhkö, M. R. J. Palosaari, M. Laitinen, K. Arstila, I. J. Maasilta, J. W. Fowler, W. B. Doriese, J. N. Ullom, T. Sajavaara. Minimum detection limits and applications of proton and helium induced X-ray emission using transition-edge sensor array. *Nucl. Instr. Meth B - 406 130–134 (2017)*.

PIII M. Käyhkö, M. R. J. Palosaari, M. Laitinen, K. Arstila, I. J. Maasilta, T. Sajavaara. Heavy ion induced Ti X-ray satellite structure for Ti, TiN, and TiO_2 thin films. *Submitted to X-ray spectrometry*.

PIV M. Käyhkö, M. Laitinen, K. Arstila, I. J. Maasilta, T. Sajavaara. A new beamline for energy-dispersive high-resolution PIXE analysis using polycapillary optics. *Submitted to Nucl. Inst. Meth. B*.

PI: The author was involved in the measurements, did part of the data analysis, and contributed writing the manuscript.

PII: The author did the measurements, data analysis and wrote the first version of the manuscript.

PIII: The author did the measurements, data analysis and wrote the first version of the manuscript.

PIV: The author did most of the work in building the new beamline, as well as did the measurements, data analysis and wrote the first version of the manuscript.

Additionally, outside the scope of this thesis, the author has contributed to the published work in Ref. [1].

CONTENTS

1 INTRODUCTION

The foundation for all X-ray methods began with the discovery of X-rays by W. Röntgen [2]. The importance of the finding was shortly acknowledged, and W. Röntgen was awarded with the very first Nobel prize in physics [3]. In total 15 Nobel prizes have been awarded for discoveries related to X-rays (7 in physics, 6 in chemistry and 2 in medicine), indicating the high importance of the field of X-ray physics [3]. The applications of X-rays are so numerous that it would be impossible to list them all.

In this thesis, characteristic X-rays of atoms are the subject of interest, more specifically characteristic X-rays induced via an ion beam, a technique known as particle-induced X-ray emission, PIXE. In 1906 characteristic X-rays were discovered by Barkla [4] (awarded with Nobel prize for the discovery in 1917). Characteristic X-rays are unique for each atom and can be thought of as a "fingerprint" of an atom. In 1922, Hadding was able to measure multiple elements for the first time by exciting atoms using an electron beam [5]. A big breakthrough for PIXE took place in 1970 when Johansson et al. [6] demonstrated the ability to distinguish neighboring elements using a lithium doped silicon, Si(Li), detector and a 2 MeV proton beam. Since then PIXE has been widely used over the world in wide range of fields including art and archaeology [7], biology [8], geology [9], air pollution [10] study et cetera [11].

High-resolution PIXE, referring to the detection of X-rays with energy resolution much better than 100 eV, is a less explored field of PIXE because of the limited availability of high-energy-resolution detectors. The higher energy-resolution reveals hidden details not visible in regular PIXE. In the simplest case, the hidden detail can be an unidentified element with characteristic X-rays too close to more intense X-ray peaks. In a more complex case, the high-resolution PIXE can provide a way to probe subtle changes between the same element in different chemical environments.

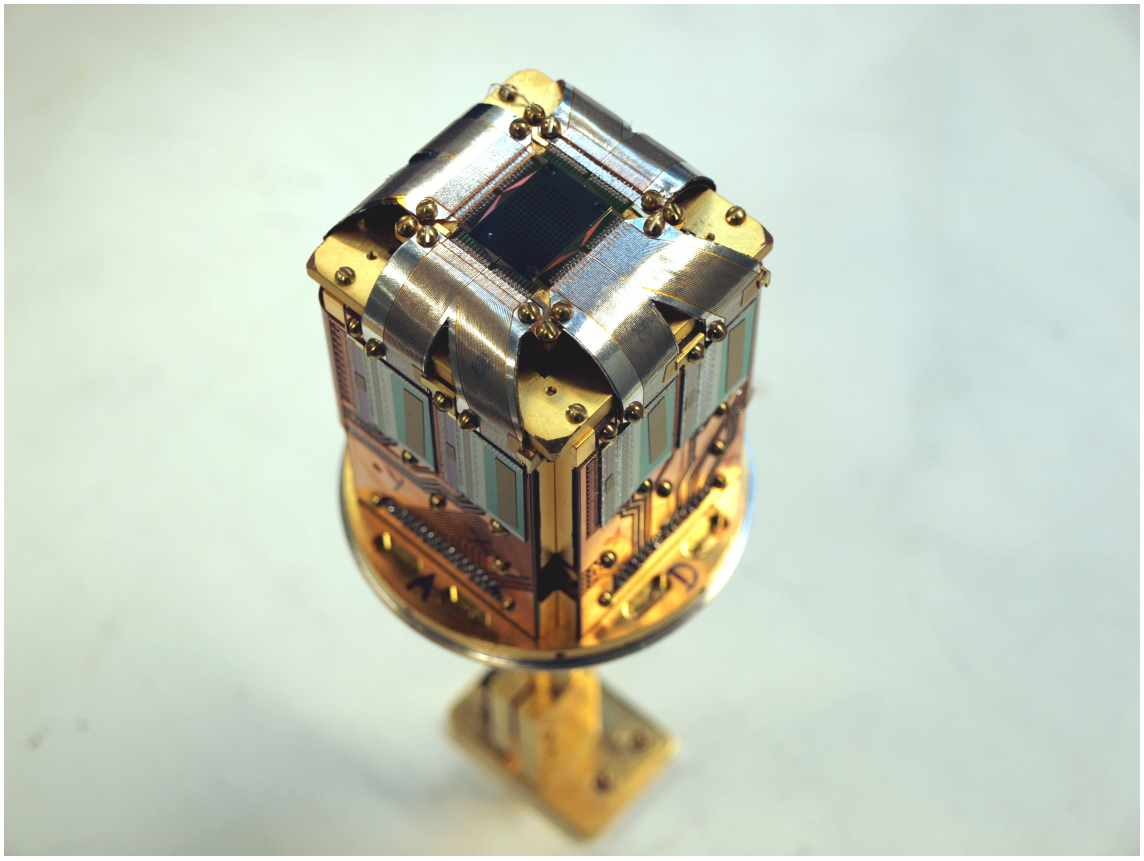

FIGURE 1 An image of the transition-edge sensor array at the University of Jyväskylä. Size of the whole detector complex is circa 5 cm x 5 cm. Image printed with permission from Mikko Palosaari.

One clear drawback of the high-resolution PIXE has been the lack of energy-dispersive detection. The energy-dispersive detector can be compared to a human eye. The human eye can simultaneously see all the colors of visible light, or sense different energies of photons to be more specific. The energy-dispersive detector does the same and can detect a wide range of the energy spectrum simultaneously. On the other hand, a wavelength-dispersive detector works differently, and it can only detect a very small portion of the energy spectrum at a time and works on a narrow energy region. Wavelength-dispersive detection is like being able to sense all the shades of blue with very high precision, but being blind to all other colors. In this thesis, I have used a high-energy resolution, energy-dispersive detector called transition-edge sensor (TES) array (see Fig. 1). TES array was incorporated to PIXE measurements in vacuum and in-air, its performance was quantified, and it was used to study chemical effects of different titanium-containing thin films.

2 X-RAY GENERATION AND INTERACTIONS WITH MATTER

X-rays are photons with higher energy than visible light or ultraviolet light. X-rays have typically energies between 100 eV and 150 keV. The photons with even higher energies are called gamma rays. The gamma rays are commonly defined to originate from nuclear transitions, and X-rays from atomic transitions or acceleration of charged particles, and there is some overlap in energy between X-rays and gamma rays. [12]

2.1 X-ray generation

In order to understand X-rays originating from the atomic transitions, one needs to understand electronic shell structure of atoms. All elements have a unique electronic shell structure with quantized energy levels. Each electron in the atom can be described with four (4) quantum numbers: principal quantum number (n=1, 2, 3,...), angular quantum number (ℓ=0, 1,..., n-1), magnetic quantum number (m=$-\ell$, $-\ell+1$,..., $\ell-1$, ℓ), and spin quantum number (s=$\pm\frac{1}{2}$). Furthermore, quantum numbers (ℓ) and (s) are often combined into total angular momentum quantum number ($|\ell - s| \leq j \leq |\ell + s|$). In practice instead of full quantum numbers different notations like the atomic notation or the X-ray notation are used. The equivalents of these three notations for the first 28 electrons are summarized in Table 1 [13].

TABLE 1 Comparison of different electron shell notations [13]. The first notation gives the principal quantum number (n), angular quantum number (ℓ), and total angular momentum quantum number (j). The spin quantum number has only a small effect on the energy levels and is not shown here. In the atomic notation, the angular quantum number is replaced with a letter (0=s, 1=p, 2=d, etc.). In the X-ray notation, the principal quantum number is replaced with a letter (1=K, 2=L, 3=M, etc.), and other quantum numbers are replaced with an integer with consecutive numbers.

$n\ell j$	atomic notation	X-ray notation
10(1/2)	$1s_{1/2}$	K1
20(1/2)	$2s_{1/2}$	L1
21(1/2)	$2p_{1/2}$	L2
21(3/2)	$2p_{3/2}$	L3
30(1/2)	$3s_{1/2}$	M1
31(1/2)	$3p_{1/2}$	M2
31(3/2)	$3p_{3/2}$	M3
32(3/2)	$3d_{3/2}$	M4
32(5/2)	$3d_{5/2}$	M5

2.1.1 Characteristic X-rays

A characteristic X-ray or an Auger electron is emitted when an electron from a higher energy shell transfers into a lower energy shell. This always requires an electron-hole in an inner electron shell which can occur, for example, by excitation with an energetic photon, electron or ion, or spontaneously by electron capture (see Fig. 2 for an illustration). If the excited atom has more than one electron-hole the emitted X-ray generates a satellite line or a hypersatellite line in the case of two K-shell electron-holes (for K-shell transitions) [13].

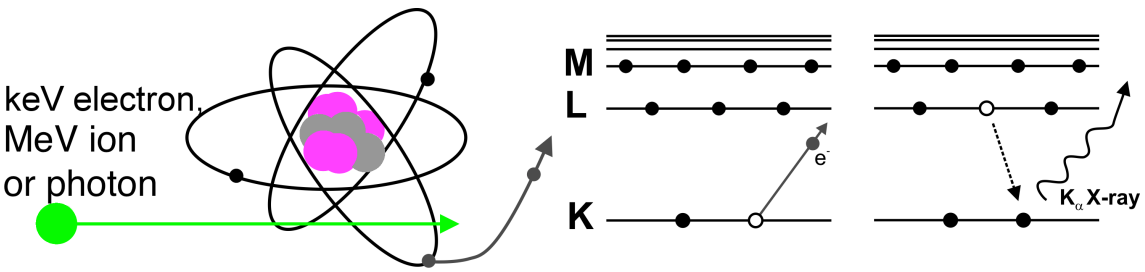

FIGURE 2 An illustration of a characteristic X-ray emission. An energetic particle (ion, electron), or a photon creates an electron-hole at K-shell, which is filled by an L-shell electron leading to emission of Kα X-ray (in this example).

TABLE 2 Different Siegbahn and IUPAC notations [13] are compared and relative intensities for silver within each shell are given [14].

Siegbahn notation	IUPAC notation	Relative intensity
$K\alpha_1$	KL2	100
$K\alpha_2$	KL3	53
$K\beta_3$	KM2	16
$K\beta_1$	KM3	9
$K\beta_2$	KM4 and KM5	4
$L\alpha_1$	L3M5	100
$L\alpha_2$	L3M4	11
$L\beta_1$	L2M4	56
$L\beta_3$	L1M3	
$L\beta_4$	L1M2	
$L\beta_2$	L3N5	13
$L\gamma_1$	L2N4	6
$L\gamma_3$	L1N3	
$L\iota$	L3M1	4
$M\alpha_1$	M5N7	
$M\alpha_2$	M5N6	
$M\beta$	M4N6	
$M\gamma$	M3N5	

The most probable transitions follow rules: $\delta n \neq 0$, $|\delta l| = 1$, $|\delta j| = 0, 1$ [12]. The first transition following the rules is L2→K1, which exists for elements with 5 electrons or more (boron or heavier). Transitions that do not follow aforementioned rules are called multipole lines or forbidden lines [13] but are rarely used in X-ray spectroscopy because of the low transition probabilities.

Characteristic X-ray transitions are marked most commonly with the Siegbahn notation or with the IUPAC notation [13]. In the Siegbahn notation, three characters are used to distinguish the transition; a capital letter (K, L, M, ...) indicating the shell with an electron-hole, a Greek letter ($\alpha, \beta, \gamma, \eta$) groups together transitions close each other in energy, and an integer number (1, 2, ...) specifies the exact transition. In the IUPAC notation, the X-ray notations (see Table 1) of electron-hole and the hole-filling electron are used to indicate the transition. The most common K-, L-, and M-shell transitions are marked with these two different notations in Table 2 [13].

2.1.2 Radiation emitted by a charged particle with changing velocity

When a charged particle, like a proton or an electron, is being accelerated it emits photons. The origin of this type of radiation is generally related into two different processes: synchrotron radiation, and Bremsstrahlung radiation. In synchrotron radiation, the charged particle is accelerated radially, and in Bremsstrahlung radiation the charged particle is deflected by the electric field of another charged particle. Synchrotron radiation, as the name implies, is most relevant in synchrotrons, and in this thesis, I will focus on Bremsstrahlung radiation.

Bremsstrahlung radiation is a form of radiation that spreads continuously in energy from zero to some maximal energy. It is known that the intensity of Bremsstrahlung is proportional to the acceleration of a moving particle to the second power [11]. For example as electrons and protons differ by the mass and sign of charge they experience equally strong Coulomb interaction, but they have different acceleration. Because a proton is approximately 1840 times heavier than an electron, it creates radiation that has almost 3 400 000 times lower intensity.

Intensity of the Bremsstrahlung radiation depends on the detection angle and follows equation

$$I = C\frac{\sin(\theta)^2}{(1-\beta\cos(\theta))^6}, \tag{1}$$

where C is a constant, θ is the detection angle and $\beta = {}^{v}/_{c}$ is the ratio of the velocity of the charged particle to the speed of light [12]. The detection angle is defined as the angle between the vector pointing from the particle to the detector, and the velocity vector of the particle.

2.2 Interactions of X-rays with matter

X-rays can be absorbed by the electrons in the atom. Atomic electrons are bound to the atom, but when given enough energy, they can be excited into free electrons, and this is called the photoelectric effect (illustarted in Fig. 3). The photoelectric effect can be written mathematically as

$$K_{max} = hf - W, \tag{2}$$

where K_{max} is the maximum kinetic energy of the ejected (photo)electron, hf is the energy of the incoming photon, and W is the minimum energy required to remove an electron. If $hf < W$, then photoelectric effect does not take place, since kinetic energy of the electron must be positive. The minimum energy required to remove the most loosely bound electron is so small for all elements, that the photoelectric effect takes place in all elements for X-rays. When the energy of

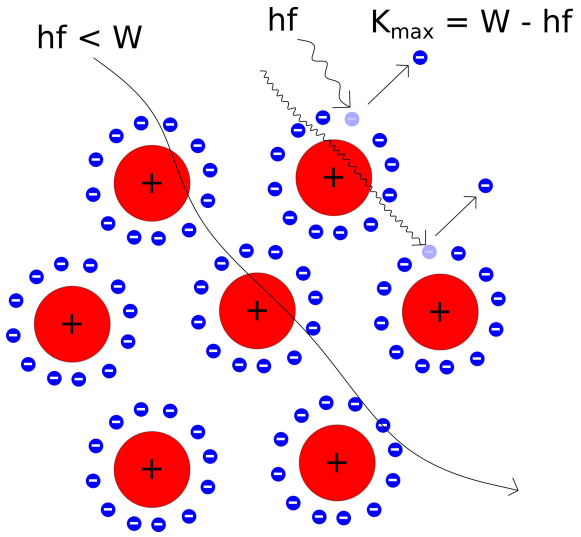

FIGURE 3 An illustration of the photoelectric effect. Only the photons with high enough energy can knock out electrons out of the valence band, and the higher energy photons (higher frequency) can penetrate deeper in the sample on average.

the incoming photon increases, the photoelectric effect can take place with electrons closer to the ground state, and a sudden increase in absorption is observed. These sudden increases in absorption are called X-ray absorption edges. The interactions of primary incoming radiation with these inner-shell electrons are also exploited in many X-ray techniques, such as X-ray fluorescence, X-ray absorption spectroscopy, and Auger electron spectroscopy. [12]

The X-ray absorption is strongly affected by the absorbing atom and the X-ray energy. The kinetic theory of absorption [12] predicts that the probability of X-ray absorption by a single electron of the atom shell, a.k.a. atomic coefficient for X-ray absorption, is

$$t_a = C_a \lambda^3 Z^4, \tag{3}$$

where C_a is a constant for each absorber element, λ the wavelength of the photon and Z the atomic number of the absorber atom. It can be noted that the X-ray absorption depends heavily on the photon energy (lower energies are more easily absorbed), and absorber material (heavier elements have higher absorption). This explains why light elements, like Be, are used when high X-ray transmission is required and heavy elements like Pb are used when high X-ray and gamma ray absorption is required. An example of X-ray absorption from 10 eV to 20 keV X-ray energies for three different materials, Be, Cu and Pb, is shown in Figure 4 [15].

Like visible light, also X-rays follow the Snell's law of refraction. The refractive index for X-rays, however, is very close to unity and in the scope of this thesis the refraction is not relevant. X-ray reflection, on the other hand, is a matter of great interest. Total external reflection can take place when X-rays come from optically

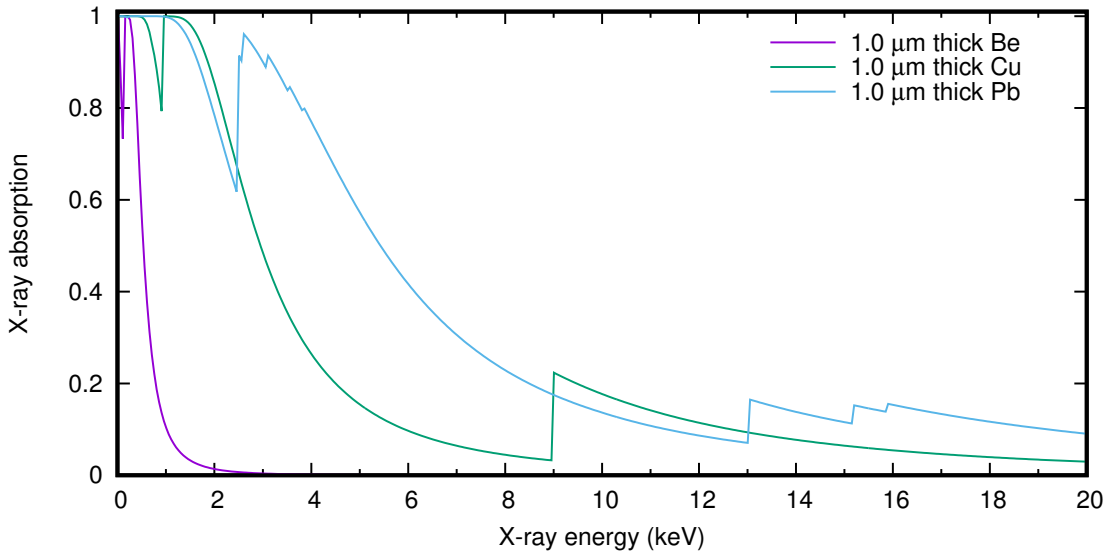

FIGURE 4 X-ray absorption as a function of X-ray energy for three different absorbers: a 1.0 µm thick Be, Cu and Pb. X-ray absorption increases with decreasing energy and increasing absorber atomic number. Sharp absorption edges occur at energies where X-ray is able to ionize more electrons. X-ray absorption values were obtained from Ref. [15].

denser material (like vacuum) to optically less dense material (like glass). Because the refractive indexes are very small for X-ray energies, the incident angle must be very small for the reflection. This critical angle for borosilicate glass can be approximated as [16]

$$\theta = \frac{0.03}{E}, \tag{4}$$

where θ is in radians when energy E is given in keV. For example, for a typical X-ray energy of 5.9 keV, the critical angle is 0.29 degrees. The reflectivity below the critical angle does not reach 100% because some X-rays are always absorbed in the glass.

X-rays can also interact with the crystalline structure of the material via Bragg's diffraction. If the X-rays scattered from two different lattice planes have the same phase constructive interference takes place, and this condition is written as [12]

$$2 \cdot d \sin(\theta) = n \cdot \lambda, \tag{5}$$

where d is the lattice spacing, λ the wavelength of the photon, and θ the angle of incidence.

Photons can also interact via Thomson scattering, Rayleigh scattering, Compton scattering, and pair production, but these are less dominant at typical X-rays relevant to this thesis than the interactions discussed earlier, and I will not discuss these interactions here.

3 PARTICLE-INDUCED X-RAY EMISSION

Particle-induced X-ray emission is a technique known to be capable of fast, multi-elemental analysis. In PIXE, an ion beam is used to excite inner-shell electrons from the target atoms, and the characteristic X-rays are detected. PIXE is attractive for many reasons: it can be used to detect almost all elements with the exception of lighter elements, it is delicate enough for measuring expensive museum artifacts, it can be performed outside a vacuum, it is capable of detecting very small concentrations, and so on. [11]

3.1 Ion-matter interactions

The interaction of ions, such as protons, with the matter is quite different from the interactions between X-rays and matter. When an energetic particle collides with matter there can occur many interactions such as a change of the charge state, elastic scattering, inelastic scattering, nuclear reactions et cetera [17]. Since the topic is very broad I will only focus on the energy loss which is the interaction most relevant to particle-induced X-ray emission.

The energy loss of a charged particle traveling in a matter can be associated into four different phenomena: electronic stopping, nuclear stopping, change of projectile charge state, and radiative stopping [17]. Electronic stopping refers to the energy loss caused by the excitation and ionization of target electrons (inelastic collisions), and with typical proton energies used in PIXE, it is the dominant effect. Nuclear stopping refers to the elastic collisions with the atomic nucleus in the matter. The effect of the projectile charge state change to the velocity of incident ion is rather small and can be ignored. The radiative stopping refers to slowing down of ions due to the emission of radiation and its contribution to the

stopping becomes important at high projectile energies. Most notably radiative effect for PIXE is the bremsstrahlung radiation that was discussed earlier.

The stopping force (a.k.a. stopping power) is used to describe the average energy loss in the matter and is defined as

$$S = -\frac{\mathrm{d}E}{\mathrm{d}x}. \tag{6}$$

Instead of stopping force, stopping cross section is sometimes used

$$S_M = -\frac{\mathrm{d}E}{\mathrm{d}x}N^{-1}, \tag{7}$$

where N is the particle density of the matter [17]. Sometimes mass density ρ is used instead of the particle density.

3.2 Quantitative elemental analysis

The intensity of diagram X-ray lines $Y(Z)$, and concentration C_Z expressed in mole per atomic fraction ($C_Z = {}^{M_Z}/_{M_{total}}$), of the element Z are related through equation [11]

$$Y(Z) = \frac{N_{av}\omega_Z b_Z t_Z \epsilon_Z (\Omega/4\pi)}{A_Z} N_P C_Z \int_{E_0}^{E_f} \frac{\sigma_Z(E)\, T_Z(E)}{S_M(E)} \mathrm{d}E, \tag{8}$$

where N_{av} is the Avogadro constant, ω_Z the fluorescence yield (probability that X-ray is emitted when an electron is relaxed to inner-shell), b_Z the branching fraction of the diagram line (e.g., Kα_1 within K series), t_Z the transmission through any absorber between the sample and the detector, Ω the detector solid angle, ϵ the efficiency of the detector, A_Z the atomic mass of the element, N_P the number of the incident ions, E_0 the initial energy of the incident ion, E_f the energy of the ion exiting the material, σ_Z the ionization cross section and $S_M(E)$ the overall stopping cross section of the sample ($S_M(E) = \frac{\mathrm{d}E}{\mathrm{d}x}\rho^{-1}$). The integral term is known as the matrix correction which can only be evaluated if all concentrations of the (major) elements in the matrix are known. The T_Z term within the integral term is the X-ray transmission of the matrix

$$T_Z = \exp\left[\left(\frac{\mu}{\rho}\right)_M \frac{\cos\alpha}{sin\theta_{TO}} \int_{E_0}^{E} \frac{\mathrm{d}E}{S_M(E)}\right], \tag{9}$$

where $\left(\frac{\mu}{\rho}\right)_M$ is the concentration weighted sum of the mass attenuation coefficients of the matrix elements, α the tilt angle (angle between sample normal and beam) and θ_{TO} the exit angle of the detected X-ray ($0° \leq \theta_{TO} \leq 90°$). It should be noted that the equation (8) does not take into account secondary fluorescence;

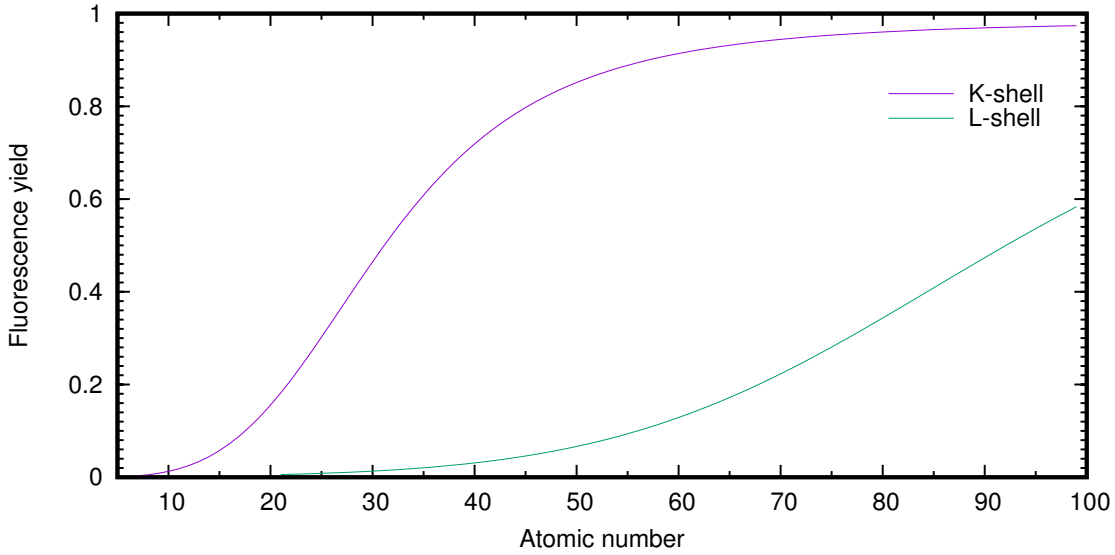

FIGURE 5 Relative fluorescence yields as a function of atomic number. K-shell fluorescence yield is calculated using Eq. (1) from reference [18] and average L-shell fluorescence yield using Eq. (8) (fit parameters from Table 2) from reference [19]. If fluorescence yield is, for example, 0.20 then 20% of the relaxation processes emit X-rays, and in 80% of cases an Auger electron is emitted.

referring to the absorption of X-rays originated in the sample which then fluorescence as a lower energy X-rays (e.g. Fe Kα absorbed by Si, and re-emitted as Si Kα).

The likelihood of an ion interacting with the material so that X-rays are produced is called an X-ray production cross section, σ_x , and it can be written as

$$\sigma_x = \sigma_Z \omega_Z. \tag{10}$$

Semi-empirical K- and average L-shell fluorescence yields [18, 19] are plotted in Fig. 5, K- and L-shell ionization cross-sections as a function of atomic number for a 3 MeV proton beam are plotted in Fig. 6, and the ionization cross-sections for Na, Si, Fe, Cu K lines as a function of proton beam energy are plotted in Fig. 7. Ionization cross-sections were calculated using the ISICS2008 software [20].

3.3 Common features in X-ray spectra

To understand the features of a common X-ray spectrum, the understanding of just characteristic X-rays is not enough. The other common features include background radiation, pile-up, and escape peaks [11]. An example of an X-ray spectrum containing all these features is shown in Fig. 8.

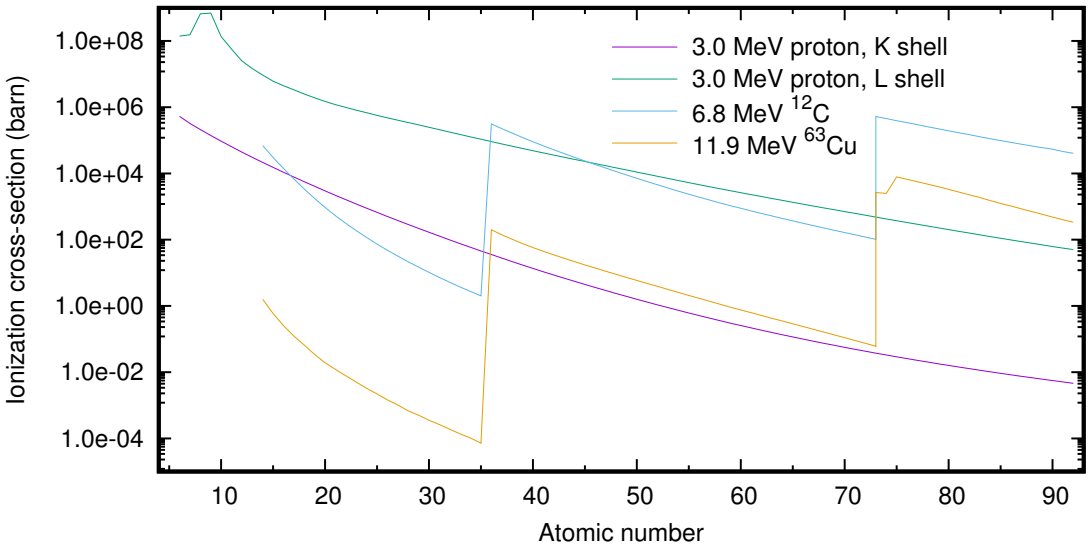

FIGURE 6 Ionization cross sections for a 3 MeV proton beam, 6.8 MeV ^{12}C beam, and 11.9 MeV ^{63}Cu beam as a function of target atom atomic number. The cross sections were calculated using the ISICS2008 software [20]. For ^{12}C beam, and ^{63}Cu beam the edges are resulting from the change of ionization cross section from K-shell to L-shell and from L-shell to M-shell. Reported L- and M-shell ionization cross-sections are sums of the subshell (L1, L2, etc.) ionization cross-sections.

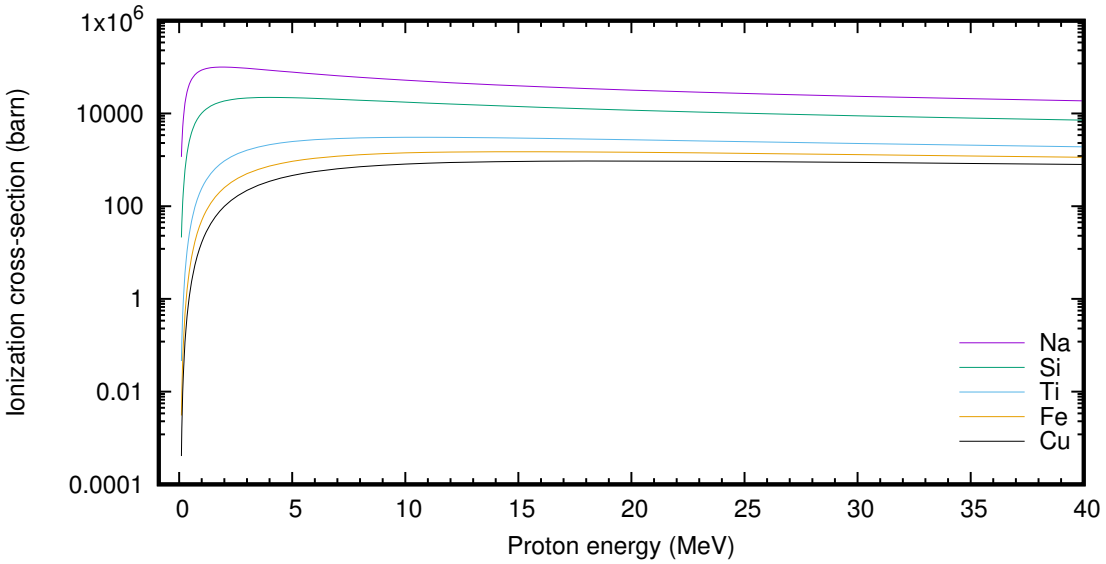

FIGURE 7 K-shell ionization cross section as a function of proton beam energy for five different elements: Na, Si, Ti, Fe, Cu. The cross sections were calculated using the ISICS2008 software [20].

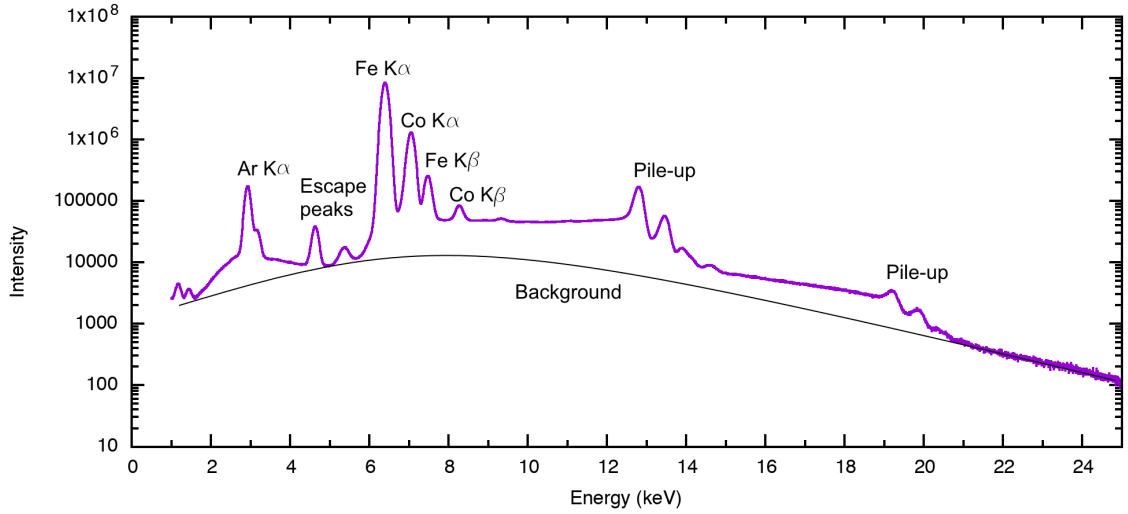

FIGURE 8 Measured X-ray spectrum of a sample containing Fe and Co. In the spectrum, the peaks of the main elements, pile-up peaks, escape peaks, and background are shown. The measurement was done with an external beam (3.0 MeV incident energy), and as a result Ar from air can be seen. X-rays were collected using a silicon drift detector.

3.4 Background in PIXE

One factor limiting the detection of characteristic X-rays in PIXE is the background. The background in PIXE arises mainly from Bremsstrahlung radiation. It is known that the intensity of the Bremsstrahlung is proportional to the acceleration of a moving particle to the second power. Because a proton is much heavier than an electron it creates radiation that has almost over six magnitudes lower intensity. Also because of this effect, the Bremsstrahlung background caused by protons is negligible, and the most significant effect is caused by electrons affected by the ion-atom collisions. [11]

The main contribution of the electron background comes from secondary electron Bremsstrahlung (SEB) [21]. The maximum energy of the Bremsstrahlung radiation from SEB is the maximum energy of an electron. This is approximately the same as the maximum energy an ion can transfer to an electron in an elastic collision. Using conservation laws of energy and momentum it follows that the maximum energy that can be transferred, T_m, is

$$T_m = 4E_0\frac{m_e}{m_{ion}}, \tag{11}$$

where m_e is the mass of electron, m_{ion} the mass of the incident ion and E_0 the energy of the incident ion. This value is circa 6.5 keV for a 3 MeV incident proton beam. [22]

The intensity of these backgrounds varies with the detection angle. The most

intense SEB background is known to be at 90-degree angle with respect to the proton beam. This is why it is beneficial to place the detector at an angle different than 90 degrees relative to the beam. [22]

In addition to the Bremsstrahlung background, the gamma ray background is relevant in some cases. It is caused by the Compton scattering of high-energy photons originated from nuclear reactions in the specimen. These high energy photons collide inelastically in the matter and lose some of their energy. The effect is highest when there are light elements, such as, C, N, O, F, Na, Si, P, S, Cl, K or Ca in the sample, as shown by Anttila et al. [23].

3.5 Pile-up and escape peaks

In the X-ray spectrum, there are two common detector related phenomena: pile-up and escape peaks. Pile-up happens when two (or more) photons reach the detector so close in time to each other that the detector records only one event with the energy of the photons combined. Escape peak is a feature of the detector absorber material. When a photon with energy higher than the absorption edge of the detector absorber material interacts with the detector, it can excite the atoms in the detector and the characteristic X-rays are emitted from the detector. If these X-rays escape the detector material, then the detected energy is equivalent to the original energy subtracted with the characteristic X-ray of the detector absorber material. [11]

3.6 Different ionization methods

There are three main methods to excite inner-shell electrons of atoms: an electron beam, high-energy X-rays, or an ion beam [12]. For each of the excitation methods, there is an X-ray spectroscopy technique: scanning electron microscope energy-dispersive X-ray spectroscopy (SEM-EDX) [24], X-ray fluorescence (XRF) [25] and particle-induced X-ray emission (PIXE) [11], respectively. All of the mentioned techniques have the same underlying principles, but with a unique characteristic.

SEM-EDX is performed always under a vacuum, which allows the detection of the low energy X-rays with good efficiency. Compared to the other two techniques it has a very high Bremsstrahlung background originating from the incident electron beam. This makes it harder to detect low concentrations, but SEM-EDX has the advantage of producing high lateral resolution elemental maps and

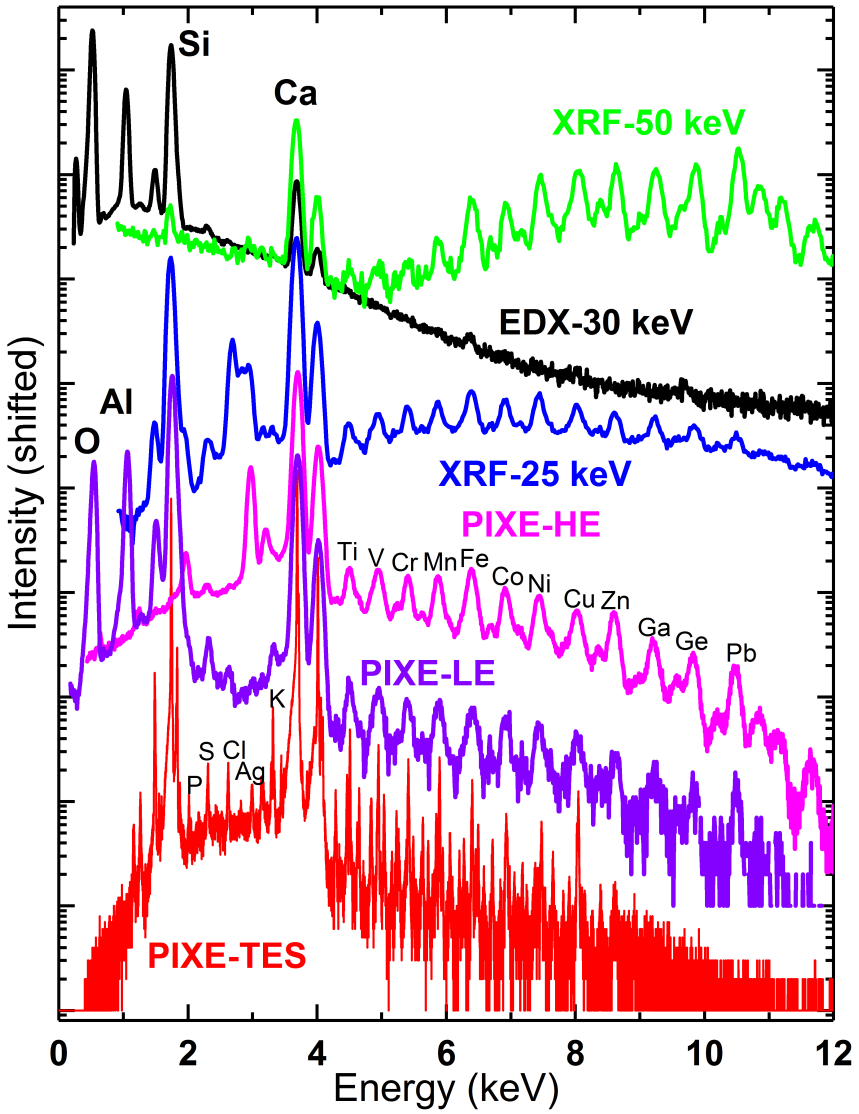

FIGURE 9 Standard reference material NIST SRM 611 (glass with impurities) measured using different X-ray emission techniques. Two different acceleration voltages were used for X-ray fluorescence (XRF), and three different detectors, low-energy (LE), high-energy (HE) and transition-edge sensor array (TES), were used for particle-induced X-ray emission (PIXE).

taking high-resolution SEM images at the same time. The backscattered electrons can be easily deflected, and no additional filters are needed and elements down to B can be detected. [24]

X-ray fluorescence is a very compact technique and out of the three, the only one that is portable. The X-ray source is much cheaper compared to a scanning electron microscope or a particle accelerator making the technique easily available. X-ray fluorescence also has a low background, and it can be operated outside of a vacuum. X-ray fluorescence excites X-rays from deeper inside the sample than SEM-EDX and typical PIXE, which can be an advantage or a disadvantage, depending on the situation. [25]

In PIXE, typically a 2–3 MeV proton beam is used for excitation. As in XRF, PIXE has a low background, and ability to measure outside of a vacuum. A proton beam can be focused into a microbeam and elemental mapping can be done with a better lateral resolution than with XRF, but not as good as SEM-EDX. Proton beam is also more efficient at exciting X-rays from lighter elements and less efficient at exciting X-rays from heavier elements compared to the XRF. [11]

Sometimes it can also be beneficial to use heavier ions such as ^{7}Li or ^{12}C for PIXE, and this is often called heavy-ion PIXE or HIXE. The biggest advantage of HIXE is the ability to combine it with other powerful ion beam analysis (IBA) methods, like Rutherford backscattering spectrometry (RBS) [26] or elastic recoil detection analysis (ERDA) [27]. In some cases, HIXE can also be more sensitive than regular PIXE [26]. Some disadvantages of HIXE is that it cannot be used for external beam measurements, and the characteristic X-rays from the incident ion beam can disturb the detection of certain elements. Combination of heavy ions and high-energy resolution can be beneficial for chemical speciation, and it is discussed in detail later.

A comparison of different techniques is shown in Figure 9. A glass with a composition of 72% SiO_2, 14% Na_2O, 12% CaO, 2% Al_2O_3 was measured with all techniques. In addition, the sample contains more than 50 added trace elements with a nominal 500 ppm concentration. In the figure, there is one SEM-EDX spectrum, two XRF spectra, and three PIXE spectra with different detectors (low-energy, high-energy, and high-energy-resolution detectors). SEM-EDX does not see the lower concentration elements but has the best efficiency at energies below 1 keV. With XRF more high energy X-rays are generated than with other methods, and only with PIXE high-resolution detector we can see all the different X-ray transitions in 4–8 keV energy region. In conclusion, all the techniques have their uses, and it depends on the area of study which method is preferred.

3.7 X-ray optics

Focusing X-rays is beneficial in many cases. It allows more efficient X-ray collecting, and thus smaller beam doses can be used or higher statistics collected in shorter time. Focusing X-rays; however, is not a trivial task. The solution that has been created for this problem is the polycapillary lens [16].

A polycapillary lens focuses X-rays by means of total external refraction (Eq. (4)). These lenses consist of multiple hollow glass tubes with diameter in the order of few or tens of micrometers. When these capillaries are slightly bent, the system becomes a focusing tool [16]. Polycapillary lenses have seen some use in SEM-EDX [28], and in PIXE [29, 30]. Focusing polycapillary lenses are widely used in XRF both in the source (enabling micro-XRF) and detector side [16]. An image of a polycapillary lens is shown in Figure 10.

One thing that should be noted is that the area from where X-rays are collected is energy dependent. The full-width half-maximum diameter of the collection area d can be obtained with equation

$$d = 2 \cdot \theta \cdot f, \tag{12}$$

where θ is the critical angle (Eq. (4)), which depends on the energy of the X-ray and f is the distance between the lens and X-ray spot [16].

3.8 Chemical analysis with PIXE and other X-ray techniques

For chemical analysis, two common X-ray methods used are X-ray photoelectron spectroscopy (XPS), and X-ray absorption near edge structure (XANES or NEXAFS).

XPS is a surface sensitive method for chemical and elemental analysis. In XPS, the sample is exposed to monoenergetic X-rays. Then, as the name implies, photoelectrons are emitted and detected. These photoelectrons can only escape from the first 1 to 10 nm, making the technique very surface sensitive. The measured kinetic energy of the detected electrons is related to the binding energies of the photoionized atom. These binding energies are affected by the chemical environment and the electronic structure of the atom which is utilized for chemical analysis. This technique can detect elements heavier than helium. [31]

XANES is a measurement of X-ray absorption near the absorption edge of an element. XANES is a method highly sensitive to the chemistry, oxidation state, and geometry of the absorbing atom. This technique requires a tunable, high-intensity X-ray source and it is done usually with synchrotrons. [32]

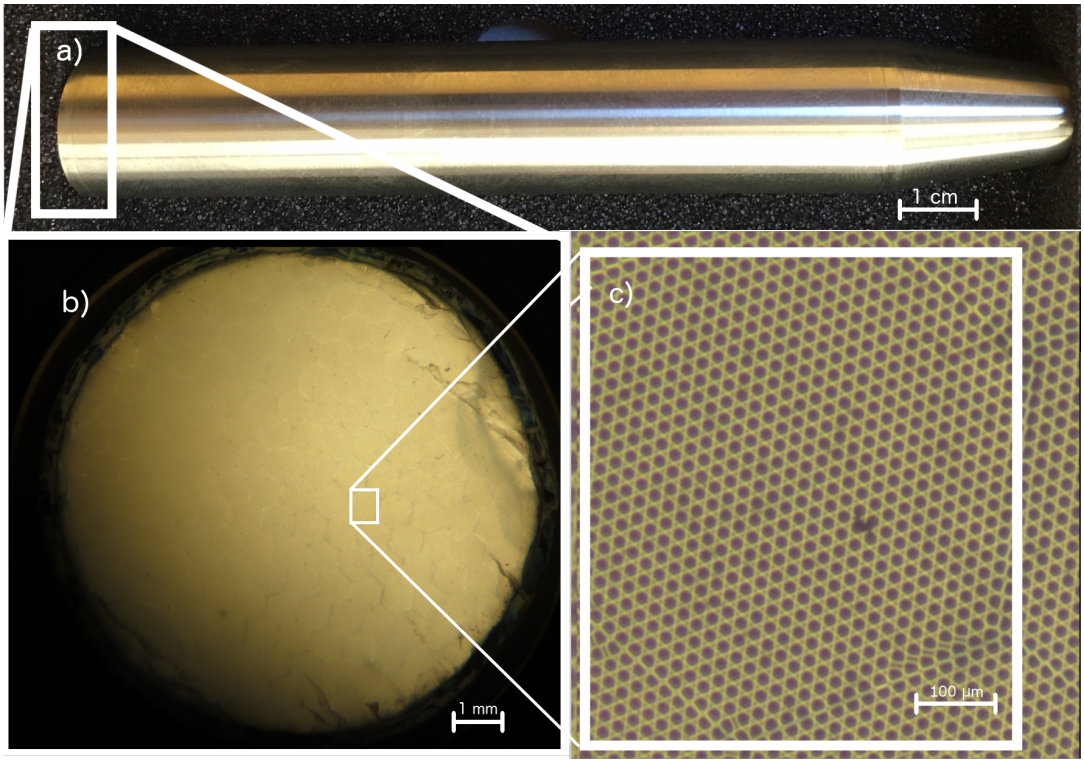

FIGURE 10 a) A photograph of the polycapillary lens used at the University of Jyväskylä, b/c) The polycapillary lens imaged with an optical microscope using two different magnifications.

PIXE is most often associated with only elemental analysis yielding no chemical information. However, the technique has been demonstrated to be useful for chemical speciation already in the 1970s using high-energy resolution wavelength-dispersive detectors [33–36]. Chemical speciation with PIXE has not been widely applied probably due to limited equipment (requires high-energy-resolution detector), and more experimental data is required before a fundamental understanding of X-ray satellite line intensity dependency on different chemical environments can be reached [37].

Chemical sensitivity of PIXE can come from energy shifts of the X-rays [33, 34], from the relative intensity changes of different diagram lines [38], or from the relative intensity changes of the X-ray satellite lines [35] (lines with two or more electron vacancies). In the first case, the shift is typically between 0.1 and 1 eV [39] (illustration in Fig. 11). In the second case, typically the ratio of α and β transitions is measured. This ratio has been reported to differ up to 10% [38] in some cases. In the final case, heavy ions (He or heavier ions with high stopping power) are used to achieve multiple ionization of the target atoms, and along with the inner-shell electron, also outer-shell electrons are excited to the vacuum level. The energy of the emitted photon depends on the number of electron vacancies, and instead of a single peak, multiple peaks can be observed. Before the X-ray emission, some of the extra vacancies can be filled, and this is affected by the

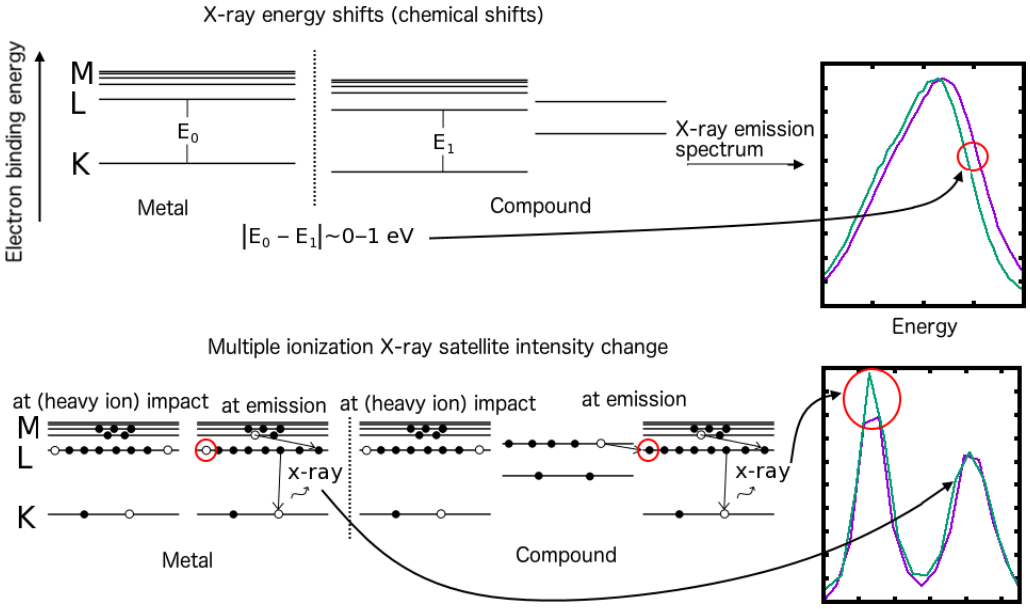

FIGURE 11 An illustration of two different chemical effects in high-resolution PIXE spectra: an energy shift and a multiple ionization X-ray satellite intensity change. X-ray energy shifts are caused by change in the electron binding energies for the element in different chemical environment. Multiple ionization X-ray satellite intensity changes are mainly caused by electron rearrangement processes prior the X-ray emission.

chemical environment. When these vacancies are filled by electrons from neighboring atoms (interatomic transitions) or by valence electrons bound to neighboring atoms (intra-atomic transitions) the probability to fill vacancies depends on the chemical environment [35] (illustration in Fig. 11). These rearrangements, in some cases, cause significant changes in X-ray satellite line structure between different chemical species of the same element.

Chemical shifts in PIXE

Chemical shift in X-ray emission techniques is generally defined as the change in characteristic X-ray energy between the atom in chemical compound and atom in metal (or in other single element form) $\Delta E = E_{compound} - E_{metal}$ [34]. Chemical shifts can be caused by changes in the core binding energies, multiplet structures, valence-band energies or changes in the density of states [34]. These effects make it hard to predict the energies. Theoretical calculations using Hartree–Fock–Slater and Hartree–Fock computer codes have been done, and they were able to predict some, but not all of the observed trends [34, 36]. Density functional theory (DFT) has been also applied for the study of chemical shifts, and it has been applied for predicting the experimental results with a good success [40]. Because of small changes, studying these requires a detector with high-energy resolution.

X-ray satellite lines

There are three types of X-ray satellites: multiple ionization satellites, charge-transfer satellites for late transition-metal compounds, and molecular–orbital splitting satellites [41]. From these the multiple ionization satellites are the ones usually referred as satellite lines. We will focus on the first type of X-ray satellites, discussion of the other satellites can be found from reference [41].

When heavier ions, like $^{4}He^{+}$, $^{12}C^{3+}$, or $^{20}Ne^{2+}$, are used for bombarding the sample, multiple ionization becomes common. When multiple ionization occurs, X-ray satellite lines or even hypersatellite lines can be detected. These X-ray satellites are generally written with following notation [13], $X^{a}Y^{b}$, where X is the inner-shell with the electron hole, Y is the outer-shell where electron comes to fill the inner-shell hole, and a and b are the number of electron holes in these shells. The common K_{α} transition with this notation can be written as $\mathrm{K^{1}L^{0}}$, but usually, the index for inner-shell ionization is left out if it is one. Thus, $\mathrm{KL^{0}}$ is also a proper notation for K_{α} transition(s). The transitions where a=1 and b>0 are called satellite lines, and transitions where a>1 are called hypersatellites [13]. The hypersatellites are much rarer than satellite lines, and thus not as interesting for applications.

When studying the multiple ionization satellite distributions, the average L-shell vacancy fraction during X-ray emission (for KL transitions) is often used, and it is defined as [42]

$$p_{L}=\frac{1}{N}\sum_{n}nf_{n}, \tag{13}$$

where N is the number of L-shell electrons in the non-ionized state and f_n is the fractional intensity ($\sum f_n = 1$) of the nth satellite line. The geometrical model (GM) was developed to study the systematics of the p_L [43]. The model predicts that the number of spectator vacancies at shell n ($n = 1\,(\mathrm{K})\,, 2\,(\mathrm{L})\,, 3\,(\mathrm{M})\,, ...$) is a function of the universal variable X_n

$$X_{n}=\frac{4V\sqrt{G\left(V\right)}Z_{1}}{nv_{1}}, \tag{14}$$

where v_1 is the velocity of the incident ion, v_2 is the average velocity of electron in n shell, $V = {}^{v_1}/_{v_2}$, Z_1 the atomic number or effective charge of the incident ion, and $G\left(V\right)$ is the binary encounter approximation (BEA) scaling function in equation [44]

$$\sigma=\frac{NZ_{1}^{2}\sigma_{0}}{U^{2}}G\left(V\right), \tag{15}$$

where σ is the ionization cross-section, $N = 8$ for L-shell, $\sigma_0 = \pi e^4$ is a constant, and U is the electron binding energy. Universal variable X_n can be interpreted as the measure of the perturbation strength that characterizes the collision. The

value of universal variable X_n also depends on whether Z_1 is interpreted as the effective charge or the atomic number and how the BEA scaling function is calculated.

It has been shown by Watson et al. [35] that multiple ionization satellite line intensities are affected by the chemical bonds and they have been studied ever since in many papers, [39, 45–49] to name a few. For chemical information, relative intensities of the satellite lines are usually the most interesting feature, but also chemical shifts can be analyzed. Changes in relative intensities between different chemical bonds are most drastic when the electron that fills the inner-shell hole comes from the valence shell. This is natural as the valence shell electrons contribute most to the chemical bonds. For example, in a study by Uda et al. [39] large relative intensity changes were observed for different fluorides ($Z = 9$), but not for different sodium ($Z = 12$) compounds when studying Kα X-ray satellites. However, significant relative intensity changes can also occur for transitions where the electron shells involved in the X-ray emission process are not involved in the chemical bonds. This can happen for two reasons: either the collision produces different vacancy distribution or outer-shell rearrangements take place prior to the X-ray emittance that change the intensity distribution. Based on the experimental data it has been concluded that the latter case is the dominant one [35]. Prior to the X-ray excitation, some of the outer-shell electrons are rearranged in a process involving electrons from the neighboring atoms. In other words, the outer-shell holes are filled by electrons from neighboring atoms, which allows chemical speciation.

The geometrical model does not factor in the chemical environment, and we need other theories to understand and predict the effect of the chemical environment. Average total valence electron density of a chemical compound is a parameter that has been shown to correlate with p_L values and can be calculated as [35]

$$D_V = 0.602 \frac{n_v \rho}{W_{mol}} \text{electrons}/\text{Å}^3, \tag{16}$$

where n_v is the total number of valence electrons, ρ is the mass density and W_{mol} is the molecular weight.

D_V can predict general trends, but it cannot predict the intensity distributions accurately. Intensity distributions of X-ray satellite lines have been calculated theoretically, for example by Uda [50]. Uda used molecular orbital calculations to predict the intensity distributions of fluoride compounds with a good agreement to experimental data.

4 X-RAY DETECTORS

4.1 Transition-edge sensor

A transition-edge sensor, TES, takes advantage of the superconducting phenomena. To be more specific, TES utilizes the sharp transition between the superconducting and the normal state. When an energetic particle, for example, a photon is absorbed in the detector, the temperature rises. This small temperature rise causes the resistance of the superconductor at the transition-edge increase, leading to an energy resolution even better than 0.1% for a typical X-ray. The energy resolution of the detector depends strongly on the temperature (because of the thermal noise), and therefore the superconductor is chosen so that its superconducting transition is close to 100 mK temperature. [51]

The transition-edge sensor is a calorimeter with three main components: a thermometer, an absorber, and heat bath [51]. The thermometer is a superconductor at the transition-edge, and it is the most critical part affecting the energy resolution. The absorber is made of an element (or elements) with a high X-ray absorption, typically Au or Bi, and it converts the energy of the photon into heat. The absorber properties determine the X-ray absorption efficiency, and the decay time of the X-ray pulse depends on the heat capacity of the absorber as well as with the thermal conductance of the absorber and heat contact between the absorber and the heat bath. The heat bath is a cooling component which keeps the system at the operating temperature during the measurement. Typically adiabatic demagnetization refrigerator, ADR, is used to cool the detector to sub-Kelvin temperatures. The operation principle of a transition-edge sensor is visualized in Figure 12.

To characterize the performance of TES, some key properties are energy resolution, X-ray absorption efficiency, and the decay time of the pulse. The energy resolution of the transition-edge sensor can be approximated using equation [52]

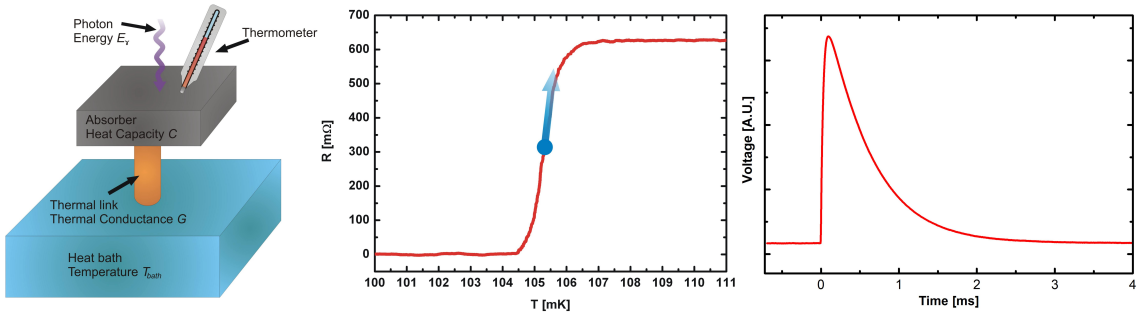

FIGURE 12 The operation principle of the transition-edge sensor. A photon absorbed in the detector is converted to heat, and a superconductor in the transition-edge is used as a thermometer to detect the absorbed energy of the incoming photon.

$$E_{fwhm} = 2.35\sqrt{\frac{4k_B T_0^2 C_0}{\alpha'}}\sqrt{\frac{N}{2}}, \tag{17}$$

where k_B is the Boltzmann constant, T_0 the temperature of the TES, C_0 the heat capacity of the absorber, and α' describes the steepness of the superconducting transition. The constant N (typically 6) describes the power of the cooling into the heat bath in equation $P_{cool} \left(T^N - T_{bath}^N\right)$, where T is the temperature of the absorber/superconductor and T_{bath} is the temperature of the heat bath. As can be seen from Eq. (17), it is critical to keep the detector at a very low temperature. The transition-edge of the superconductor, and thus the operating temperature, is around 100 mK.

The X-ray absorption efficiency depends on the absorber material and its thickness. Absorber material has also two other important properties: heat capacity C, and thermal conductivity G. When the photon comes to the detector, it creates a thermal pulse which rises rapidly to a value inversely proportional to heat capacity and then exponentially decays with a time constant $\tau = C/G$, where C is the heat capacity and G is the thermal conductivity (including the thermal conductivity of the thermal link) [51]. This thermal pulse creates a change in the resistance of the superconductor, and the change in the current is measured. Fast decay time and high pulses are preferable and thus small heat capacity and high thermal conductivity are desired. Also as seen from equation (17), small heat capacity is desirable for good energy resolution. For good X-ray absorption, however, a thicker absorber is preferred which leads to higher heat capacity. Thus the absorber thickness must be carefully decided depending on the intended use of the detector. For high absolute efficiency, large active absorber area is desirable, which also increases the heat capacity.

A TES array is a solution created to overcome requirements for small heat capacity and high X-ray efficiency. Instead of making a TES with one large absorber, a detector array is built with over hundred individual pixels. Furthermore, a time-

division multiplexing is used to read each pixel while minimizing the number of wires and heat load in the detector array. [51]

4.2 Solid-state detectors

Some of the oldest solid-state detectors are lithium drifted semiconductor detectors, Si(Li) and Ge(Li), and high-purity Ge (HPGe) detector. These detectors are based on electron-hole pair creation by the incoming photon. Charges are collected by an electric field, charge pulse is created and amplified and the electric signal is analyzed. These detectors were the first ones to obtain a good enough energy resolution and efficiency to distinguish neighboring elements with a quick measurement. These detectors require low operating temperatures (usually using liquid nitrogen) to suppress background from a thermal electron-hole pair production. Ge detectors retain high efficiency at higher energies because of the higher absorption efficiency of Ge compared to Si. On the other hand, the escape peak of Ge is more intense, and it has also higher efficiency for the gamma ray background. [11]

Within the last two decades, especially silicon drift detectors (SDD) have replaced other semiconductor detectors. With SDDs no cryogenic liquids are required for the cooling, but instead, the operating temperature is reached with electrothermal (Peltier) cooling [53]. In SDDs, highly pure Si with a very low leakage current is used, which allows the higher operating temperature compared to Si(Li) detector, for example. Electrothermal cooling allows more compact detectors that can be used even in portable systems. Another advantage of SDD is the ability to process very high count rates without sacrificing too much of the energy resolution. The high count rates are achieved by the design with small anode surrounded by many electrodes. Depending on the electrode that the photon hits, the drift time to the anode is different, which makes it possibly to distinguish even multiple photons that hit the detector at the same time. This "drift" principle allows the detector to handle count rates even up to million counts per second. The disadvantage of SDD compared to Si(Li) detector is worse X-ray efficiency at high energies due to thinner absorbing material. The compact size of a modern solid state detector (Ketek AXAS-D silicon drift detector) is shown in Fig. 13.

FIGURE 13 An image of a modern silicon drift detector (Ketek AXAS-D detector). All the electronics and cooling needed for the detector are inside the compact casing. The actual active area is highlighted in the figure, is quite small (6.2 mm in diameter) and circular in shape.

4.3 Wavelength-dispersive detectors

The wavelength-dispersive X-ray detector (WDX) is based on the principle of Bragg's law (Eq. (5)). A high-quality crystal is used to obtain a sharp constructive interference peak. The X-rays with different energies scatter to different angles, and are detected with position sensitive detector like a charged coupled device (CCD). With one crystal only a narrow energy region can be detected, so multiple crystals are needed. For the price of the low efficiency, energy resolution down to 0.5 eV can be achieved [40]. The basic principle of WDX is shown in Fig. 14.

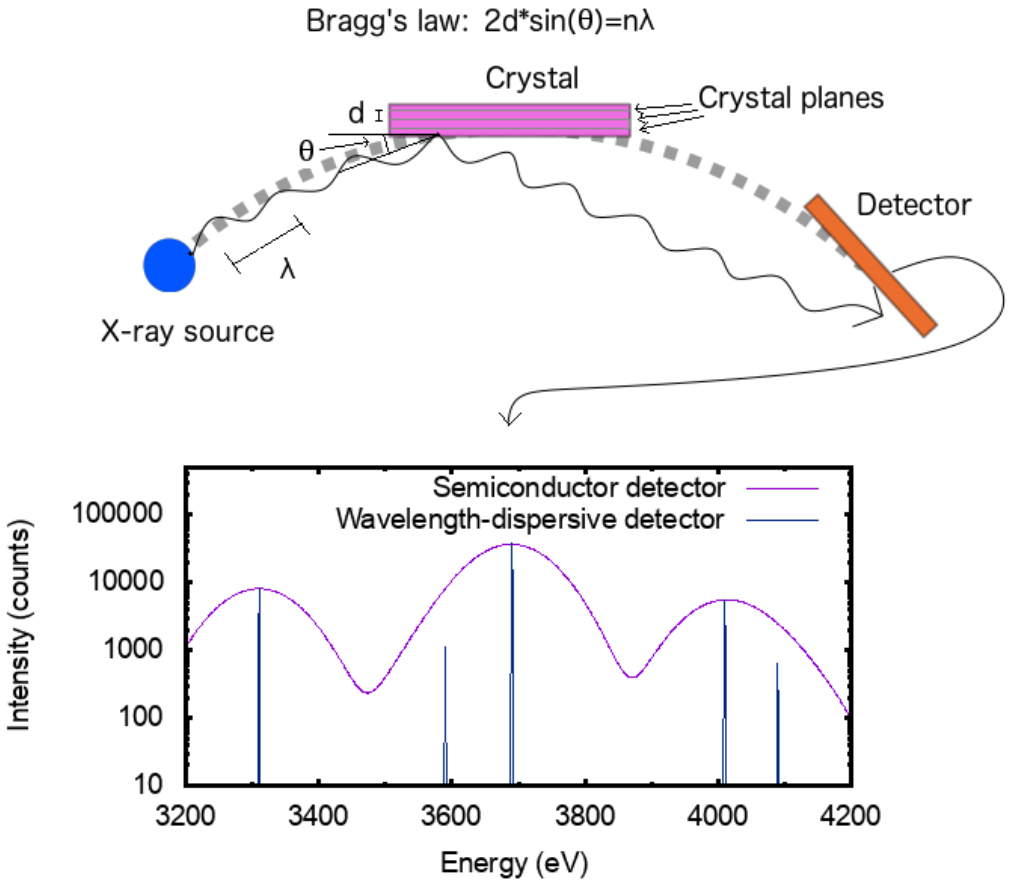

FIGURE 14 A schematic drawing of wavelength-dispersive X-ray detector (WDX), and simulated spectra for WDX and silicon drift detector (SDD) for an illustration. WDX has a superior energy resolution allowing for the separation of peaks that overlap in SDD spectrum. On the downside, WDX works on narrower energy region compared to the SSD. Simulations were calculated using CPIXE software[54]

.

5 TRANSITION-EDGE SENSOR DATA ANALYSIS AT THE UNIVERSITY OF JYVÄSKYLÄ

5.1 Digital filter

Transition-edge sensors are inductively coupled with SQUIDs (Superconducting QUantum Interference Device). One SQUID is coupled to bias and feedback current. When the photon hits the detector, resistance changes and the bias current also changes (bias voltage is constant). Feedback loop tries to keep the overall magnetic flux through the SQUID as constant, and the change in the bias current causes a pulse in the feedback voltage which is stored. To obtain the energy spectrum from the measured data in a pulse form, digital signal processing is used. Digital filtering (from now on shortened as filtering) is a series of mathematical procedures to obtain information from discrete data. In case of TES analysis, the pulse height is proportional to the deposited energy and is the quantity we are the most interested in. From the digital filter, we want the following criteria: short calculation time; good energy resolution; insensitivity to pile-up, baseline drift, tails of previous pulses, noise shape, and pulse shape.

The measured signal m is defined as

$$m = \left(m_1, m_2, \ldots, m_{j-1}, m_j, m_{j+1}, \ldots, m_{i-1}, m_i\right), \tag{18}$$

where j is the number of samples before the pulse (pre-trigger signal) and i is the total number of samples in the pulse. One very simple filter is just taking a maximum of the pulse $f_{max} = \max(m)$. This filter is very simple and efficient but lacks many properties we are looking from the filter. It is sensitive to baseline drifts and pile-up, and the energy-resolution is poor. The next step forward would be taking the baseline drift into account so filter could be written as $f_{height} = \max(m) - \text{average}\left(m_1, m_2, \ldots, m_j\right)$. This filter is now less sensitive

to changes in baseline, but it is more sensitive to tails of previous pulses (in pre-trigger).

In order to improve the energy resolution and efficiency, a more advanced filter is needed. One such filter is the optimal filter a.k.a. Wiener filter which was introduced by Wiener in 1949 [55]. Let's consider a following measurement

$$m(t) = (h \star s(t)) + n(t), \tag{19}$$

where $\star$ denotes convolution, $s(t)$ is some unknown input signal at time t, $h(t)$ is known disturbance of the signal (for example motion blur in images), and $n(t)$ is additional noise. The goal is to find a filter which approximates the input signal

$$\hat{s}(t) = (g \star m)(t), \tag{20}$$

where g is the Wiener filter in the time domain. We require the filter to minimize the mean square error $\mathbb{E}\left[(\hat{s} - s)^2(t)\right]$. If the noise and the shape of the s are stationary it can be shown that the optimal filter in the frequency domain is

$$G(f) = \frac{H^*(f) S(f)}{|H^2|(f) S(f) + N(f)}, \tag{21}$$

where H is the Fourier transform of h, H^* is the complex conjugate of H, and S, N are the power spectral densities of s and n, respectively. In the case of transition-edge sensor pulses, there is no disturbance ($H = H^* = 1$), the noise is measured, and $s(t)$ is the average pulse normalized to unit height. The Wiener filter in the frequency domain is now

$$G(f) = \frac{S(f)}{S(f) + N(f)}, \tag{22}$$

and the filter in the time domain can be calculated as the inverse Fourier transform of $G(f)$, and it is normalized to the average pulse so that $\max_i (g \star \hat{s})_i = 1$. The saved ("filtered") value is normally calculated as $\max_i (g \star m)_i$.

In practice, the pulse-shape is energy dependent which is demonstrated in Fig. 15. Also, the noise is not constant over time, and in the case of pile-up the filter does not work as intended, and these events must be discarded from the analysis. Nonetheless, this filter provides a good energy resolution while maintaining a relatively fast calculation time.

A new class of filters were developed by Alpert et al. [56] to minimize sensitivity to pile-up, while maintaining good energy resolution. I will refer to these as Alpert filters. These filters are a new class of optimal filters that have some extra constraints to minimize sensitivity to pile-up. These filters differ from the standard Wiener filter also in a sense that they are calculated entirely in the time

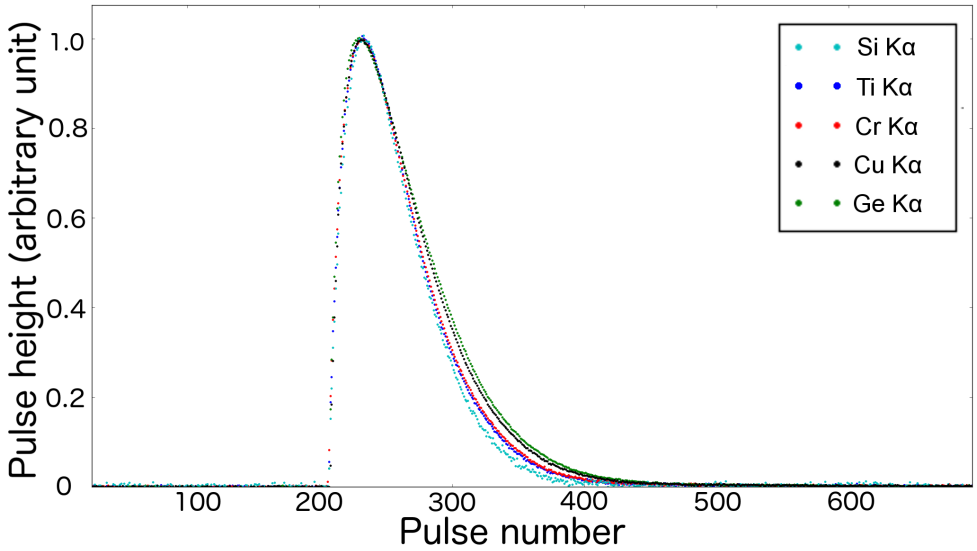

FIGURE 15 The pulse shapes of our detector for five different X-ray energies: Si Kα (1.74 keV), Ti Kα (4.51 keV), Cr Kα(5.41 keV), Cu Kα (8.05 keV), and Ge Kα (9.89 keV). Pulse heights are normalized to one. It can be seen that the decay time of the exponential tail is energy dependent.

domain. Let's consider a pile-up situation where signal f is thought to consist of two pulses

$$f(t) = a_0 s(t - t_0) + a_1 s(t - t_1) + b, \tag{23}$$

where s is the shape of the pulse, a_0 and a_1 are heights of the pulses, t_0 and t_1 are the arrival times of these pulses ($t_0 < t_1$) and b is the baseline. The pulse, which we are now interested in, is the later pulse arriving at time t_1, but it is disturbed by the previous pulse arriving at time t_0. The measured signal m consists of noise n, and the measured signal m can be written as $m(t) = f(t) + n(t)$. The estimated pulse shape $\hat{s}$ is calculated averaging many pulses and normalized so that $\max(\hat{s}) = 1$. Unlike in Wiener filter, extra constraints are used. The constraints discussed by Alpert in the paper [56] are orthogonality between filter g and different functions, for example, a constant function or an exponential function. The problem can be formulated in a following way:

$$\text{minimize } \hat{\text{V}}\text{ar}[\hat{a_1}] \tag{24}$$

$$\text{subject to } c_k(x, y) = 0,$$

where $\hat{\text{V}}\text{ar}[\hat{a_1}]$ is the variance of the pulse height, k is the number of constraints c. This problem can be solved using the method of Lagrange multipliers, and the exact solution is derived in reference [56]. The default filtering used at the University of Jyväskylä is Alpert filter with orthogonality constraint to constants only, $V = [v_1] = [(1, , \ldots, 1)]$. This constraint was demonstrated in the paper of Alpert [56] to be as good as the Wiener filter for a situation with some pile-up, but it outperformed the Wiener filter in case of high count rate.

In case of high count rate another Alpert filter that is orthogonal to constants and exponential tail (previous pulse tail) can be very useful. This filter provided 45% increase in peak area and also had almost 10% better energy resolution compared to the Wiener filter when a single pixel count rate was 13.15 Hz. On the downside, the Alpert filter orthogonal to constants and exponential tail had 12% worse energy resolution compared to the Wiener filter when a single pixel count rate was 2.13 Hz.

5.2 Energy calibration

It is a well-known fact that the response of the transition-edge sensor is non-linear because the $R(T)$-curve of the superconducting transition is non-linear. Currently, there exists no reliable physical model for the calibration, and thus a purely mathematical model is used. In our case, a cubic spline function is used. The advantage of this model is that even the most complicated shapes can be approximated, but the disadvantage is that the reliability outside the fit region is poor, especially at high energies close to the saturation energy. That is why a good calibration sample is necessary. In our case, a calibration sample consisting of Si, Ge, Cu, Cr and Ti and X-rays between 1.74 keV and 9.89 keV is used. This is the energy region we are most interested in.

The calibration process is automated with a self-made algorithm. First, peaks are identified with a peak finding algorithm from the uncalibrated spectrum. Then user gives the main peaks in the spectrum, for example, Kα peaks of the main elements in the calibration sample. Then every (uncalibrated peak, energy)-combination is checked until the obtained cubic spline function is acceptable. The function is considered acceptable if it is a rising function, and the difference between the smallest slope and the highest slope is small (usually a factor of two or less is considered small). Then minor peaks in the spectrum, for example, Kβ peaks of major elements or Kα peaks of minor elements are added to the calibration one by one if an (uncalibrated peak, energy)-combination, that is considered acceptable is found.

5.3 Drift corrections

5.3.1 Temperature drift

The transition-edge sensor is an extremely sensitive device both in good and bad. During the measurements, the baseline (input voltage of the feedback loop) can

drift, which can be caused by a temperature drift, for example. Because the response of the transition-edge sensor is non-linear, the X-ray with the same energy does produce pulses with different heights depending on the baseline level. Since these drifts are very small a linear approximation is used.

The simplest drift correction is an energy independent correction. With this correction, a single X-ray line is chosen, and the change in energy versus the change in the baseline drift is fitted using linear fit. Using the obtained slope ($E/\text{pulse height}$), the correction can be performed for all pulses. This correction is sufficient when the measurement is done at narrow energy range where the energy response of the detector is nearly linear.

When measuring wider energy range, $> 1\,\text{keV}$, we need to start taking into account the non-linearity of the detector. Let's define our energy calibration function as $cal\,(ph)$, which takes a pulse height as an input and gives the energy as the output. The drift corrected energy E_{dc} is calculated as

$$E_{dc} = cal\,(ph + \Delta) - cal\,(\Delta)\,, \tag{25}$$

where ph is the analyzed pulse height, and Δ is the drift of the baseline in the same unit as ph. Next we need a correction for the constant drift term Δ. We have to remember that the pulse with height Δ and the baseline change of Δ will not give the same thermal response. For this reason, a correction term α is introduced, and the equation for the drift correction is now

$$E_{dc} = cal\,(ph + \alpha \cdot \Delta) - cal\,(\alpha \cdot \Delta)\,. \tag{26}$$

In practice, the energy calibration at low energies ($\ll 1\,\text{keV}$) using the standard spline fitting can behave very non-linearly, although it is known to be almost linear. Thus in practice at low energies, a 2nd order polynomial is used, and when allowing $cal(0) \neq 0$, we will arrive at the final form of the drift corrected energy

$$E_{dc} = cal_{HE}\,(ph + \alpha \cdot \Delta) - cal_{LE}\,(\alpha \cdot \Delta) + cal_{LE}\,(0)\,, \tag{27}$$

where HE refers to the standard cubic spline energy calibration at high energies and LE refers to 2nd order polynomial calibration at low energies. The principle of this drift correction is visualized in Figure 16.

5.3.2 Other drifts

From time to time, we can notice drifts that are not related to the changes in baseline, but instead, they stem for example from problems at SQUIDs. Unlike regular drifts, these are sharp shifts as illustrated in Fig. 17, and the shifts are

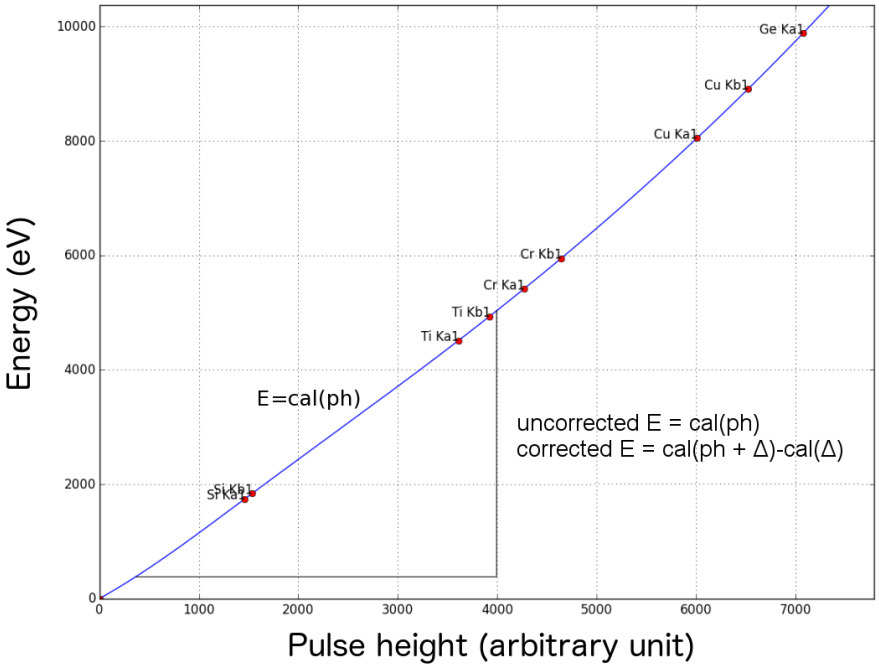

FIGURE 16 The basic principle of energy-dependent drift correction calculation using the energy calibration curve as a basis. Because the calibration is non-linear, for different baseline levels the pulse height is different for X-rays with the same energy.

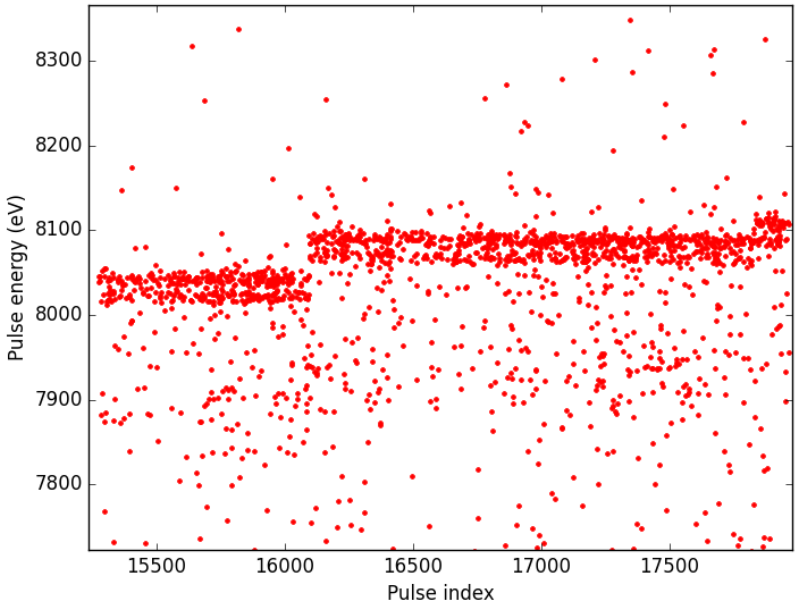

FIGURE 17 An example of non-continuous drift caused most likely by some sort of SQUID problem. There are two jumps visible, one at 16100 and the other at 17700.

typically a few tens of eVs, and they can be seen in spectra as peak doubling. In practice, this correction is done by fitting a simple step function to the data. This correction has an unknown energy-dependency, but a correction proportional to energy seems to work well in most cases for energy range from 4 to 10 keV, but not below it. Thus a correction applied to different regions may be necessary.

5.4 Graphical interface

A graphical user interface has been developed for analyzing the data from transition-edge sensors. The interface is written using python2.7 and Qt5 (Qt4 is also supported). Thus the program should run in any major computer environment. This new interface allows a more user-friendly way for the TES pulse processing, including cutting the bad data, calculating different optimal filters, tools for energy calibration, drift corrections, and various data visualization options. In Figure 18 the graphical interface shows raw pulse records from the measurement data.

Graphical interface also provides a peak fitting tool optimized for high-resolution spectrum, but it can be used for fitting any X-ray emission spectra. Peak fitting tool includes automatic peak identification, fitting of multiple ionization peaks, fitting of an exponential tail, and the X-ray energies are allowed to deviate from the tabulated values. Peak fitting tool is integrated with libCPIXE library[54], and the analysis and the simulation of multilayered samples are supported for proton-induced X-ray emission. Peak fitting tool is demonstrated in Figures 19, and 20.

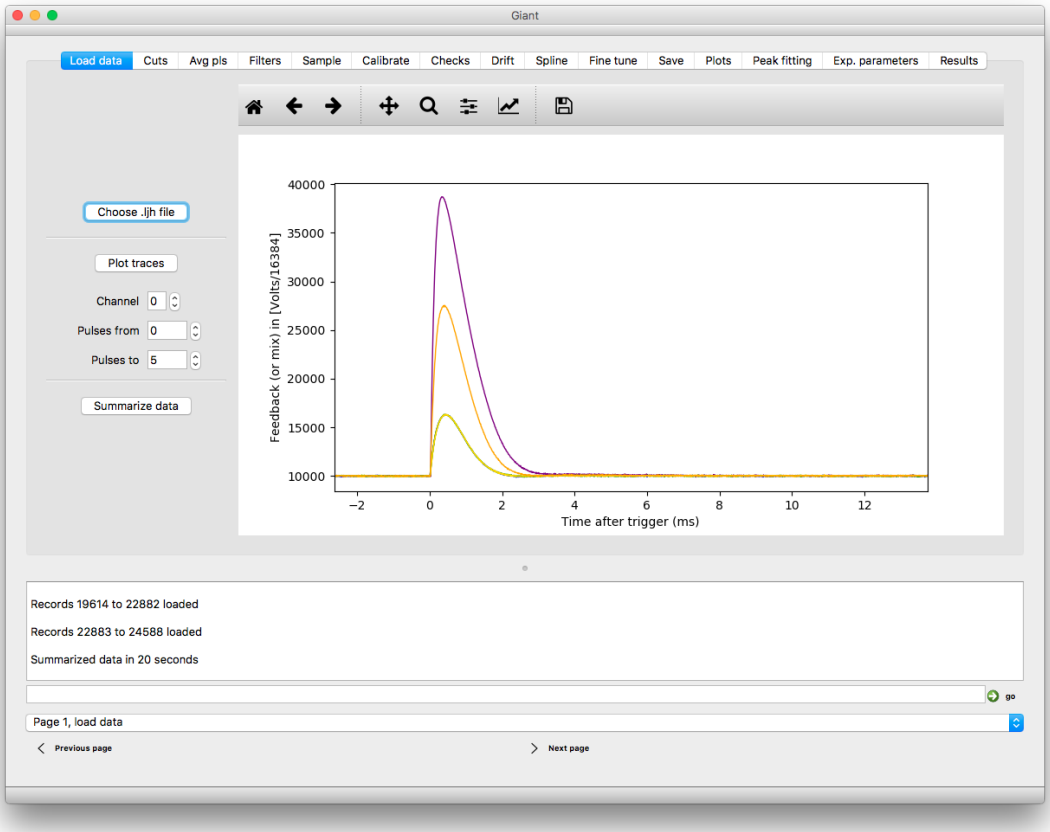

FIGURE 18 Graphical interface for transition-edge sensor (TES) pulse processing. Three TES pulses are visualized in the figure.

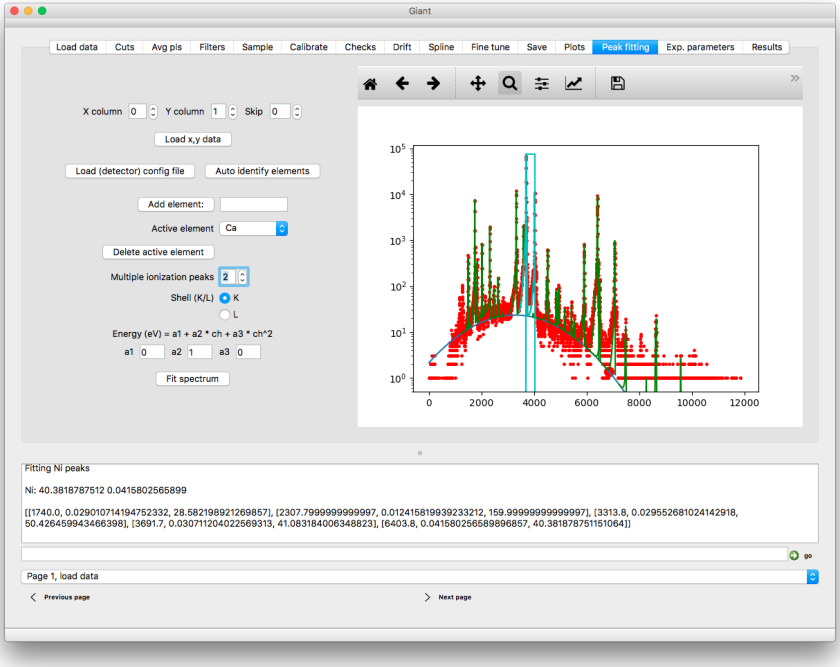

FIGURE 19 Fitting of a high-resolution spectrum, including features such as an automatic element detection, fitting of detector parameters, fitting of multiple ionization X-ray satellite lines, and fitting of overlapping peaks.

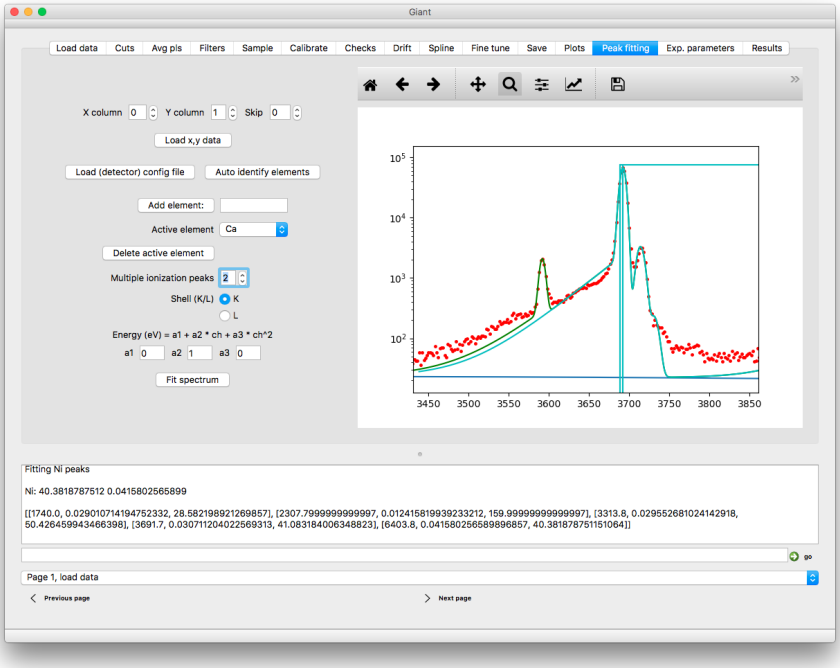

FIGURE 20 Detailed region showing the ability to fit multiple ionization peaks, exponential tail, and overlap.

6 QUANTITATIVE ELEMENTAL ANALYSIS USING TES-PIXE

6.1 Measurements in vacuum

Transition-edge sensors (TES) at the University of Jyväskylä have 2.5 µm thick Bi absorbers, the system is isolated from the outside using Moxtek Inc. AP3.3 vacuum window, and inside the vacuum there are three in-house manufactured infrared filters with a composition of a 225 nm thick Al layer on top of a 280 nm thick silicon nitride membrane on each. In the vacuum measurements a 125 µm thick Be foil was used as an ion filter.

We used two standard reference materials, NIST SRM 1157 (stainless steel) and NIST SRM 611 (glass with added impurities), to calibrate the TES array efficiency. The main elements in the SRM 1157 sample are Mn, Si, Ni, Cr, V, Mo, W, and Fe. The nominal matrix composition of the SRM 611 glass is 72% SiO_2, 14% Na_2O, 12% CaO, 2% Al_2O_3 (mass fractions, not including impurities). The SRM 611 sample contains also 61 additional elements with a nominal 500 ppm concentration. Spectra of the SRM 1157 and the SRM 611 reference samples are shown in Figures 21 and 22, respectively.

The detector efficiency was calculated with the help of GUPIXwin program [57]. GUPIXwin was used to calculate X-ray yields, filter transmissions, etc. The peak fitting of GUPIXwin was not satisfactory for high-resolution data, and it was done manually. With the known composition of reference samples, the known X-ray yields, and peak areas the only unknown parameter left is the detector efficiency which then could be determined. The analyzed detector efficiency, as well as theoretically expected efficiency and its components, are plotted in Figure 23.

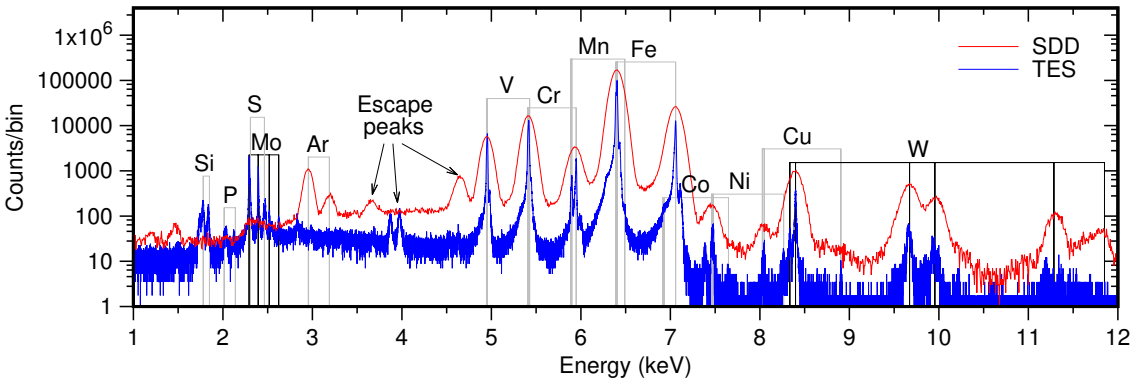

FIGURE 21 An X-ray spectrum of the NIST standard reference material SRM 1157 (tool steel), measured using a transition-edge sensor (TES) array and a silicon drift detector (SDD). Note that the escape peaks in the SDD and TES spectra appear at different positions; circa 1.75 keV below the intrinsic X-ray line for SDD and circa 2.4 keV below the intrinsic X-ray line for TES. The SDD spectrum was collected using an external beam, and the TES spectrum was collected in vacuum, thus the Ar peaks are visible only on SDD spectrum.

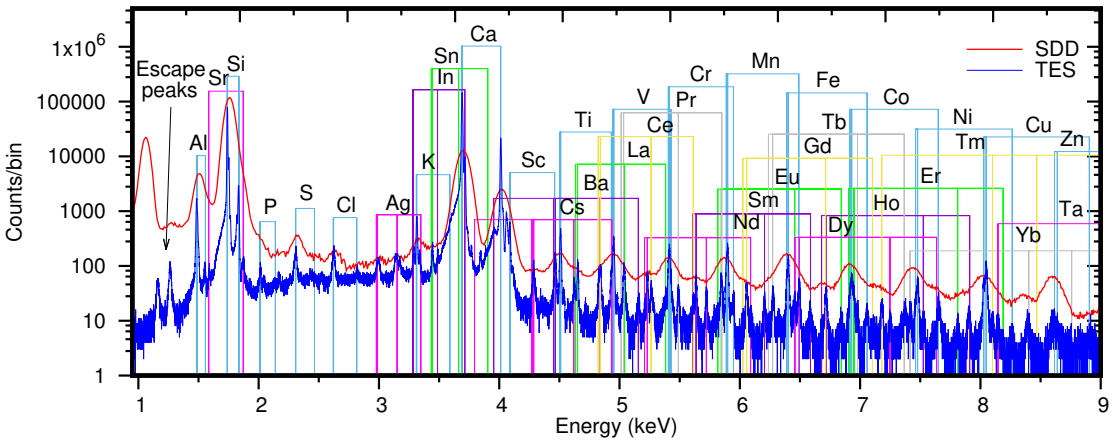

FIGURE 22 An X-ray spectrum of the NIST standard reference material SRM 611 (glass with impurities), measured using a transition-edge sensor (TES) array and a silicon drift detector (SDD). Note that the escape peaks from the SDD and TES appear at different positions; circa 1.75 keV below the intrinsic X-ray line for SDD and circa 2.4 keV below the intrinsic X-ray line for TES.

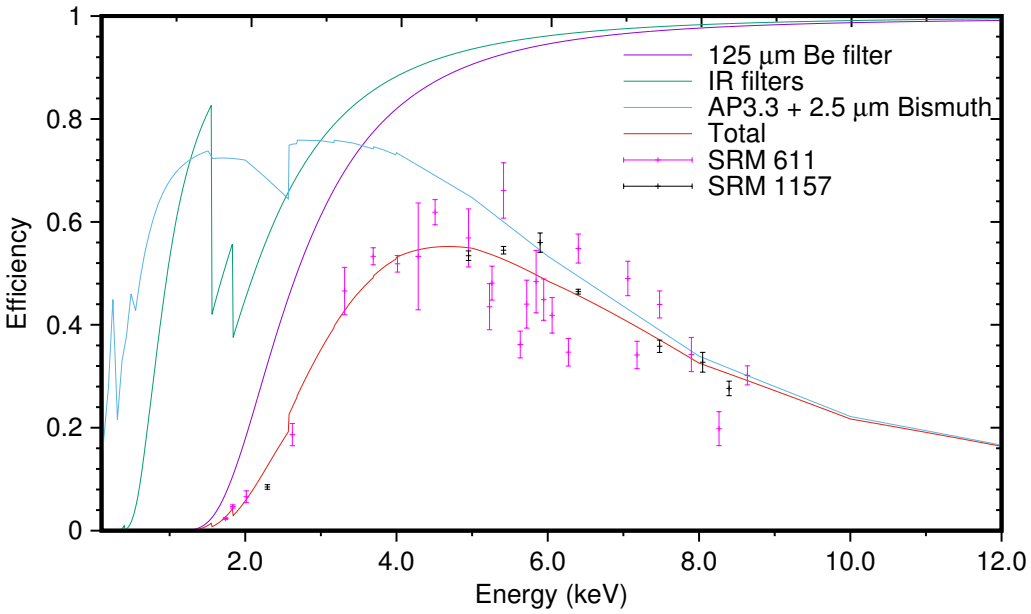

FIGURE 23 Calibrated transition-edge sensor array efficiency using two reference materials, the NIST SRM 611 (glass with impurities), and the NIST SRM 1157 (tool steel). The points and squares are experimental data, and the solid lines are calculated values.

6.2 External beam development and characterization

We have designed and built a new beamline with options for external beam and vacuum chamber measurements using the transition-edge sensor array. The new beamline is visualized in Figure 24 and the external beam setup in Figure 25.

A critical part of the design was a polycapillary lens which allows detection of low energy X-rays while stopping scattered proton beam [29]. The polycapillary lens is attached to a plastic snout which is in He atmosphere as well as the space between the plastic snout and the sample. The polycapillary lens was designed in co-operation with IfG - Institute for Scientific Instruments GmbH. We wanted to increase X-ray intensity gain at lower energies while maintaining good efficiency up to 8 keV. In Figure 26, gains for 5 different polycapillary lens designs are plotted, the solid line is the chosen design. As can be seen from Figure 26, the design is always a compromise between efficiency at low and high energies. Sudden drops in the gain are caused by the X-ray absorption edges of the Si, and O (SiO_2 was used as a capillary material in the simulations).

To characterize the gain of the polycapillary lens, I measured two calibration samples having calibration energies ranging from O Kα_1 to Cu Kα_1. The first sample measured was the NIST standard reference material SRM 611. The second calibration sample was fabricated by means of electron beam evaporation on top of

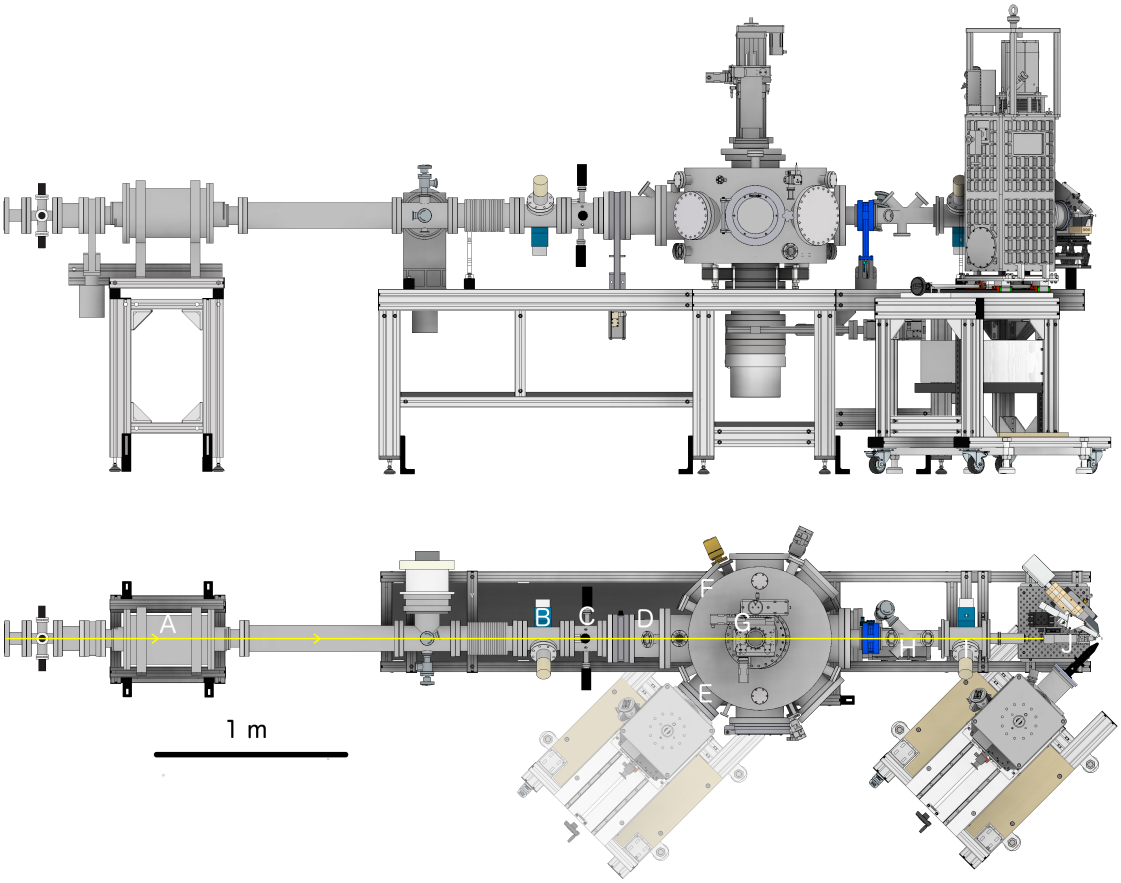

FIGURE 24 Two CAD-images of the new beamline at the University of Jyväskylä. The new beamline is dedicated for the PIXE and RBS measurements. In both images the ion beam comes from left to right (yellow line in the figure). In the bottom image following are shown: A = wobbler, B/I = beam profile meter (BPM), C = motorized slits, D = RBS chopper, E = mounting flange for the TES array, F = mounting flange for a silicon drift detector or a CdTe detector, G = goniometer, H = fluorescent screen, J = external beam setup, see Fig. 25.

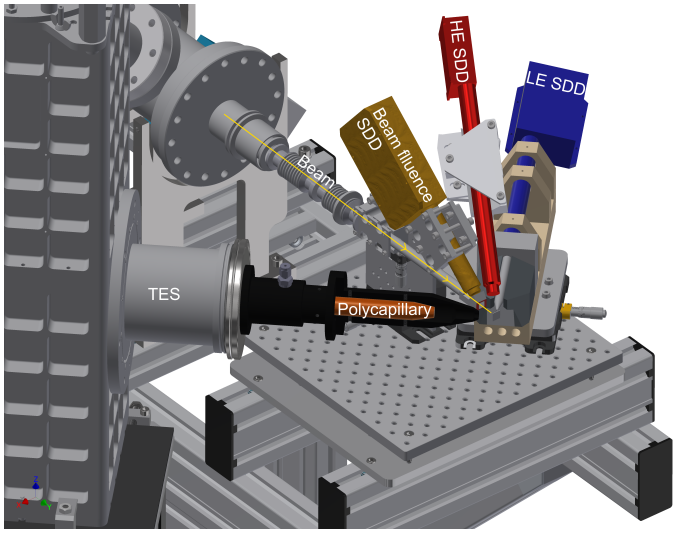

FIGURE 25 A CAD-image of the new external beam PIXE setup at the University of Jyväskylä. In the image the TES array, beam fluence normalization detector (beam fluence SDD), low-energy silicon-drift detector (LE SDD), high-energy silicon-drift detector (HE SDD), polycapillary lens alignment snout, and metallic polycapillary container are shown. The proton beam goes from the top-left corner towards bottom-right corner.

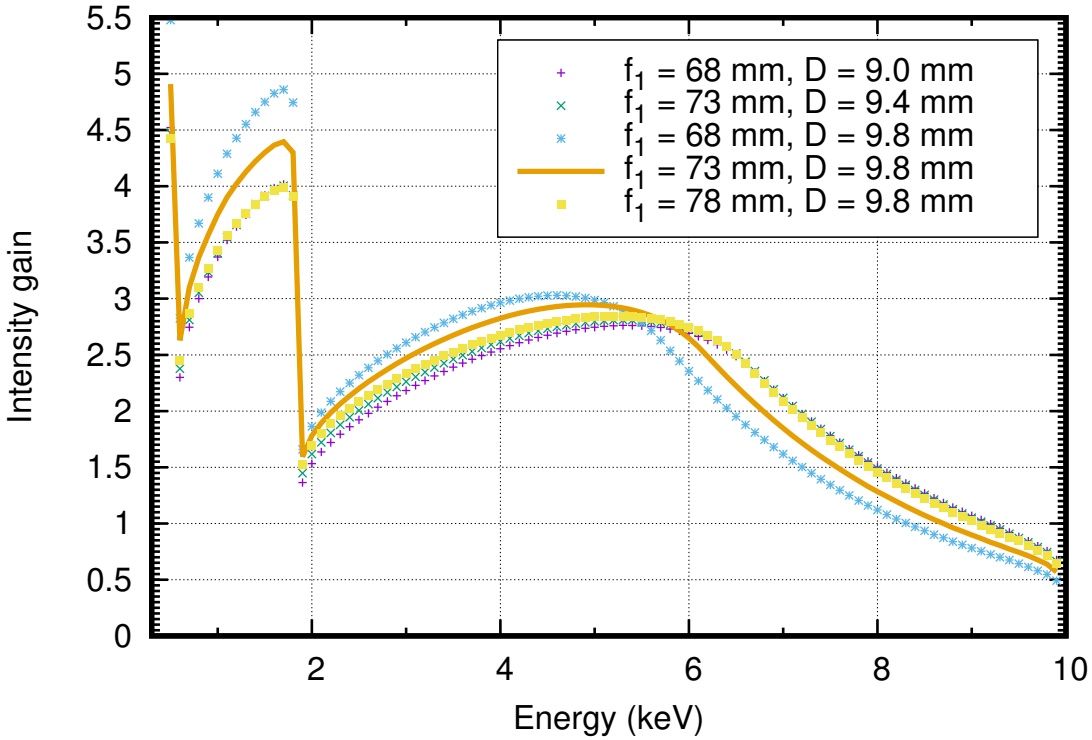

FIGURE 26 Calculated gains for five different polycapillary lens designs. The distance between the sample and the polycapillary lens is f_1, and the input diameter of the polycapillary is D. The solid line is the chosen design. The capillary material in calculations is SiO_2. It can be noticed, that the design is a compromise between the efficiency at low and high energies.

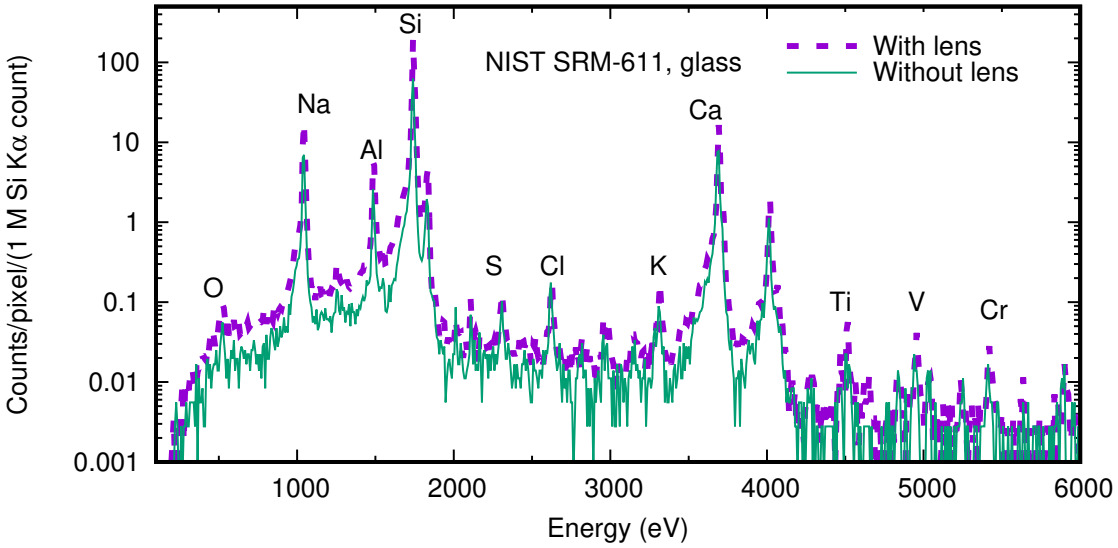

FIGURE 27 Measured PIXE spectra of the NIST SRM 611 with 72% SiO_2, 14% Na_2O, 12% CaO, 2% Al_2O_3 nominal matrix composition. Intensity is divided with number of pixels used in the analysis and with counts/million in Si Kα area from the exit window. The dead times of the detectors were taken into account.

C substrate. The second calibration sample contains following thin films from top to bottom: 14 nm Al, 10 nm Nb, 25 nm Ag, 65 nm Ti, 115 nm Fe, 185 nm Ni, and 300 nm Cu, and 70 nm Cr.

The measurements were performed in the same day first by measuring both samples with the polycapillary lens and then both samples without the polycapillary lens. Detector geometries, He atmosphere, sample positions and beam energy were kept the same in both measurements. The proton energy 1.7 MeV was chosen so, that the proton beam stops in the He atmosphere even without the polycapillary lens. For the common 3.0 MeV proton beam, a polycapillary lens or some other proton filter is needed. The beam fluence was monitored by measuring Si Kα intensity from the Si_3N_4 exit window. The measured spectra are shown in Figures 27 and 28.

Analyzed polycapillary gain and the calculated polycapillary gain for different glass compositions is plotted in Figure 29. For theoretical calculations we used three different borosilicate compositions: 1) 81% SiO_2, 13% B_2O_3, 2% Ca_2O, 2% K_2O, 2% Al_2O_3, 2) 81% SiO_2, 13% B_2O_3, 2% Ca_2O, 2% K_2O, 2% Al_2O_3, 1% Pb, 3) 65% SiO_2, 25% B_2O_3, 2% Ca_2O, 8% K_2O, 4) same as 1), but with 1.3 nm RMS roughness. The exact composition of the borosilicate glass was not known and thus we used different compositions to compare to the experimental data. For the reference, the total overall efficiency (not comparable with experimental points), taking into account X-ray transmission through vacuum window, He atmosphere, IR-filters and detector absorber, is shown.

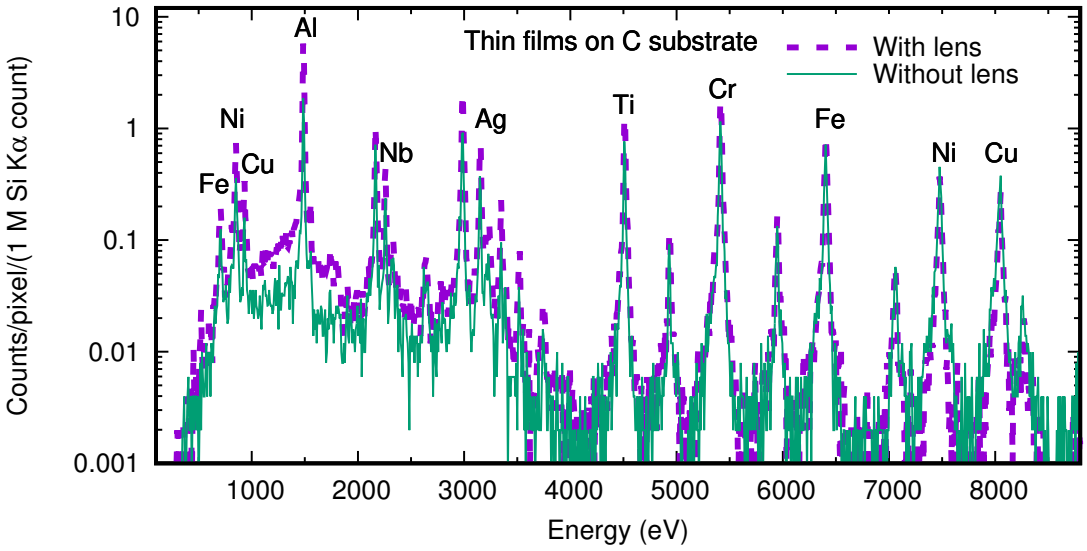

FIGURE 28 Measured PIXE spectra of an in-house fabricated sample with Al, Nb, Ag, Ti, Cr, Fe, Ni, Cu thin films on top of C substrate. Intensity is divided with number of pixels used in analysis and with counts/million in Si Kα area from the exit window. The detector dead times were taken into account.

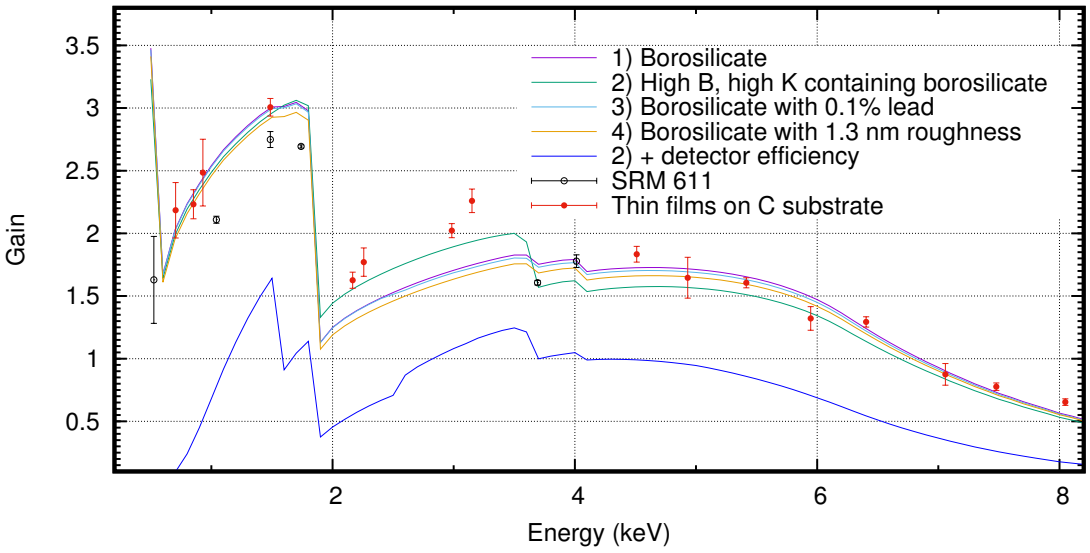

FIGURE 29 Experimental and theoretical X-ray intensity gains for the polycapillary lens. For the theoretical calculations four different borosilicate glass compositions were used: 1) 81% SiO_2, 13% B_2O_3, 2% Al_2O_3, 2% Ca_2O, 2% K_2O; 2) 65% SiO_2, 25% B_2O_3, 2% Ca_2O, 8% K_2O, 3) same as 1), but with additional 0.1% Pb, 4) same as 1) but with 1.3 nm RMS roughness (all values are in mass percentages). The bottom-most (blue) line is the total efficiency of the system with polycapillary composition 2) including the X-ray transmission of the He atmosphere, vacuum window and IR-filters.

6.3 Analysis example

The transition-edge sensor array was used in the analysis of a fly-ash obtained from Jyväskylän Energia, and the spectrum is shown in Figure 30. In the TES spectrum, Ba, Ce, and V are clearly separated, but they severely overlap in the SDD spectrum. We determined the minimum detection limits for these elements in this sample. A common definition for minimum detection limit can be written as

$$Y_{MDL} = 3 \cdot \sqrt{b_{fwhm}}, \tag{28}$$

where b_{fwhm} is the background area in the full width at half maximum region [11]. This definition is valid in the situation where the peak height is much higher than the background level, and the peaks are well separated [58]. If that is not the case we can write

$$Y_{MDL} = C \cdot FWHM^n, \tag{29}$$

where C is a constant, $n = 0.5$ for non-overlapping peaks (peaks more than 2 FWHM apart), $n = 1.5$ for severe overlap of two peaks (peaks less than 1/10 FWHM apart), and n =0.5–1.5 when there is some overlapping [58]. In these measurements, the resolution was 6.6 eV for the TES array and 145 eV for the SDD. Assuming the same detection geometry and efficiency, we can calculate that the MDL improves by a factor of 620 ($n = 1.4825$ for SDD), 400 ($n = 1.3947$ for SDD), and 680 ($n = 0.5$ for TES array) for V, Ba, and Ce, respectively.

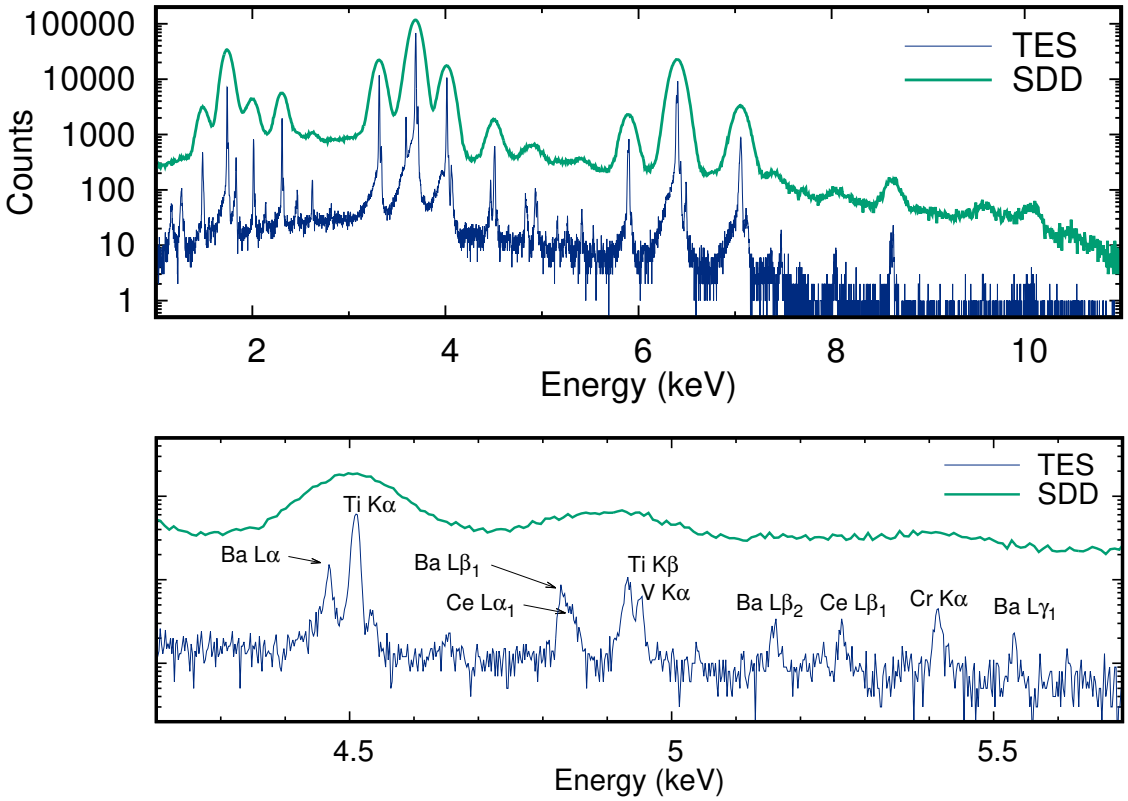

FIGURE 30 Measurement of fly ash from a power plant using a silicon drift detector (SDD), and a transition-edge sensor array (TES). Peaks not visible in SDD spectrum (e.g. Ba Lα and V Kα) can be revealed using high-energy resolution TES.

7 CHEMICAL SPECIATION OF TITANIUM COMPOUNDS WITH PIXE

Different titanium compounds are highly relevant in many fields. For example, a thin titanium nitride coating can be used to harden and protect surfaces [59]. PIXE has been used for chemical speciation with wavelength-dispersive detectors for many decades [34], but energy-dispersive detectors capable of good enough energy resolution to do chemical speciation have not been available until recently [60, 61]. With high-energy resolution, energy-dispersive detectors it is possible to see all elements (except for the lightest elements) in the sample and to detect finer details in X-ray lines. These details can be used for chemical speciation of many compounds, including some titanium-containing compounds [62, 63].

7.1 Proton measurements

We measured three titanium-containing thin films: 400 nm Ti, 450 nm TiO_2, and 500 nm TiN. All films were grown on top of Si wafer. Metallic Ti was deposited using electron beam evaporation, and the rest with atomic layer deposition (ALD). For the ALD-grown samples, $TiCl_4$ and H_2O were used as precursors for TiO_2, and $TiCl_4$ and NH_3 were used as precursors for TiN. The compositions of TiO_2 and TiN thin films were verified by time-of-flight elastic-recoil-detection analysis. In both films, there were C and H at the surface. In the film, the atomic concentrations for impurities were below 0.5% for TiO_2, and below 2% for TiN sample. The Ti:O and Ti:N ratios were 1:2.3 and 1:1.3 for TiO_2 and TiN, respectively.

In Figure 31 a close-up region of titanium Kα peak is shown. A chemical shift of (1.1 ± 0.3) eV was observed for TiO_2, but no shift was observed for TiN when compared to pure Ti sample.

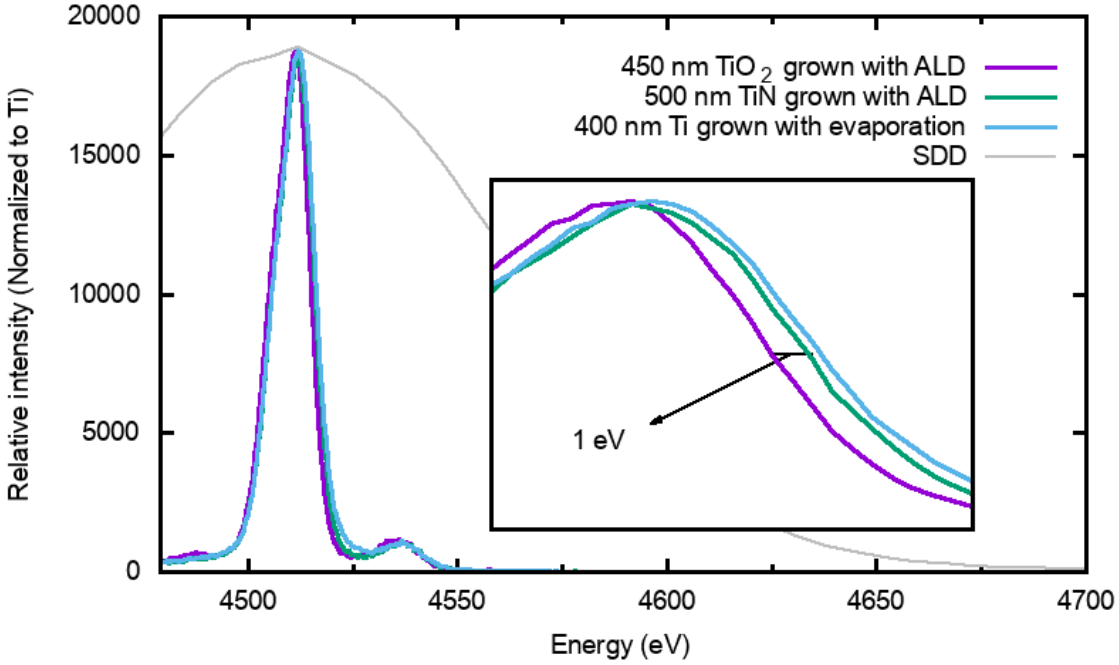

FIGURE 31 Ti Kα X-ray line of three different titanium thin films measured with a 2.0 MeV proton beam. X-rays were detected using the transition-edge sensor array, and for comparison, a silicon drift detector (SDD) spectrum is shown in the background. The peak on the high-energy side of the Ti Kα peak is a multiple ionization X-ray line KL^1.

7.2 Heavy ion measurements

Three titanium-containing films on Si substrate, a 50 nm thick Ti layer, a 50 nm thick TiO_2 layer, and a 50 nm thick TiN layer, were measured with seven different $^{12}C^{3+}$ ion energies from 4.4 MeV to 6.8 MeV, as well as with 4.8 MeV $^{12}C^{2+}$, 5.1 MeV $^{7}Li^{2+}$, 6.8 MeV $^{16}O^{3+}$ and 11.9 MeV $^{63}Cu^{6+}$ beams. For the ALD-grown samples, $TiCl_4$ and H_2O were used as precursors for TiO_2 (growth temperature was 350 °C), and $TiCl_4$ and NH_3 were used as precursors for TiN (growth temperature was 400 °C). The compositions of thin films were verified using ToF-ERDA. All ToF-ERDA measurements were done after the heavy ion PIXE measurements. In all films, there were C and H impurities in the surface. The compositions in the films are summarized in Table 3. We could see some impurities in the films, but the main compositions of the films were as expected.

Measured spectra are shown in Figures 32 and 33. Compared to the proton measurements (see Fig. 31), more multiple ionization X-ray lines are seen and they have much higher intensity. The Ti Kα peak in the heavy ion spectra is much wider compared to the proton measurements. With heavy ions, more M-shell electrons are ionized, creating a distribution of M-shell vacancies and this is the main contributor for the widening of the peaks [34].

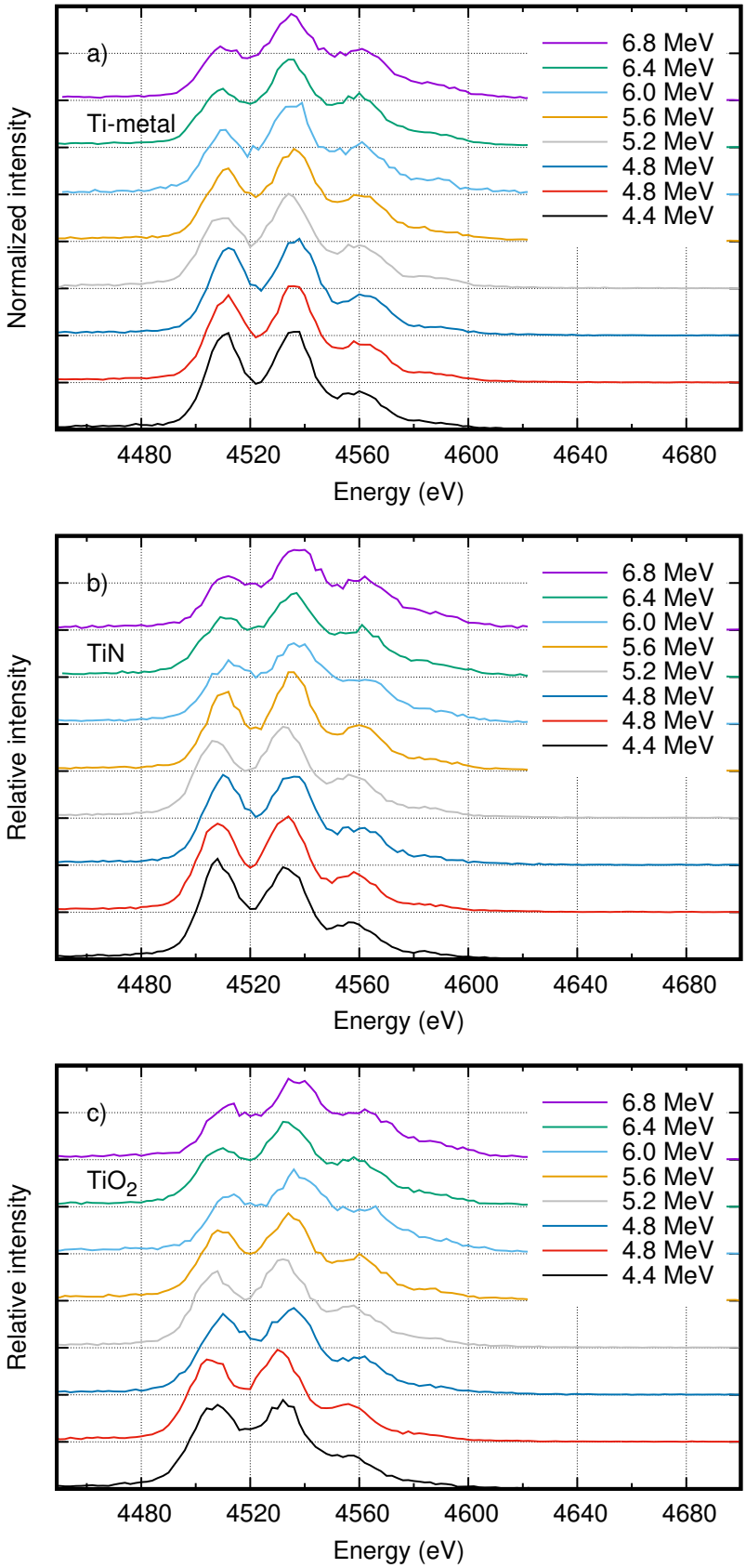

FIGURE 32 Ti Kα X-ray satellite lines of Ti-metal, TiN and TiO_2 samples measured with 4.4–6.8 MeV $^{12}C^{3+}$ beams, and 4.8 MeV $^{12}C^{2+}$ beam (red line).

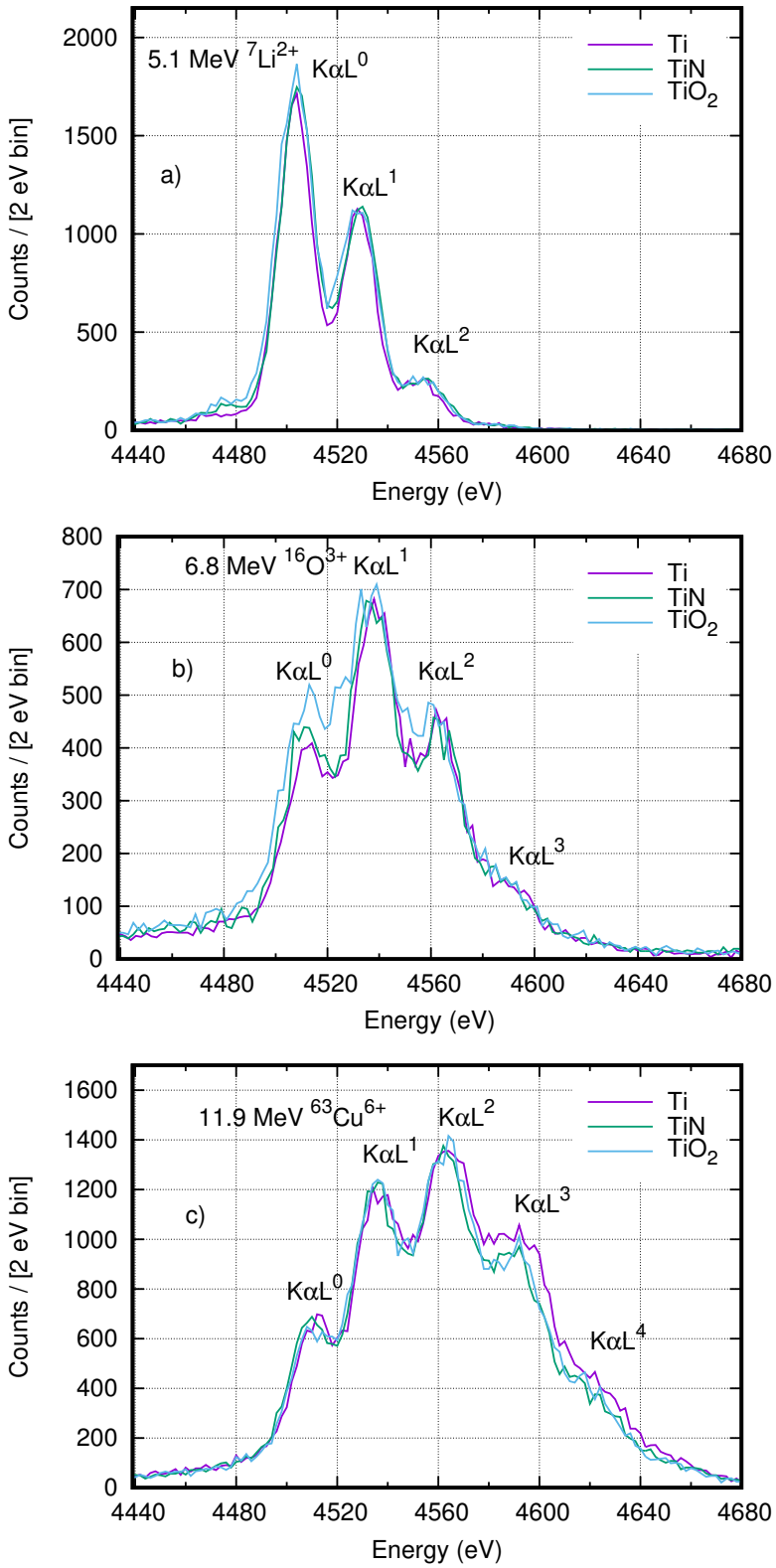

FIGURE 33 Ti Kα X-ray satellite lines of Ti-metal, TiN and TiO_2 samples measured with 5.1 MeV $^{7}Li^{2+}$, 6.8 MeV $^{16}O^{3+}$ and 11.9 MeV $^{63}Cu^{6+}$ beams. Intensity of TiN, and TiO_2 samples are scaled against the fitted height of the highest satellite line of the Ti-metal sample. The y-axis shows the numerical value of peak height for Ti-metal sample.

TABLE 3 Elemental compositions (in atomic percentages) for the measured thin film samples. Measurements were performed after PIXE measurements using time-of-flight elastic-recoil-detection analysis. In each sample there was C and H contamination on the surface, the composition given here is for the film.

Sample	H	C	N	O	Ti
Ti	4.1 ± 0.2	2.8 ± 0.2	0.07 ± 0.03	4.0 ± 0.2	89.0 ± 0.9
TiN	0.88 ± 0.09	4.7 ± 0.2	47.7 ± 0.7	3.3 ± 0.2	41.7 ± 0.5
TiO_2	0.48 ± 0.06	2.36 ± 0.15	0.10 ± 0.03	65.3 ± 0.7	31.2 ± 0.4

Data was analyzed in a list mode to ensure there was no beam damage affecting the results. In Figure 34 a) relative peak position of Ti Kα and b) KL^0 fraction is plotted as a function of the measurement real time. It can be noted that some shifts occur in the energy. The drifts in peak positions happen because of the limitations in drift correction algorithm used. The algorithm (Ref. [64]) is optimized for narrow X-ray lines, not for complicated and wide X-ray satellite structures, making it less reliable in this situation. Due to the relatively small statistics, wide peaks, and peak overlapping, we cannot perform energy correction with high enough accuracy to reliably give absolute peak positions, like we did in the case of the proton beam. The KL^0 fractions are stable through measurements, with the except of few data points, but this is due to a fit reaching a little different peak shape compared to the other fits. For these reasons, we conclude that no beam damage affecting the results occurred during the measurements.

Relative intensities, KαL^0, KαL^1, KαL^2 and KαL^3, for different titanium thin films (Ti, TiN, TiO_2) measured with seven different $^{12}C^{3+}$ beam energies: 4.4 MeV, 4.8 MeV, 5.2 MeV, 5.6 MeV, 6.0 MeV, 6.4 MeV and 6.8 MeV are shown in Figure 35, and the apparent average L-shell ionization fraction is plotted in Figure 36. In a previous study, a correlation between p_L and average valence shell electron density D_v was found [35]. Our measurements follow this same trend. Calculated values for D_v are 0.227, 0.456, 0.457, for Ti, TiO_2, and TiN, respectively and p_L values of TiN, and TiO_2 fall in the same line whereas Ti has higher p_L values. For 11.9 MeV $^{63}Cu^{6+}$ and 5.1 MeV $^{7}Li^{2+}$ ions the same trend in the p_L value was observed. The values for $^{63}Cu^{6+}$ beam were 0.266 ± 0.015, 0.255 ± 0.012, and 0.253 ± 0.013 for Ti, TiN, and TiO_2, respectively. The values for $^{7}Li^{2+}$ beam were 0.066 ± 0.003, 0.062 ± 0.002 and 0.058 ± 0.003, for Ti, TiN and TiO_2, respectively.

The difference between Ti, and other samples can be seen in p_L value, and KαL^0 and KαL^2 fractions. For chemical speciation, KαL^0/KαL^2-ratio and p_L value are the most sensitive and can be used to distinguish Ti from TiN, and TiO_2. With proton beam we could differentiate TiO_2 from Ti, and TiN and with combination of proton and $^{12}C^{3+}$ beam measurements all three samples can be identified.

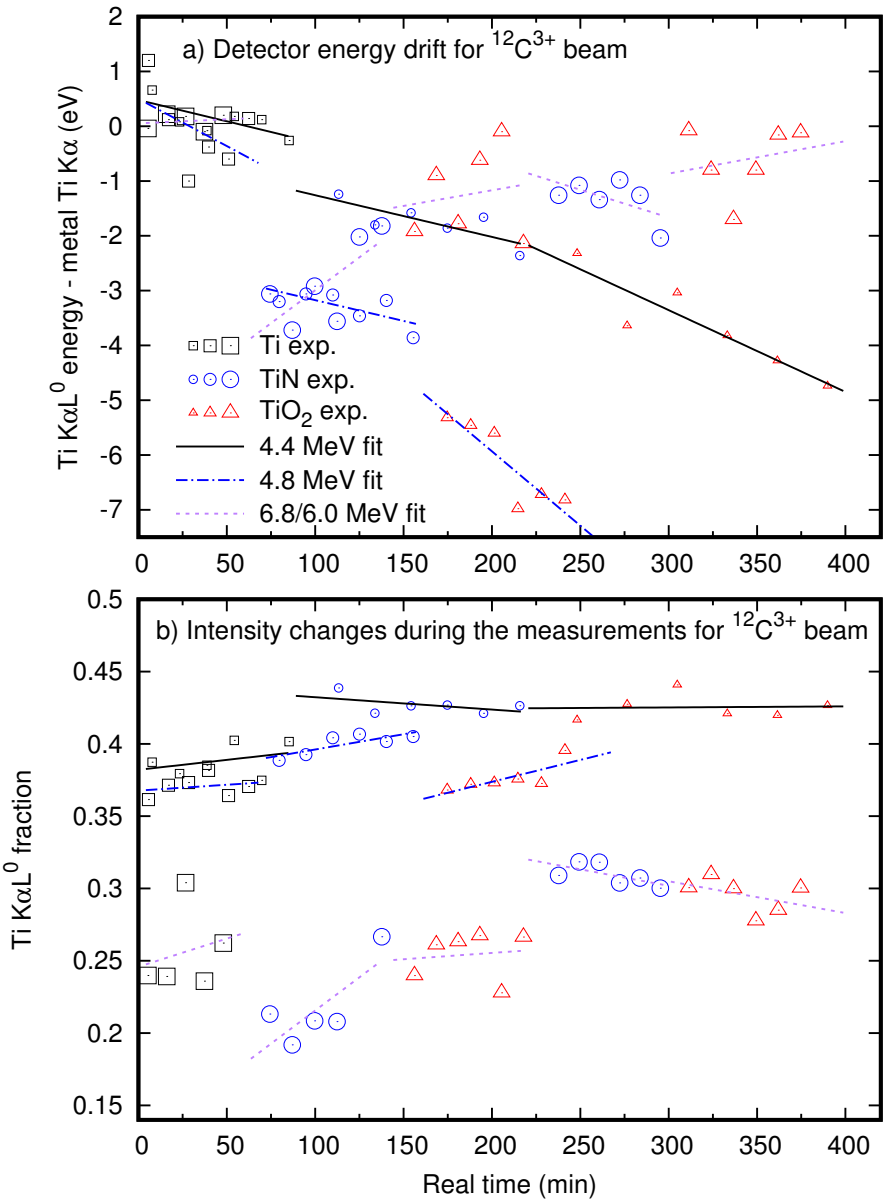

FIGURE 34 a) Relative Ti KαL^0 positions and b) Ti KαL^0 fractions analyzed in list-mode for measurements from three different days. List-mode analysis was done to monitor possible changes in the sample and detector stability during the measurements. The KαL^0 fractions and peak positions for different Ti-containing samples were measured using 4.4 MeV (small symbols), 4.8 MeV (average-size symbols), 6.0 MeV (large symbols), and 6.8 MeV (large symbols) $^{12}C^{3+}$ beams (same symbols are used in both figures). Lines are linear fits to the data points of each sample, and the line style describes a measurement from the same day (real time starts from zero for each day). For the dashed line, first three measurements were performed with a 6.8 MeV $^{12}C^{3+}$ beam, and the last two with a 6.0 MeV $^{12}C^{3+}$ beam. Uncertainties for peak positions are between 0.3 and 0.9 eV, and uncertainties for Ti KαL^0 fractions are between 0.013 and 0.02. Uncertainties are not displayed in the plot for clarity.

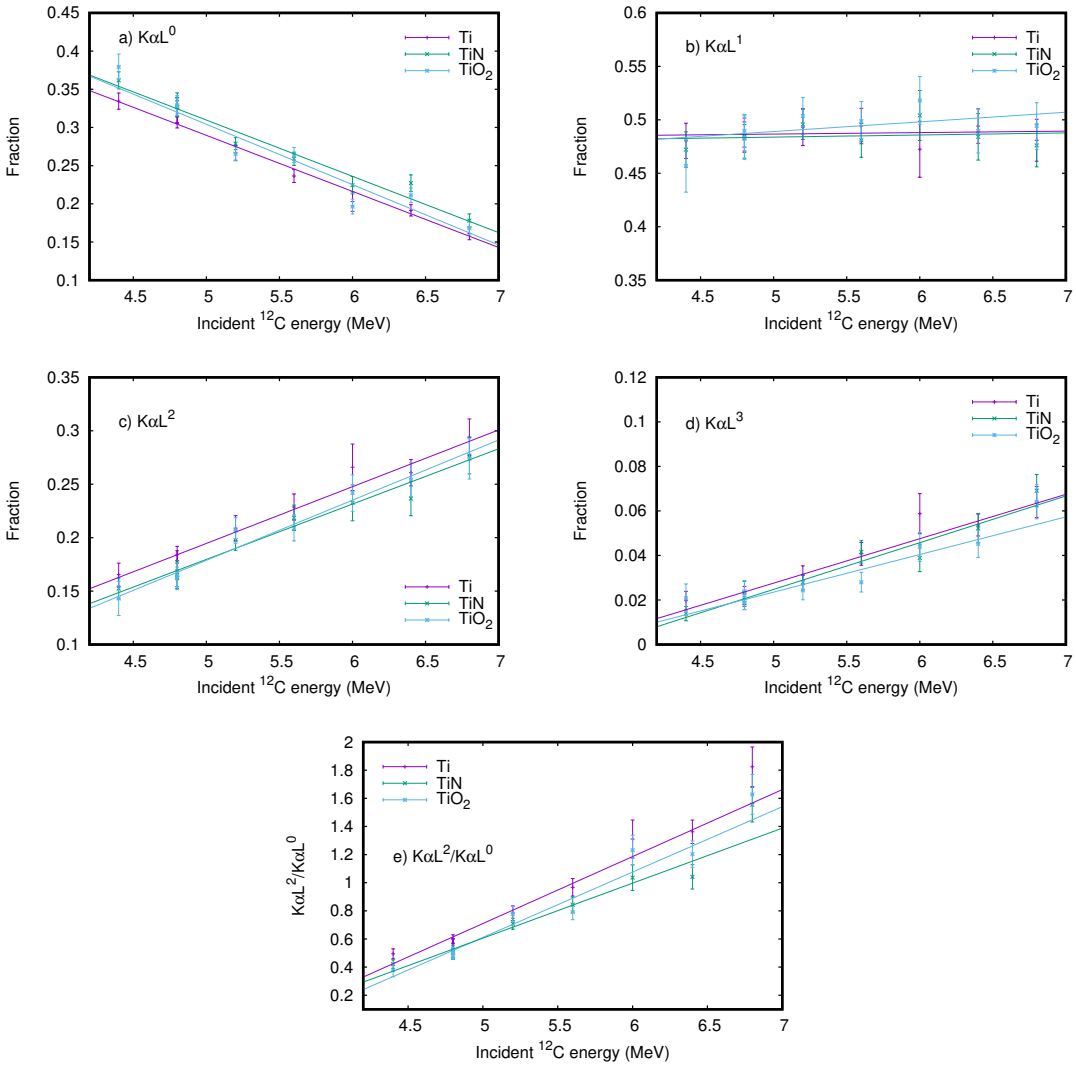

FIGURE 35 Measured a) KαL^0, b) KαL^1, c) KαL^2, d) KαL^3, e) KαL^2/KαL^0 fractions as a function of energy for $^{12}C^{2+/3+}$ ions. Peaks were fitted with the Voigtian peak with an exponential tail. The Gaussian width, corresponding to instrumental resolution, was a constant 6 eV and was fitted using a calibration measurement carried out with a proton beam. All samples had a thickness of circa 50 nm and energy losses in the films were roughly 0.15 MeV in all cases (calculated with SRIM-2013 [65]).

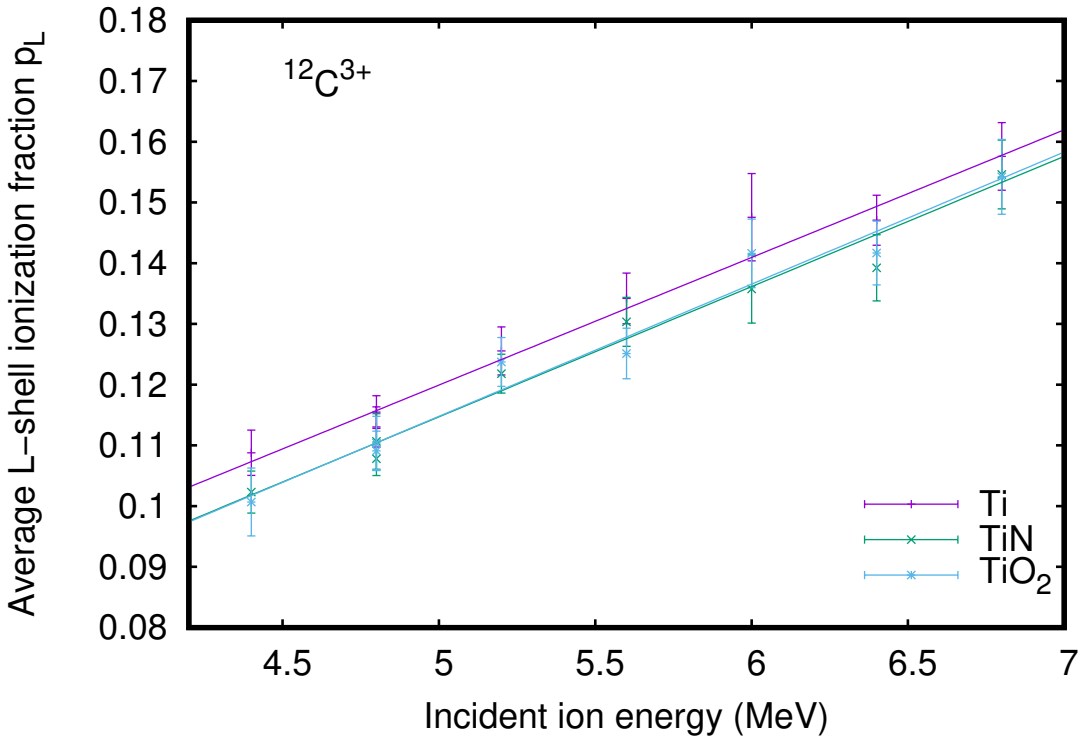

FIGURE 36 The apparent average L-shell ionization p_L during X-ray emission as a function of $^{12}C^{2+/3+}$ ion energy. The higher the value of p_L the more ionized the L-shell of titanium is. All samples were roughly 50 nm thick, and energy loss in the films was approximately 0.15 MeV in all cases (calculated with SRIM-2013 [65]).

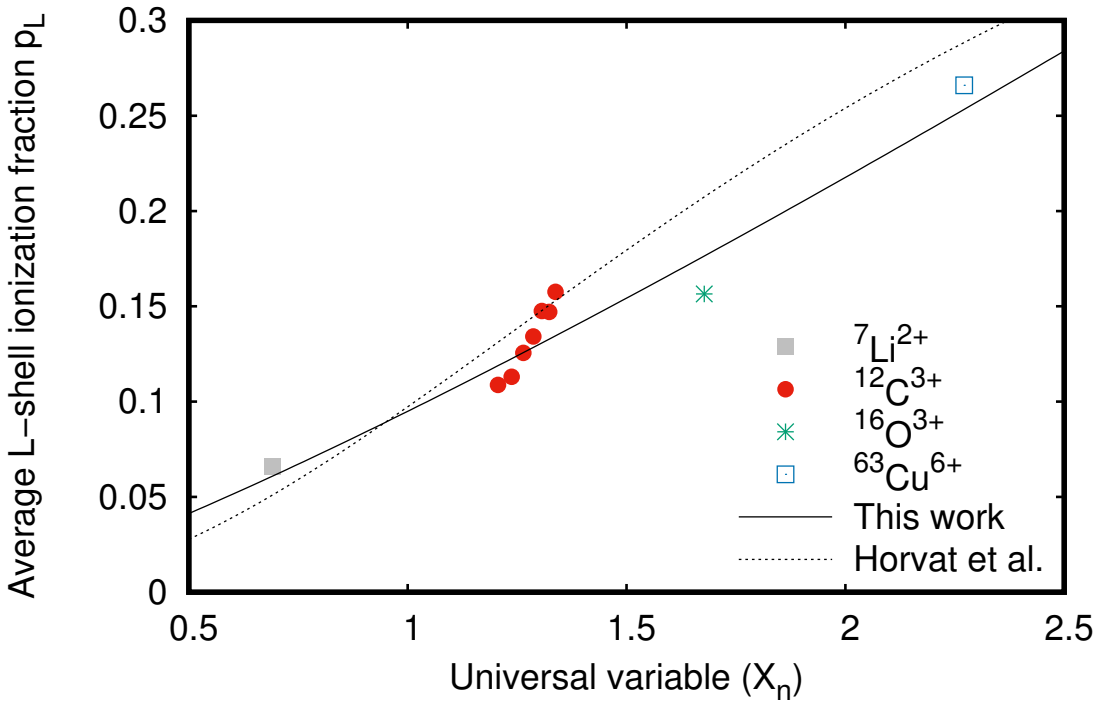

FIGURE 37 The apparent average L-shell ionization p_L at the time of Kα emission as a function of the universal variable X_n (Eq. (14)). X_n is a parameter that describes the perturbation strength of the collision. The energy loss in the film was calculated using SRIM-2013 [65], and the average energy of the incident ion was used to calculate X_n values. We fitted our data points to Eq. (30), and the fit previously made by Horvat et al. [66] is plotted for comparison.

7.2.1 Systematics of Ti Kα X-ray satellites

We have studied the systematics of p_L values for metallic titanium film using the Geometrical Model (GM) (Eq. (14)), and fitted the data using equation

$$p_L = \frac{a}{1 + (b/X_n)^c}. \tag{30}$$

Measured data, the best fit to our data, and fit obtained by Horvat et al. [66] are plotted in Fig. 37. Horvat et al. fitted the universal variable X_n for different p_L values and there the emphasis was on the region $X_n > 2$, and in this work the emphasis is on region $X_n < 2$. The Geometrical Model works also in this region, and difference between the best fit to our data, and fit obtained by Horvat et al. is small (Fig. 37).

8 SUMMARY AND CONCLUSIONS

A transition-edge sensor measurement system has been developed for quantitative analysis in both inside and outside of the vacuum. It is the first time a high-energy resolution, energy-dispersive detector has been installed for external beam PIXE measurements. Using the external beam measurement setup utilizing the polycapillary lens we were able to expand our lowest detectable X-ray energy from 1.4 keV to 0.5 keV. This region opens up a possibility to study many interesting K-, L-, and M-lines, and opens up a possibility for chemical speciation of light elements like fluorine.

We have studied effects of chemical bonding of titanium-containing thin films using different incident ions. We observed energy shift between TiO_2 and Ti using proton beams, but no energy shift between Ti and TiN was observed. With heavier ions, ^{12}C, and ^{63}Cu, metallic Ti could be distinguished from TiO_2, but no difference between TiO_2 and TiN was observed. However, combining proton and heavy ion measurements, all three compositions can be identified.

The polycapillary lens was installed to detect low energy X-rays, and we were able to see X-rays down to O Kα (=0.525 keV). The X-ray intensity gain with the polycapillary lens was modest, a factor of three at highest. Thus, the main advantage of the polycapillary lens is the detection of low energy X-rays. For energies higher than 7 keV the polycapillary lens is actually starting to decrease the efficiency and should thus be uninstalled if this is the main region of interest.

I have also developed software for analyzing high-energy resolution data, which cannot be done with current commercial software such as GUPIX. This development has greatly reduced the time needed for analyzing the data produced by transition-edge sensors, and it can also be used by a person not familiar with the exact algorithms or working principles of the underlying code.

Transition-edge sensors in PIXE have been demonstrated to be very useful. The high-energy resolution, wide-energy range, and high efficiency is a combination that is sought after in every spectroscopy. All the good properties do not come without a disadvantage. Compared to the standard silicon drift detector, TES detectors are not commercially available and thus the number is very limited. The cost for such detector is much larger, and the operation of the detector requires much more expertise compared to solid state detectors. The spectrum analysis is often more complicated due to the details like multiple ionization satellite lines, that cannot be handled with commercial software.

In terms of other low-temperature detectors, there is some competition. For example detector like metallic magnetic calorimeter (MMC) [51] is a promising detector that can compete with TES. These detectors share many similarities and I see this as a positive competition that will surely benefit also TES.

Wavelength-dispersive X-ray detector (WDX) is another high-resolution detector commonly used in PIXE. In terms of pure energy-resolution WDX is superior to TES, and one could argue that by combining SDD to measure the whole spectrum, and WDX to measure the interesting area, this combination can do the same as TES or even outperform it. In some instances, this can very well be true, but not always. The simpler is better, and obtaining all the information from one spectrum instead of multiple spectra is beneficial. Sometimes you can also miss some information, if you don't expect to look for it with WDX. With the TES, you do not need any prior knowledge of the sample you are measuring. In the science in general, it is the unexpected that is many times the most interesting finding, and this is something you can achieve more easily with TES. Taking, for example, the analysis example in section 6.3, the most interesting finding (from an analyst point of view at least) was the amount of Ba in the sample, which we could not see at all from the SDD spectrum. Possibility to see unexpected things like this makes TES highly relevant for analyzing complicated samples.

In summary, PIXE-TES is a powerful analysis tool. It shines in the analysis of highly complicated samples, which was demonstrated by measuring samples like the NIST SRM 611, and fly ash from a power plant. It can also be used in chemical speciation in the same way like WDX can be, and TES array has high enough efficiency to do chemical speciation even in thin films.

REFERENCES

[1] M. Laitinen, M. Käyhkö, G. Hahn, N. von Uexküll-Güldenband, and T. Sajavaara. Tang dynasty (618–907) bowl measured with PIXE. *Nuclear Instruments and Methods in Physics Research Section B: Beam Interactions with Materials and Atoms* 406 (2017) 329–333.

[2] W. C. Röntgen. On a New Kind of Rays. *Science* 3.59 (1896) 227–231.

[3] *All Nobel Prizes in Physics*. URL: http://www.nobelprize.org/nobel_prizes/physics/laureates/.

[4] C. G. Barkla. Secondary Rontgen Rays and Atomic Weight. *Nature* 73.1894 (1906) 365.

[5] A. Hadding. Mineralienanalyse nach röntgenspektroskopischer Methode. *Zeitschrift für anorganische und allgemeine Chemie* 122.1 (1922) 195–200.

[6] T. B. Johansson, R. Akselsson, and S. A. E. Johansson. X-ray analysis: Elemental trace analysis at the 10^{-12} g level. *Nuclear Instruments and Methods* 84.1 (1970) 141–143.

[7] T. Calligaro, J. D. MacArthur, and J. Salomon. An improved experimental setup for the simultaneous PIXE analysis of heavy and light elements with a 3 MeV proton external beam. *Nuclear Instruments and Methods in Physics Research Section B: Beam Interactions with Materials and Atoms* 109-110 (1996) 125–128.

[8] B. Forslind, K. Malmqvist, and J. Pallon. Proton induced X-ray emission analysis of biological specimens - Past and future. *Scanning Microscopy* 5.3 (1991) 877–884.

[9] C. G. Ryan. Quantitative trace element imaging using PIXE and the nuclear microprobe. *International Journal of Imaging Systems and Technology* 11.4 (2001) 219–230.

[10] R. M. Harrison, D. J. T. Smith, and L. Luhana. Source Apportionment of Atmospheric Polycyclic Aromatic Hydrocarbons Collected from an Urban Location in Birmingham, U.K. *Environmental Science & Technology* 30.3 (1996) 825–832.

[11] K. G. M. Sven A. E. Johansson John L. Campbell. *Particle-Induced X-Ray Emission Spectrometry (PIXE)*. A Wiley-Interscience Publication, New York, 1995.

[12] G. V. Pavlinsky. *Fundamentals of X-Ray Physics*. Cambridge International Science Publishing, 2007.

[13] R. Jenkins, R. Manne, R. Robin, and C. Senemaud. IUPAC—nomenclature system for x-ray spectroscopy. *X-Ray Spectrometry* 20.3 (1991) 149–155.

[14] A. C. Thompson. *X-ray Data Booklet*. Lawrence Berkeley National Laboratory, University of California, 2009.

[15] B. L. Henke, E. M. Gullikson, and J. C. Davis. X-Ray Interactions: Photoabsorption, Scattering, Transmission, and Reflection at E = 50-30,000 eV, Z = 1-92. *Atomic Data and Nuclear Data Tables* 54.2 (1993) 181–342.

[16] C. A. MacDonald. Focusing Polycapillary Optics and Their Applications. *X-Ray Optics and Instrumentation* 867049 (2010).

[17] P. Sigmund. *Particle Penetration and Radiation Effects*. Springer, 2006.

[18] A. Kahoul, A. Abassi, B. Deghfel, and M. Nekkab. K-shell fluorescence yields for elements with $6 \leq Z \leq 99$. *Radiation Physics and Chemistry* 80.3 (2011) 369–377.

[19] D. D. Cohen. Average L shell fluorescence yields. *Nuclear Instruments and Methods in Physics Research Section B: Beam Interactions with Materials and Atoms* 22.1 (1987) 55–58.

[20] S. J. Cipolla. ISICS2008: An expanded version of ISICS for calculating K-, L-, and M-shell cross sections from PWBA and ECPSSR theory. *Computer Physics Communications* 180.9 (2009) 1716–1717.

[21] K. Ishii, S. Morita, and H. Tawara. Bremsstrahlung induced by proton and ^{3}He-ion bombardments in the 1-4-MeV/amu energy range. *Physical Review A* 13.1 (1976) 131–138.

[22] K. Ishii, M. Kamiya, K. Sera, S. Morita, and H. Tawara. Directional anisotropy of secondary-electron bremsstrahlung induced by proton bombardment of thin solid target. *Physical Review A* 15.5 (1977) 2126–2129.

[23] A. Anttila, R. Hänninen, and J. Räisänen. Proton-induced thick-target gamma-ray yields for the elemental analysis of the Z=3–9, 11–21 elements. *Journal of Radioanalytical Chemistry* 62.1-2 (1981) 293–306.

[24] J. I. Goldstein, D. E. Newbury, J. R. Michael, N. W. Ritchie, J. H. J. Scott, and D. C. Joy. *Scanning Electron Microscopy and X-Ray Microanalysis*. Springer, 2017.

[25] B. Beckhoff, B. Kanngieber, N. Langhoff, R. Wedell, and H. Wolff. *Handbook of Practical X-ray Fluorescence Analysis*. Springer, 2006.

[26] U. Tapper and J. Räisänen. Comparison of various ions for use in heavy ion induced X-ray emission. *Nuclear Instruments and Methods in Physics Research Section B: Beam Interactions with Materials and Atoms* 71.2 (1992) 214–220.

[27] A. Harjunmaa, T. Sajavaara, K. Arstila, K. Kukli, and J. Keinonen. Thin film nanolaminate analysis by simultaneous heavy ion recoil and X-ray spectrometry. *Nuclear Instruments and Methods in Physics Research Section B: Beam Interactions with Materials and Atoms* 219-220 (2004) 773–777.

[28] D. A. Wollman, K. D. Irwin, G. C. Hilton, L. L. Dulcie, D. E. Newbury, and J. M. Martinis. High-resolution, energy-dispersive microcalorimeter spectrometer for X-ray microanalysis. *Journal of Microscopy* 188.3 (1997) 196–223.

[29] R. Alberti, A. Bjeoumikhov, N. Grassi, C. Guazzoni, T. Klatka, A. Longoni, and A. Quattrone. Use of silicon drift detectors for the detection of medium-light elements in PIXE. *Nuclear Instruments and Methods in Physics Research Section B: Beam Interactions with Materials and Atoms* 266.10 (2008) 2296–2300.

[30] N. Grassi, C. Guazzoni, R. Alberti, T. Klatka, and A. Bjeoumikhov. External scanning micro-PIXE for the characterization of a polycapillary lens: Measurement of the collected X-ray intensity distribution. *Nuclear Instruments and Methods in Physics Research Section B: Beam Interactions with Materials and Atoms* 268.11–12 (2010) 1945–1948.

[31] J. M. Wagner. *X-Ray Photoelectron Spectroscopy*. Nova Science Publishers, Inc., 2010.

[32] J. A. van Bokhoven and C. Lamberti. *X-Ray Absorption and X-Ray Emission Spectroscopy : Theory and Applications*. John Wiley & Sons, incorporated, 2016.

[33] P. Richard, J. Bolger, D. K. Olsen, and C. F. Moore. Molecular structure effects of aluminum $K\beta$ x-ray spectra produced in proton and alpha particle excitation. *Physics Letters A* 41.3 (1972) 269–271.

[34] P. G. Burkhalter, A. R. Knudson, D. J. Nagel, and K. L. Dunning. Chemical Effects on Ion-Excited Aluminum *K* X-Ray Spectra. *Physical Review A* 6.6 (1972) 2093–2101.

[35] R. L. Watson, A. K. Leeper, B. I. Sonobe, T. Chiao, and F. E. Jenson. Effect of chemical environment on the intensities of $K\alpha$ x-ray satellites produced in heavy-ion collisions. *Physical Review A* 15.3 (1977) 914–925.

[36] J. McWherter, D. K. Olsen, H. H. Wolter, and C. F. Moore. Silicon and silicon dioxide *K* x-ray spectra from hydrogen, helium, and oxygen bombardment. *Physical Review A* 10.1 (1974) 200–208.

[37] V. P. Petukhov, I. Török, and M. Terasawa. High resolution PIXE instrumentation survey. Part III. *Nuclear Instruments and Methods in Physics Research Section B: Beam Interactions with Materials and Atoms* 109–110 (1996) 105–108.

[38] F. Folkmann. Chemical effects in Cr containing samples measured by the KβKα intensity ratio and the Kβ energy shift. *Nuclear Instruments and Methods in Physics Research Section B: Beam Interactions with Materials and Atoms* 109–110 (1996) 39–41.

[39] M. Uda, O. Benka, K. Fuwa, K. Maeda, and Y. Sasa. Chemical effects in PIXE spectra. *Nuclear Instruments and Methods in Physics Research Section B: Beam Interactions with Materials and Atoms* 22.1 (1987) 5–12.

[40] M. Petric and M. Kavčič. Chemical speciation via X-ray emission spectroscopy in the tender X-ray range. *Journal of Analytical Atomic Spectrometry* 31.2 (2016) 450–457.

[41] K. Jun. Chemical effects in the satellites of X-ray emission spectra. *Nuclear Instruments and Methods in Physics Research Section B: Beam Interactions with Materials and Atoms* 75.1–4 (1993) 3–8.

[42] S. Raman and C. R. Vane. Implications of heavy-ion-induced satellite X-ray emission I: Introduction. *Nuclear Instruments and Methods in Physics Research Section B: Beam Interactions with Materials and Atoms* 3.1–3 (1984) 71–77.

[43] B. Sulik, I. Kádár, S. Ricz, D. Varga, J. Végh, G. Hock, and D. Berényi. A simple theoretical approach to multiple ionization and its application for 5.1 and 5.5 MeV/u X^{q++} Ne collisions. *Nuclear Instruments and Methods in Physics Research Section B: Beam Interactions with Materials and Atoms* 28.4 (1987) 509–518.

[44] J. H. McGuire and P. Richard. Procedure for Computing Cross Sections for Single and Multiple Ionization of Atoms in the Binary-Encounter Approximation by the Impact of Heavy Charged Particles. *Physical Review A* 8.3 (1973) 1374–1384.

[45] J. A. Demarest and R. L. Watson. Ion-excited $K\alpha$ x-ray satellite spectra of Si, S, Cl, and Ar in the gas phase. *Physical Review A* 17.4 (1978) 1302–1313.

[46] A. Langenberg and R. L. Watson. Study of Mg $K\alpha$ x-ray multiplet structure observed in ion-atom collisions. *Physical Review A* 23.3 (1981) 1177–1187.

[47] C. R. Vane, L. D. Hulett Jr, S. Kahane, F. D. Mcdaniel, W. T. Milner, G. D. O'kelley, S. Raman, T. M. Rosseel, G. G. Slaughter, S. L. Varghese, and J. P. Young. Implications of heavy-ion-induced satellite X-ray emission III: Chemical effects in high-resolution sulfur $K\alpha$ X-ray spectra. *Nuclear Instruments and Methods in Physics Research Section B: Beam Interactions with Materials and Atoms* 3.1–3 (1984) 88–93.

[48] M. Tachibana, H. Adachi, T. Mukoyama, Y. Hibino, Y. Sasa, K. Fuwa, and M. Uda. Intensity analysis of F $K\alpha$ satellite spectra of NaF and KF. *Nuclear Instruments and Methods in Physics Research Section B: Beam Interactions with Materials and Atoms* 49.1–4 (1990) 15–18.

[49] F. Folkmann. High resolution ion induced X-ray spectroscopy for chemical state analysis. *Nuclear Instruments and Methods in Physics Research Section B: Beam Interactions with Materials and Atoms* 75.1 (1993) 9–13.

[50] U. Uda. Extended analysis of satellite structures in particle induced X-ray emission spectra using molecular orbital calculations. *Advances in Quantum Chemistry* 37 (2000) 31–55.

[51] C. Enss. *Cryogenic Particle Detection*. Springer, 2005.

[52] M. A. Lindeman. "Microcalorimetry and the transition-edge sensor". PhD thesis. University of California at Davis, 2000.

[53] T. Pantazis, J. Pantazis, A. Huber, and R. Redus. The historical development of the thermoelectrically cooled X-ray detector and its impact on the portable and hand-held XRF industries. *X-Ray Spectrometry* 39.2 (2010) 90–97.

[54] C. Pascual-Izarra, N. P. Barradas, and M. A. Reis. LibCPIXE: A PIXE simulation open-source library for multilayered samples. *Nuclear Instruments and Methods in Physics Research Section B: Beam Interactions with Materials and Atoms* 249.1 (2006) 820–822.

[55] N. Wiener. Extrapolation, Interpolation, and Smoothing of Stationary Time Series. *New York: Wiley* (1949).

[56] B. K. Alpert, R. D. Horansky, D. A. Bennett, W. B. Doriese, J. W. Fowler, A. S. Hoover, M. W. Rabin, and J. N. Ullom. Filters for High Rate Pulse Processing. *arXiv:1212.1738* (2012).

[57] J. L. Campbell, N. I. Boyd, N. Grassi, P. Bonnick, and J. A. Maxwell. The Guelph PIXE software package IV. *Nuclear Instruments and Methods in Physics Research Section B: Beam Interactions with Materials and Atoms* 268.20 (2010) 3356–3363.

[58] P. J. Statham. Quantifying Benefits of Resolution and Count Rate in EDX Microanalysis. In: *X-Ray Spectrometry in Electron Beam Instruments*. Ed. by D. B. Williams, J. I. Goldstein, and D. E. Newbury. Springer US, 1995 101–126.

[59] C. Mendoza, Z. Gonzalez, E. Gordo, B. Ferrari, and Y. Castro. Protective nature of nano-TiN coatings shaped by EPD on Ti substrates. *Journal of the European Ceramic Society* 38.2 (2018) 495–500.

[60] M. A. Reis, L. C. Alves, N. P. Barradas, P. C. Chaves, B. Nunes, A. Taborda, K. P. Surendran, A. Wu, P. M. Vilarinho, and E. Alves. High Resolution and Differential PIXE combined with RBS, EBS and AFM analysis of magnesium titanate (MgTiO3) multilayer structures. *Nuclear Instruments and Methods in Physics Research Section B: Beam Interactions with Materials and Atoms* 268.11–12 (2010) 1980–1985.

[61] M. R. J. Palosaari, K. M. Kinnunen, J. Julin, M. Laitinen, M. Napari, T. Sajavaara, W. B. Doriese, J. Fowler, C. Reintsema, D. Swetz, D. Schmidt, J. Ullom, and I. J. Maasilta. Transition-Edge Sensors for Particle Induced X-ray Emission Measurements. *Journal of Low Temperature Physics* 176.3-4 (2013) 285–290.

[62] L. Mandić, S. Fazinić, and M. Jakšić. Chemical effects on the $K\beta''$ and $K\beta_{2,5}$ x-ray lines of titanium and its compounds. *Physical Review A* 80.4 (2009) 042519.

[63] M. Kavcic, A. G. Karydas, and C. Zarkadas. Chemical state analysis employing sub-natural linewidth resolution PIXE measurements of Kα diagram lines. *X-Ray Spectrometry* 34.4 (2005) 310–314.

[64] M. Käyhkö, M. R. J. Palosaari, M. Laitinen, K. Arstila, I. J. Maasilta, J. W. Fowler, W. B. Doriese, J. N. Ullom, and T. Sajavaara. Minimum detection limits and applications of proton and helium induced X-ray emission using transition-edge sensor array. *Nuclear Instruments and Methods in Physics Research Section B: Beam Interactions with Materials and Atoms* 406 (2017) 130–134.

[65] J. F. Ziegler, M. D. Ziegler, and J. P. Biersack. SRIM – The stopping and range of ions in matter (2010). *Nuclear Instruments and Methods in Physics Research Section B: Beam Interactions with Materials and Atoms* 268.11–12 (2010) 1818–1823.

[66] V. Horvat, R. L. Watson, and Y. Peng. Systematics of *K*α x-ray satellite structure. *Physical Review A* 74.2 (2006) 022718.

ORIGINAL PAPERS

PI

BROADBAND ULTRAHIGH-RESOLUTION SPECTROSCOPY OF PARTICLE-INDUCED X RAYS: EXTENDING THE LIMITS OF NONDESTRUCTIVE ANALYSIS

by

M. R. J. Palosaari, M. Käyhkö, K. M. Kinnunen, M. Laitinen, J. Julin, J. Malm, T. Sajavaara, W. B. Doriese, J. Fowler, C. Reintsema, D. Swetz, D. Schmidt, J. N. Ullom, and I. J. Maasilta

Physical review applied - 6, 024002 (2016)

Broadband Ultrahigh-Resolution Spectroscopy of Particle-Induced X Rays: Extending the Limits of Nondestructive Analysis

M. R. J. Palosaari,[1] M. Käyhkö,[2] K. M. Kinnunen,[1] M. Laitinen,[2] J. Julin,[2] J. Malm,[1,2] T. Sajavaara,[2] W. B. Doriese,[3] J. Fowler,[3] C. Reintsema,[3] D. Swetz,[3] D. Schmidt,[3] J. N. Ullom,[3] and I. J. Maasilta[1,*]

[1]*Nanoscience Center, Department of Physics, University of Jyvaskyla, P.O. Box 35, FI-40014 Jyvaskyla, Finland*

[2]*Accelerator Laboratory, Department of Physics, University of Jyvaskyla, P.O. Box 35, FI-40014 Jyvaskyla, Finland*

[3]*National Institute of Standards and Technology, Boulder, Colorado 80305, USA*

(Received 25 August 2015; revised manuscript received 24 March 2016; published 4 August 2016)

Nondestructive analysis (NDA) based on x-ray emission is widely used, for example, in the semiconductor and concrete industries. Here, we demonstrate significant quantitative and qualitative improvements in broadband x-ray NDA by combining particle-induced emission with detection based on superconducting microcalorimeter arrays. We show that the technique offers great promise in the elemental analysis of thin-film and bulk samples, especially in the difficult cases where tens of different elements with nearly overlapping emission lines have to be identified down to trace concentrations. We demonstrate the efficiency and resolving capabilities by spectroscopy of several complex multielement samples in the energy range 1–10 keV, some of which have a trace amount of impurities not detectable with standard silicon drift detectors. The ability to distinguish the chemical environment of an element is also demonstrated by measuring the intensity differences and chemical shifts of the characteristics x-ray peaks of titanium compounds. In particular, we report measurements of the $K\alpha/K\beta$ intensity ratio of thin films of TiN and measurements of Ti $K\alpha$ satellite peak intensities in various Ti thin-film compounds. We also assess the detection limits of the technique, comment on detection limits possible in the future, and discuss possible applications.

DOI: 10.1103/PhysRevApplied.6.024002

I. INTRODUCTION

X-ray emission spectroscopy is a ubiquitous technique to study the elemental composition of materials. Different versions of the technique exist, varying either in the type of excitation used to generate the characteristic x rays or in the method of detecting them. Typically, high-energy electrons, ions, or x rays are used for excitation, with detectors operating in either the energy-dispersive (EDS) or the wavelength-dispersive (WDS) mode. The choice of the excitation source depends on many factors, with electron-beam and x-ray sources being most common. Here, we focus on ion-beam excitation, or the so-called particle-induced x-ray emission (PIXE) technique, most often performed with 2–3-MeV protons, because they give the best x-ray yield for elements between $Z = 20$ and 40 [1].

There are several reasons to use particle excitation. Compared to electron-beam excitation, there are at least the following advantages: (i) The accelerated particle beam in PIXE can be taken out of the vacuum to study large or delicate samples (artifacts, biological samples, etc.), (ii) particle beams penetrate much deeper into the sample and can be used to study the subsurface composition, whereas electron beams give information only from the surface, and, most importantly, (iii) due to the orders-of-magnitude-heavier mass of the proton, the background brehmsstrahlung, which in many cases limits sensitivity, is much reduced. Compared to conventional x-ray-induced fluorescence, PIXE (i) does not suffer from the presence of characteristic peaks of the x-ray tube anode material and (ii) gives more sensitivity for thin samples and elements $Z > 20$ due to a lower background in the high-energy range [2].

In any spectroscopic experiment, the ability to detect energy differences as small as possible is always sought after, so that close-lying emission lines in complex samples can be resolved. In addition, in x-ray emission measurements the energy resolution of the detector often sets the limit on the impurity levels that can be measured, as the signal-to-background ratio improves with narrower lines. The most commonly used detector in PIXE measurements is the silicon drift detector (SDD), which is energy dispersive and fairly cheap, offers high count rates, up to 100 kcps without resolution degradation, and has a wide dynamic energy range. However, even the optimal energy resolution of the SDD (typically around 130 eV at 6 keV) is quite poor and limits the detection of elements with overlapping excitations and low impurity levels. On the

*maasilta@jyu.fi

other hand, wavelength-dispersive detectors have excellent energy resolution (around 1 eV at 6 keV) [3], but their limited energy range and small solid angle limit their use to experiments where either only a small range in energy is of interest or where high-excitation beam currents and long measurement times are possible.

Here, we apply a detector instrument to PIXE that combines the advantages of the wide energy range, high efficiency, and simplicity of the energy-dispersive detection with ultrahigh-energy resolution and high sensitivity, by using arrays of superconducting transition-edge sensor (TES) x-ray microcalorimeters operated at 0.1 K [4,5]. Although TES sensors have been used before in materials analysis, often their applicability in real-life problems is compromised by their inherently low count-rate capability. However, we obtain competitive counting rates (approximately kcps) and collecting areas by using large arrays with hundreds of individual detector elements. This count-rate capability is combined with a full width at half maximum (FWHM) energy resolution demonstrated to be 3 eV at 6 keV in the best cases [6]. Thus, we have a unique instrument for elemental analysis that combines the best aspects of traditional EDS and WDS instruments. Similar TES arrays have recently also been used in tabletop x-ray absorption spectroscopy experiments [7] and in synchrotron-based x-ray spectroscopy [8].

In this study, we report the wide energy range, ultrahigh-resolution PIXE elemental-analysis results on several kinds of thin-film and bulk samples. In addition to identifying correctly elements from standard samples containing over 60 different trace elements, we also present several results on thin-film Ti compounds of Ti, TiO_2, and TiN. We measure the chemical shifts of the positions of the Ti $K\alpha$ and $K\beta$ peaks in atomic-layer-deposited TiO_2 while collecting data in the full energy range 1–10 keV, determine the changes in the $K\alpha/K\beta$ intensity ratios among the different films with high precision, and observe multiple-ionization satellite emission of the Ti $K\alpha$ transition. We also study ppm-level impurity contents of several common Co- and Pb-containing pigment materials, discovering low-level impurities, unresolvable with the standard SDD detector, that may be used to fingerprint the material source. A discussion on possible future detection limits and applications is also presented.

II. SUPERCONDUCTING DETECTOR TECHNOLOGY

The maturation of low-temperature detector technology enables their use in many experiments ranging in frequency from terahertz bolometry [9] to γ-ray detection [10]. The detector type used here, a TES microcalorimeter, is an energy-dispersive detector that is based on the sharp resistive transition between the normal state and the superconducting state of a thin film [11]. When a photon hits an absorber material that is coupled to the superconducting thin film, the temperature of the film first quickly rises and then falls back to the steady state with a time constant τ set by the heat capacity C and thermal conductance G and the reduction in Joule heating associated with the increase in resistance, causing a pulse-shaped change in the resistance of the device. This resistance change causes a pulse in the current, which is read out with a superconducting quantum interference device (SQUID) [11]. SQUIDs are well suited for reading out TESs thanks to their low noise, low power dissipation, and low input impedance [12,13]. TES devices optimized for x-ray detection are relatively slow (effective time constants around 0.1–1 ms), which limits their count rate to 100–1000 cps, but they have high-energy resolution when operated at temperatures around 0.1 K (in the best cases, below 2 eV at 6 keV [14]). However, with an array of hundreds of TES detectors, the total count rate can be beyond kcps [10]. Another advantage of the array format is that the active detector area, and thus the collection efficiency, is increased to keep the irradiation times shorter, so that the possible damage to delicate samples in a PIXE measurement can be limited. The major motivation for using TES detectors is their exceptionally good energy resolution for energy-dispersive detectors. In addition, within the designed operational energy range of a particular TES detector, the energy resolution is not degraded as a function of energy [5], in contrast to SDD detectors, where it scales as $\sqrt{E}$.

The energy-resolution limit is typically dominated by the unavoidable thermodynamic fluctuations of energy between the sensor and the heat bath, leading to an expression for the theoretical FWHM energy resolution $\Delta E = 5.6\sqrt{k_B T^2 C/\alpha}$, where k_B is the Boltzmann constant, T is the temperature of the sensor, C is its heat capacity, and $\alpha = (T/R)\partial R/\partial T$ is the dimensionless parameter describing the steepness of the superconducting transition [5]. The above result is valid for sensors with $G \sim T^3$, in the optimal case of $\alpha \gg 1$, without excess noise sources and in the limit $T \gg T_{\mathrm{bath}}$ and $\beta \ll 1$, where T_{bath} is the temperature of the refrigerating stage (the sensor temperature is always higher due to Joule heating), and $\beta = (I/R)\partial R/\partial I$ with I the current. In addition, optimal filtering and a constant pulse shape are assumed. We see that lowering the operational temperature is the best way to reduce ΔE. The practical limits of refrigeration technology (adiabatic demagnetization and He dilution refrigeration) often set the lower limit to around $T \sim 0.1$ K. It then seems that, by decreasing C and increasing α, even lower values could be obtained. However, these parameters are hard to change, because the ratio C/α also sets the upper limit in energy where the sensors can be operated without saturation [15]. Thus, for x-ray calorimetry up to the 10-keV range, any significant advances of resolution below 1–2 eV are not straightforward with TES sensors.

Pioneering work on using single-pixel x-ray TES microcalorimeters in electron-beam-induced x-ray spectroscopy

of materials was performed at NIST Boulder at the turn of the millennium [16,17], with the result that an electron microprobe analysis with a small array of TES sensors is now commercially available, with an energy resolution below 10 eV at 1.7 keV [18]. In Ref. [17], it is reported that the single-pixel TES-based electron microprobe spectrometer operating up to 10 keV has a FWHM resolution of 4.5 eV at 5.9 keV, with high efficiency and a maximum count rate of approximately 1000 cps. In addition, a single-pixel TES sensor is tested with PIXE, as well [19], but only with a far-from-optimal energy resolution around 18 eV at 1.7 keV and a count rate of approximately 50 cps. Our instrument achieves almost an order-of-magnitude improvement in energy resolution, and over an order of magnitude in count rate, making it a truly practical PIXE spectrometer.

III. EXPERIMENTS

A. Detector setup

The 160-pixel TES array and the time division multiplexed SQUID readout [13] used in the experiments are fabricated at NIST Boulder. A single TES pixel consists of an about 300-nm-thick superconducting Mo/Cu bilayer with a critical temperature T_C around 100 mK. The 500-nm-thick normal-metal Cu strips are deposited on top of the bilayer to suppress local T_C variation at the edges [20] and to suppress noise [21]. The absorber, coupled directly to the superconducting film, is a $350 \times 350 \times 2.5\ \mu m^3$ bismuth block. Bi is used because of its advantageous combination of high x-ray absorption and low heat capacity. A collimator chip with a 320 μm $\times$ 305 μm aperture size for each pixel sits on top of the array chip to prevent x-ray hits outside the absorber area.

The experiments presented in this paper are performed with a total of 30–60 pixels, a 65-mK bath temperature, and a 2.01-MeV proton beam striking the samples in vacuum. A pulse-tube precooled cryogen-free adiabatic demagnetization refrigerator [22] is used to cool the detectors and the readout, which are located inside a specially designed extension structure [6] to facilitate close proximity to the samples (Fig. 1). The sample and the detector vacuums are separated by an AP3.3 ultrathin polymer/Al silicon grid x-ray window from Moxtek Inc., allowing efficient x-ray transmission above 1-keV energies. In addition, to stop backscattered protons from hitting the detector setup, an additional 125-μm-thick Be foil is placed in front of the vacuum window. The extension is positioned at a 90° angle with respect to the proton-beam axis, and the sample surface is tilted 45° with respect to it. Thin infrared filters fabricated in house (280-nm SiN membrane supporting a 225-nm Al film) are used at the three shielding stages (60 K, 3 K, and 50 mK) of the extension, to reduce unwanted power loading on the detectors. Further details of the measurement geometry and the setup can be found in Ref. [6], where the FWHM energy resolution 3.06 eV of the best pixel in our setup is also reported. In contrast to Ref. [6], however, the distance between the detector and the samples is reduced from 30 to 15 cm, increasing the collection efficiency by a factor of 4. An Amptek X-123SDD silicon drift detector is used as a reference detector, with measurements performed in air.

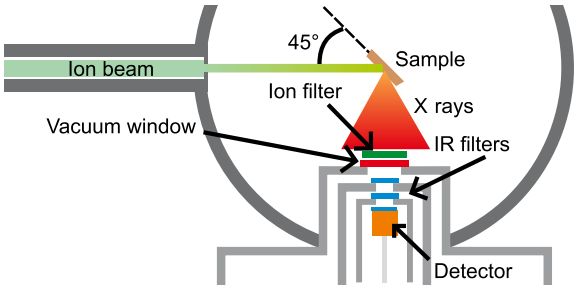

FIG. 1. A schematic of the detector setup. The sample and the detector vacuums are separated by an x-ray vacuum window, with an additional Be foil as an ion filter in front of the vacuum window. Thin SiN/Al infrared filters are used at the three shielding stages (60 K, 3 K, and 50 mK) of the extension.

B. Reference samples and efficiency calibration of the TES array

To demonstrate the capabilities of TES PIXE, two NIST standard reference material (SRM) samples with known compositions, a SRM 1157 stainless-steel sample (Fig. 2) and a SRM 611 glass sample (Fig. 3), are measured both with the TES-PIXE setup and with the SDD detector. SRM 1157 has 12 minor elements in addition to Fe: C, Si, P, S, Mo, V, Cr, Mn, Ni, Cu, W, and Co, with concentrations ranging from 40 ppm to 6%, whereas SRM 611 has altogether 61 trace elements in a glass support matrix with concentrations ranging from 100 to 500 ppm. The glass matrix has a nominal composition of 72% SiO_2, 14% Na_2O, 12% CaO, and 2% Al_2O_3. The average count rate for a single TES pixel is 9.3 cps, leading to a total count rate of about 550 cps for 60 pixels. The SDD count rate is 1400 cps. The measurement times (4 h for TES and 1.13 h for SDD) are chosen such that the total number of counts is approximately the same. For the TES detector, the conversion from pulse height to energy is achieved by a spline interpolation of the known peak energies, for each pixel separately due to the intrinsic nonlinearity of the TES detector. In the full energy range of 1–10 keV, the typical observed pulse height nonlinearity is $(25 \pm 0.3)\%$ at 10 keV compared to a line fitted at the lower energy range. The error gives the variation from cooldown to cooldown. Before a measurement of an unknown sample, the energy calibration is always checked with a dedicated calibration sample, consisting of a thin-film multilayer of Ge, Cu, Cr, and Ti on a Si substrate. The $K\alpha$ and $K\beta$ lines of those elements cover the energy range 1–11 keV. The drift

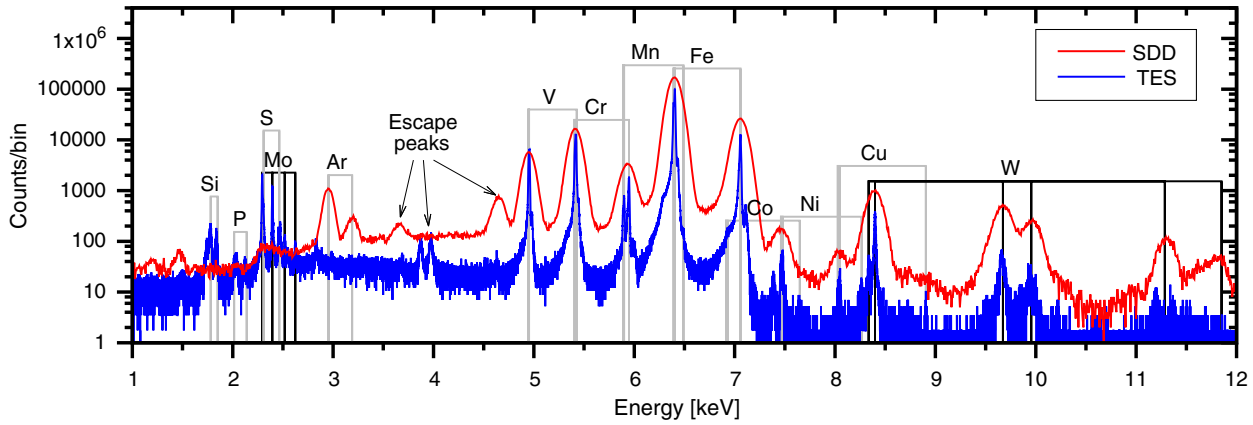

FIG. 2. SRM 1157 reference sample measured with both TES (blue line) and SDD (red line) detectors. The bin width for TES is 0.5 eV, and for SDD it is 7 eV. The Ar excitations from air can be seen in the SDD data around 3 keV as well as the Si escape peak from the Fe x rays at 4.6 keV and from the Cr at 3.7 keV. In the TES data, the Bi escape peaks can be seen just below 4 keV.

occurring during the measurement is corrected to the first order [23].

We can see from Figs. 2 and 3 the clear difference in the energy resolution between the SDD and the TES setup. Focusing on the steel sample first (Fig. 2), we observe that, with the TES detector, we can identify all elements in the sample except carbon (its emission below 1 keV is cut by filtering in the setup). In particular, low levels of Co (280 ppm) can be seen, even though its $K\alpha$ lines are close to the dominant Fe $K\beta$ line at 7 keV. Moreover, phosphorus and sulphur lines are also observable above 2 keV, even though the concentrations are low—110 and 40 ppm, respectively. None of those elements (Co, P, and S) could be identified with the SDD detector. For the more complex sample SRM 611, some of the dense peaks in the energy range 4–8 keV overlap in the SDD data, making the identification of most elements impossible or extremely challenging with SDD detectors, particularly the heavier rare-earth elements (Ce, Nd, Sm, Gd, Tb, and Dy) whose $L\alpha$ lines are mixed in with the $K\alpha$ lines of the lighter transition metals (Sc, Ti, V, Cr, Mn, Fe, Co, and Ni). In contrast, with the TES detectors, we identify most of the elements (38) that emit x rays in the energy range shown, without any complex peak-fitting analysis. By looking at the observed good peak-to-background ratios of the SRM 611 trace-element peaks measured with the TES detectors, we estimate that roughly over an order-of-magnitude-lower level impurities at the 10–50-ppm level could have been detected with the same measurement time. As a final note on the SRM 611 spectrum and to put it into perspective, an electron probe analysis with a commercial liquid-nitrogen-cooled semiconductor detector could not identify any of the trace elements.

For the highest count-rate peaks (e.g., Fe in Fig. 2), there is evidence of asymmetric low-energy tailing, which we know originates from the nonidealities of the Bi absorber.

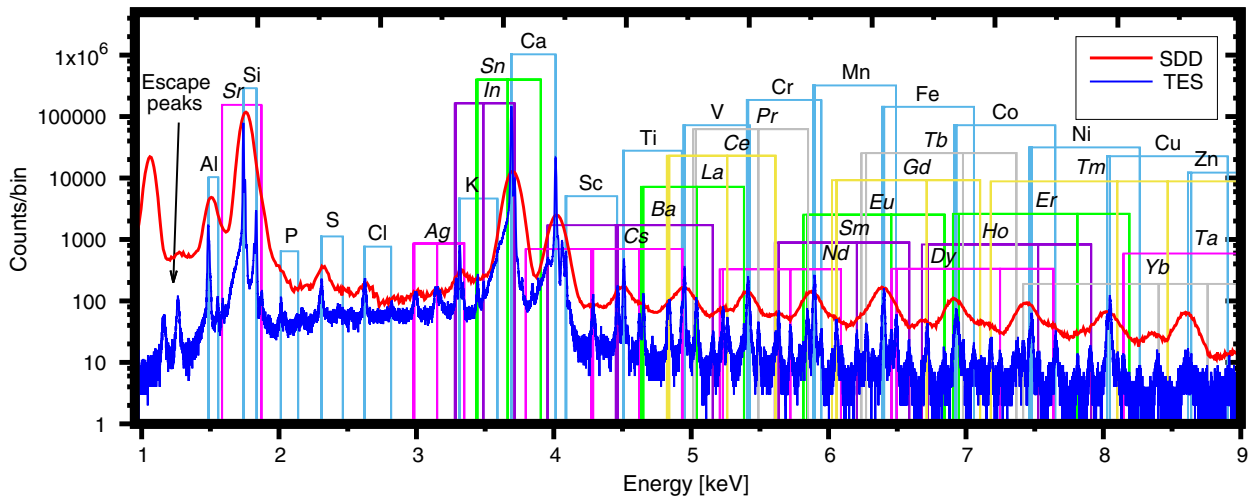

FIG. 3. SRM 611 reference sample measured with both TES (blue line) and SDD (red line) detectors. The bin width for TES is 0.5 eV, and for SDD it is 7 eV. The Ar excitations from air can be seen in the SDD data, as well as the Si escape peak from the Ca x rays at 2 keV.

One possibility is that there are long-lived metastable states in Bi that can trap a small part of the heat pulse long enough so that it does not contribute to the measured response. More work is required to clarify this effect.

To be able to discern quantitative information on samples with unknown elemental concentrations, an efficiency calibration of the detector is required. To determine the detector efficiency, the measured data of the SRM samples are analyzed using the GUPIXwin program [24], which calculates the elemental concentrations based on the known physical parameters of the setup. In the GUPIXwin analysis, all the external filters are taken into account, but the to-be-determined detector setup efficiency is temporarily set to 1. For the SRM 611 sample, the nominal matrix mass composition (72% SiO_2, 14% Na_2O, 12% CaO, and 2% Al_2O_3) is used in the GUPIXwin analysis, whereas for SRM 1157 sample, the matrix composition (consisting mostly of iron) is iterated by GUPIXwin. We do not use the standard fitting procedures of the program; instead, the peak areas are integrated after the continuous background is removed by a visual fit. Then, the concentrations (without the efficiency of the setup) are calculated using the x-ray yields that GUPIXwin calculates. Finally, the detector setup efficiency is calculated as the ratio between the measured concentration without the detector efficiency and the known reference concentration, for all reference energies. In the analysis, statistical uncertainties and uncertainties in the ionization cross sections for K lines (1%–7%) [25] and L lines (5%) [26] are taken into account. The reference values for the concentrations and energies of the analyzed elements are taken from Ref. [27] (preferred average values, Table 8) for SRM 611 and from the NIST certificate for the SRM 1157 sample.

Figure 4 shows the measured efficiency data (dots), compared with the theoretical efficiency curve consisting of the transmission through the 125-μm Be filter used to stop the scattered ions, through the AP3.3 vacuum window, through the 280-nm-thick Si_3N_4 membrane with a 220-nm Al coating used as infrared filters at the three stages of the cryostat, and the absorption of the 2.5-μm Bi absorber (using Ref. [28]). We see that the experimental values agree well with the theory and conclude that, within the accuracy of the measurement and the reference data, the calculated theoretical curve can be used to represent the efficiency of the setup. We note that the SRM 1157 points are derived from elements with high concentrations, leading to low uncertainties and very good agreement with the theory. In contrast, some of the SRM 611 points have more scatter. This is natural, as many of the trace-element concentrations of that sample are not so accurately known and are uncertified. In addition, we note that three observed elements (Al, Cu, and Mn) are excluded from the analysis because of extra fluorescence coming from the sample stage and other parts of the apparatus. It should also be noted that the theoretical efficiency of the vacuum window never reaches a level higher than 77% below 10-keV energies. This is due to the fact that a thick silicon grid with a 77% hole area is under the polymer in the AP3.3 vacuum window.

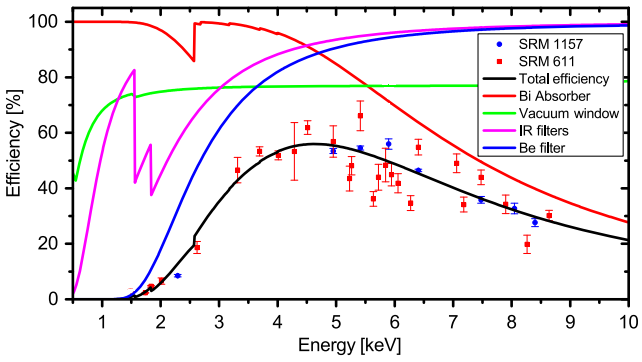

FIG. 4. The measured (squares and circles) and simulated (black line) total efficiency of the TES-PIXE setup. Also plotted are the absorption of the Bi absorber (red line) and the transmissions of the AP3.3 vacuum window (green line), infrared filters (pink line), and the Be filter (blue line). The efficiency curve is calibrated using the known reference materials NIST SRM 611 (squares) and NIST SRM 1157 (circles).

C. Chemical shifts, intensity ratios, and satellite peaks in Ti-based samples

Because of the excellent energy resolution of TES detectors, we expect that even chemical effects, where the characteristic x rays of a material are dependent on the chemical environment of a element, can be observed in our setup. The chemical state of an element (oxidation number and chemical bonding) influences its electronic transitions and atomic-energy levels, even those involving the inner shells of the atoms. Different kinds of effects are observed that affect x-ray transitions: energy shifts of the characteristic x-ray lines, the alteration of x-ray relative intensity ratios and line shapes, and satellite peak formation [29]. Typically, these kinds of shifts can be resolved only with a wavelength-dispersive and not with an energy-dispersive detector; see, for example, Ref. [30]. With TES detectors in the electron-probe analysis setup, evidence for Fe L-shell transition chemical shifts has been seen before [17].

We measure the x-ray spectra of three different titanium-based thin-film samples—Ti (400 nm), TiN (500 nm), and TiO_2 (450 nm)—all on Si substrates, with TES PIXE, using 2-MeV proton excitation. The TiN and TiO_2 are grown with atomic-layer deposition, and the Ti film is electron-beam evaporated. The samples are measured in the order Ti, TiN, Ti, TiO_2, and Ti, so that any possibility of jumps in the calibration is ruled out by comparing the Ti spectra. Any possible energy drift of a pixel is corrected on the Si $K\alpha$ line, which is common in all of the samples and close enough in energy to Ti so that the error introduced by the gain nonlinearity is insignificant. Each sample is measured

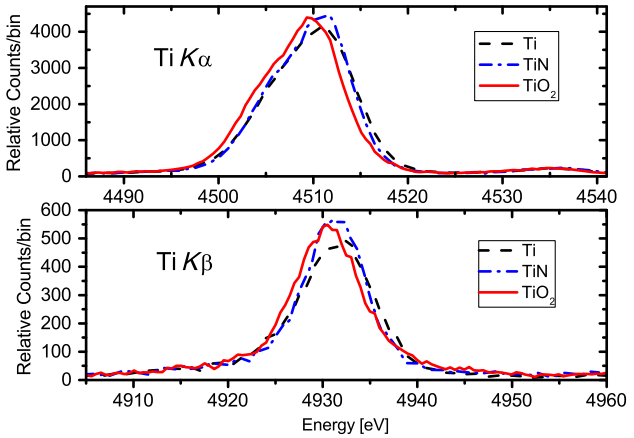

FIG. 5. Ti peaks from the three different Ti compounds normalized for the $K\alpha$ peak area. The spectra are divided into two plots for clarity. Top: The Ti $K\alpha_{1,2}$, bottom: The Ti $K\beta_{1,3}$. A chemical shift for the TiO_2 sample is visible.

for 1 h with an average count rate of about 8 cps per pixel. The energy calibration of the spectra is done on the Ti sample, using the $K\alpha$ and $K\beta$ peaks of Si and Ti.

Figure 5 shows the measured Ti $K\alpha$ and $K\beta$ complexes from all three samples. A negative chemical shift of 1.1 eV is seen on the $K\alpha$ complex of the TiO_2 sample compared to the pure Ti sample. Also, a slightly smaller shift of 1.0 eV can be seen in the $K\beta$. No measurable shift can be seen in the TiN spectrum. The shift is determined by fitting Gaussians to the peaks and taking the difference between the peak centroids of the Ti and TiO_2 lines. The standard deviation of the peak position for all the lines is 0.3 eV (24 pixels in this measurement), which is well below the observed shift value, giving us confidence on the statistical significance of the result. Moreover, all the shifts have the same negative sign, strong evidence against a random process. In addition, this chemical shift result agrees with x-ray photoelectron spectroscopy measurements [31] and wavelength-dispersive spectrometer measurements [32]. Note that, due to the peak-fitting procedure, chemical shifts much below the FWHM energy resolution of the instrument are observable. The observed $K\beta/K\alpha$ intensity ratios are $(12.5 \pm 0.1)\%$ for Ti, $(13.1 \pm 0.2)\%$ for TiN, and $(13.3 \pm 0.2)\%$ for TiO_2. This trend of an increasing $K\beta/K\alpha$ ratio is consistent with previous studies of Ti and TiO_2 [33–35], as the $K\beta/K\alpha$ ratios are shown to depend on the chemical state of 3d elements [36]. No literature results for TiN are found. From the above results, we conclude that the accurate measurement of the $K\beta/K\alpha$ intensity ratio is a very useful way to obtain chemical information, as all studied Ti compounds show different values. This is in contrast to the shift in the line position, where only TiO_2 shows a measurable effect. Moreover, the measurement of peak ratios is less prone to systematic errors and is not sensitive to energy calibration issues. Note that, in addition to sensitivity to different compounds, one can, in principle, also distinguish between different oxidation states of Ti in the same compound, i.e., the different oxides (TiO, TiO_2, and Ti_2O_3).

On the high-energy side of the main peaks (e.g., at 4.535 keV), the spectra show also smaller satellite lines, typical in PIXE measurements. The $K\alpha$ satellite intensity compared to the total Ti emission is $(4.9 \pm 0.1)\%$ for Ti, $(5.0 \pm 0.1)\%$ for TiN, and $(4.8 \pm 0.1)\%$ for TiO_2. This satellite peak is most likely generated during the ion bombardment when $1s$ and $2p$ vacancies are created simultaneously (multiple ionization). The $2p$ vacancy has a longer lifetime than the $1s$ vacancy. When the inner $1s$ vacancy deexcites in the presence of this spectator hole, there is a change in the electrostatic potential, leading to shifts in the energy levels and thus changing the energy of the emitted photon [37]. Although multiple-ionization Ti $K\alpha$ satellite peaks have been observed before with ion-beam excitation [38,39], we are not aware of any previous measurements on Ti thin-film samples or comparisons between different chemical compounds of Ti. As seen from the satellite intensity values, we do not observe any significant chemical sensitivity with the proton-beam excitation. However, literature reports suggest that with heavier projectiles chemical information can be obtained in some cases from the satellite intensities [40,41].

D. Pigment measurements

Finally, we also present elemental-analysis data from several pigment samples with unknown impurity content. Pigment analysis is useful in the context of art history, as major-element and trace-impurity content in pigments can pinpoint or rule out certain geographical locations and time periods [42]. As a first example, we show spectra from a cobalt blue ($CoAl_2O_4$) pigment sample (pellet compressed from powder), measured using both the TES and SDD detectors (Fig. 6) and a 2-MeV proton beam. The spectra

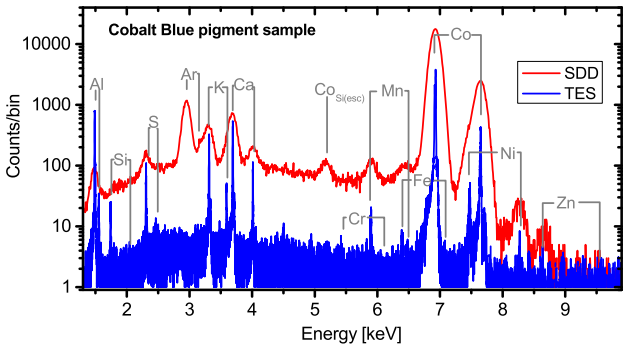

FIG. 6. PIXE spectra of a Co pigment sample using the SDD (red line) and TES (blue line) detectors. The bin width for TES is 0.5 eV and for the SDD 7 eV. Cr and Fe trace impurities can be resolved with the TES detectors.

are collected with a measurement time of 50 (TES) and 10 min (SDD). Many trace impurities can be identified: S, K, Ca, Cr, Mn, Fe, Ni, and Zn. Out of those impurities, Fe and Cr are observable only in the TES spectrum and cannot be identified from the SDD spectrum. The estimate for the Fe concentration is 920 ± 140 ppm and for the Cr 110 ± 40 ppm, calculated with the efficiency curve obtained previously. The TES spectrum shows also weak Si lines, but they may originate from secondary fluorescence of the vacuum window and/or IR filters.

Two different lead pigments, red lead (Pb_3O_4) and lead white [$2PbCO_2 \cdot Pb(OH)_2$], are also measured in addition to a reference sample of a bulk piece of industrial-grade metallic lead sheet (Fig. 7). The measurement time is 50 min for all samples with the TES detectors and below 10 min for the SDD. Both M- and L-shell Pb transitions are observable at the low and high end of the spectra, respectively. All three samples have clearly different compositions of trace impurities, again many of them identified only with the help of the TES detectors. Interestingly, all samples have traces of gold in the range 1000–2000 ppm. There are also visible peaks from copper in all samples, but we determine that most of the Cu contribution comes from the sample stage, so the possible sample contributions are unknown. The Pb red pigment is otherwise surprisingly clean. On the other hand, both the bulk Pb and the Pb white samples have many additional common impurities: Ba, Ca, Ti, Fe, and Ni, at concentrations 100–9000 ppm. The bulk sample has, in addition, Cr at the 1600-ppm level. Further studies will reveal if all Pb white samples contain these impurities or not, and whether some of them could serve as a fingerprint. Barium seems especially interesting, as the Pb red sample does not contain any within the detection limits, whereas the Pb white contains it at the 8500-ppm level, but the bulk lead only at the 800-ppm level.

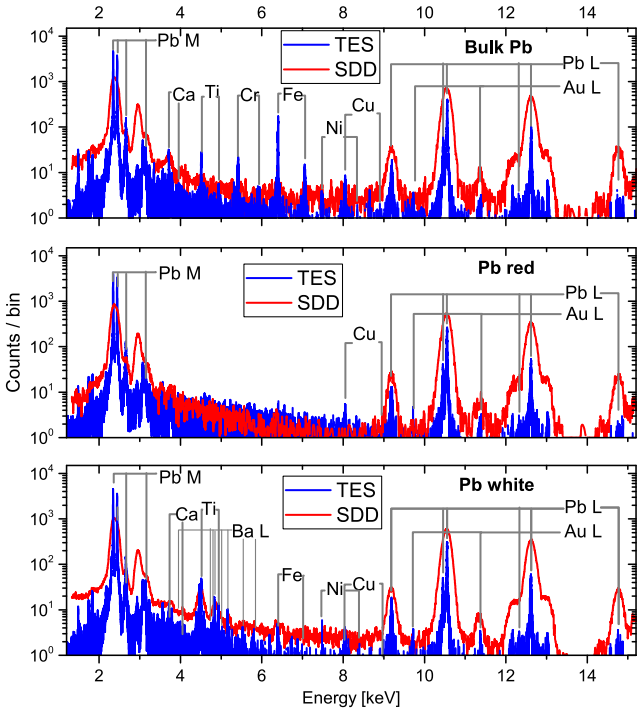

FIG. 7. PIXE spectra of three different Pb samples: bulk Pb (top), Pb red pigment (middle), and Pb white pigment (bottom), measured with both the SDD (red line) and TES (blue line) detectors. The bin width for TES is 0.5 eV and for the SDD 7 eV.

E. Analysis of detection limits

In all the presented spectra, it is clear that PIXE, in general, is well suited for trace-element analysis due to its low background level and that TES PIXE has more sensitivity than standard PIXE using SDD detectors. The detection limits are ultimately determined by Poisson statistics of the random count arrival times. Following Ziebold [17,43], the minimum mass fraction detectability limit at the 95% confidence level, C_{MMF}, for trace elements and without peak interference can be estimated from

$$C_{\mathrm{MMF}} = 3.29a/\sqrt{\tau P(P/B)}, \tag{1}$$

where a is an element and matrix-dependent unitless constant of the order of 1 [43], τ is the measurement time, P is the count rate of the peak in question, and P/B is the peak-to-background ratio in measurement time τ in a pure sample. Looking at this formula, it is clear that, for a constant measurement time, to improve detection limits one can increase either the peak count rate or the peak-to-background ratio. Our TES-PIXE setup is extremely well suited for multiple-trace-element detection, because it combines a reasonably good count rate (due to the detector array and high efficiency) with an excellent peak-to-background ratio due to the high-energy resolution, in a wide energy range. WDS spectrometers can be competitive for single-trace-element analysis but simply cannot operate in a 10-keV energy window in the multiple-trace-element mode. The WDS spectrometer also has a higher theoretical upper limit for the count rate, but, because of the lack of detection efficiency, much higher proton-beam currents must be used to achieve similar count rates, which can be a problem for delicate samples.

Using one of the measured lines, we can also try to estimate the current and future TES-PIXE detection limits using Eq. (1). Using the Co $K\alpha$ peak from the Co pigment spectrum, we estimate $P/B \sim 65\,500$, $P \sim 44$ cps, and thus, for the used measurement time of 50 min, we get $C_{\mathrm{MMF}} \sim 35$ ppm. The measurement is performed with 31 pixels, so in the future, by upgrading to the full array capability (160 pixels), the estimated detection limit will decrease by a factor of $\sqrt{31/160}$ to 15 ppm. A further improvement can still be obtained by increasing the proton current and irradiation time, so, for nondelicate samples,

limits below 1 ppm can be achieved. In addition, the origin of the background is presently under study, and it may be reduced in the future, which would lead to a further reduction in the detection limits. These estimates indicate that TES PIXE has the capability of becoming the most sensitive nondestructive analysis technique.

As a final comment on the detection limits, the above analysis concerns only well-separated peaks. If there is peak overlap, detection limits improve superlinearly with the improving energy resolution. Statham [44] introduces several figures of merit proportional to the analysis speed for cases where overlap is important. For example, he estimates that, if a trace-element peak has to be resolved with overlap from another peak, the analysis speed scales as P/FWHM^3, where FWHM is the full-width-at-half-maximum energy resolution. Thus, TES PIXE can give a factor of $(3\ \mathrm{eV}/130\ \mathrm{eV})^3 \sim 10^{-5}$ smaller detection limits compared to standard SDD detectors in those kinds of cases.

IV. CONCLUSIONS

We recently developed a powerful x-ray spectroscopic materials analysis tool [6], which utilizes an array of superconducting transition-edge sensors operated at 0.1 K as the detectors, coupled with an ion-beam (proton) excitation by an accelerator (TES PIXE). Here, we demonstrate the spectroscopic capabilities of the instrument by measuring several complex samples with many elements. The TES detectors clearly give a large advantage over the traditional silicon drift detectors in terms of the capability to identify and resolve a large number (approximately 50) of closely spaced characteristic x-ray peaks over a large energy window (1–10 keV). Much smaller concentrations of trace impurities can be resolved, and in some cases chemical effects are observable (here, in the Ti K-shell transitions). Although high-energy resolution can be obtained with wavelength-dispersive methods, as well, they cannot be operated as efficiently and easily over a broad energy range as what we demonstrate here. The superior detection efficiency of TES detectors also means that smaller excitation currents can be used as compared to wavelength-dispersive detection.

Several physical effects are seen, from both thin-film and bulk samples. Chemical shifts of the positions of the Ti $K\alpha$ and $K\beta$ peaks in atomic-layer-deposited TiO_2 thin films are observable, while collecting data in the full energy range 1–-10 keV. Chemical changes in the $K\alpha/K\beta$ intensity ratios between thin films of Ti, TiN, and TiO_2 are measured. Our data also give a comparison of Ti $K\alpha$ multiple-ionization satellite peak intensities in Ti thin-film compounds. We also study ppm-level impurity contents of several common Co- and Pb-containing pigment materials, discovering low-level impurities, unresolvable with the standard SDD detector, that may possibly be used to fingerprint the material source.

V. OUTLOOK

All the measurements discussed here are performed in vacuum. In PIXE, the excitation beam can be brought to atmosphere, as well, and our cryogenic setup does allow the coupling of x rays from air. This means that there are future prospects of studying specimens that are large or specimens that might not survive the vacuum. Collection efficiency will also be improved by operating the full 160-pixel array. Detector fabrication and readout electronics improvements in the future will also allow for the operation of even larger arrays, possibly up to the kilopixel range, with higher per-pixel count rates.

We also discuss some possible future directions. In terms of impurity analysis, TES PIXE using large detector arrays offers an unparalleled combination of efficiency, resolution, and large energy range, to identify even extremely-low-impurity contents less than ppm from bulk and thin-film samples, in a nondestructive way. This is in contrast to other highly sensitive elemental-analysis methods such as inductively coupled plasma mass spectrometry, which can measure lower concentrations but is destructive and typically starts from a liquid phase (bulk samples), or secondary ion mass spectrometry, which is also destructive and can measure thin films directly. Applications for TES PIXE could include, for example, studies of low-level dopants or defects in semiconductors, with possibly the added bonus of chemical information. For example, a weak phosphorus line at 2.0 keV is easily resolved even next to a very large Si K peak at 1.84 keV with TES PIXE. Mapping is also possible in the future by scanning the proton beam.

Another direction would be studies of biological specimens, as PIXE allows samples in air. For example, the demonstrated chemical sensitivity of Ti lines could be used to study the Ti oxidation state and the distribution of Ti in different organisms. This is especially interesting, as Ti compounds are used as anticancer drugs and because Ti is widely used as an implant material [45]. Naturally, other elements could be considered, as well.

ACKNOWLEDGMENTS

We thank S. Hornytzkyj for providing the pigment samples and M. Reis for discussions. This work is supported by the Finnish Funding Agency for Technology and Innovation TEKES, Academy of Finland Project No. 260880 and Academy of Finland Center of Excellence in Nuclear and Accelerator Based Physics (Ref. 251353), and by the NIST Innovations in Measurement Science program. M. R. J. P. thanks the National Graduate School in Materials Science for funding.

[1] *Particle-Induced X-Ray Emission Spectrometry (PIXE)*, edited by S. A. E. Johansson, J. L. Campbell, and K. G. Malmqvist (Wiley, New York, 1995).

[2] H. R. Verma, *Atomic and Nuclear Analytical Methods* (Springer, New York, 2007), Chap. 1.

[3] J. Szlachetko, M. Cotte, J. Morse, M. Salome, P. Jagodzinski, J.-Cl. Dousse, J. Hoszowska, Y. Kayser, and J. Susinia, Wavelength-dispersive spectrometer for x-ray microfluorescence analysis at the x-ray microscopy beamline ID21 (ESRF), J. Synchrotron Radiat. **17**, 400 (2010).

[4] J. N. Ullom and D. A. Bennett, Review of superconducting transition-edge sensors for x-ray and gamma-ray spectroscopy, Supercond. Sci. Technol. **28**, 084003 (2015).

[5] K. D. Irwin and G. C. Hilton, in *Cryogenic Particle Detection*, edited by Ch. Enss (Springer, New York, 2005).

[6] M. R. J. Palosaari, K. M. Kinnunen, J. Julin, M. Laitinen, M. Napari, T. Sajavaara, W. B. Doriese, J. Fowler, C. Reintsema, D. Swetz, D. Schmidt, J. Ullom, and I. J. Maasilta, Transition-edge sensors for particle induced x-ray emission measurements, J. Low Temp. Phys. **176**, 285 (2014).

[7] J. Uhlig, W. Fullagar, J. N. Ullom, W. B. Doriese, J. W. Fowler, D. S. Swetz, N. Gador, S. E. Canton, K. Kinnunen, I. J. Maasilta, C. D. Reintsema, D. A. Bennett, L. R. Vale, G. C. Hilton, K. D. Irwin, D. R. Schmidt, and V. Sundström, Tabletop Ultrafast X-Ray Microcalorimeter Spectrometry for Molecular Structure, Phys. Rev. Lett. **110**, 138302 (2013).

[8] J. N. Ullom, W. B. Doriese, D. A. Fischer, J. W. Fowler, G. C. Hilton, C. Jaye, C. D. Reintsema, D. S. Swetz, and D. R. Schmidt, Transition-edge sensor microcalorimeters for x-ray beamline science, Synchrotron Radiat. News, **27**, 24 (2014).

[9] J. M. Gildemeister, A. T. Lee, and P. L. Richards, A fully lithographed voltage-biased superconducting spiderweb bolometer, Appl. Phys. Lett. **74**, 868 (1999).

[10] D. A. Bennett, R. D. Horansky, D. R. Schmidt, A. S. Hoover, R. Winkler, B. K. Alpert, J. A. Beall, W. B. Doriese, J. W. Fowler, C. P. Fitzgerald, G. C. Hilton, K. D. Irwin, V. Kotsubo, J. A. B. Mates, G. C. O'Neil, M. W. Rabin, C. D. Reintsema, F. J. Schima, D. S. Swetz, L. R. Vale, and J. N. Ullom, A high resolution gamma-ray spectrometer based on superconducting microcalorimeters, Rev. Sci. Instrum. **83**, 093113 (2012).

[11] K. D. Irwin, Appl. Phys. Lett. **66**, 1998 (1995).

[12] J. A. Chervenak, E. N. Grossman, K. D. Irwin, John M. Martinis, C. D. Reintsema, C. A. Allen, D. I. Bergman, S. H. Moseley, and R. Shafer, Performance of multiplexed SQUID readout for Cryogenic Sensor Arrays, Nucl. Instrum. Methods Phys. Res., Sect. A **444**, 107 (2000).

[13] W. B. Doriese, J. A. Beall, S. Deiker, W. D. Duncan, L. Ferreira, G. C. Hilton, K. D. Irwin, C. D. Reintsema, J. N. Ullom, L. R. Vale, and Y. Xu, Time-division multiplexing of high-resolution x-ray microcalorimeters: Four pixels and beyond, Appl. Phys. Lett. **85**, 4762 (2004).

[14] S. R. Bandler, R. P. Brekosky, A.-D. Brown, J. A. Chervenak, E. Figueroa-Feliciano, F. M. Finkbeiner, N. Iyomoto, R. L. Kelley, C. A. Kilbourne, F. S. Porter, J. Sadleir, and S. J. Smith, Performance of TES X-ray microcalorimeters with a novel absorber design, J. Low Temp. Phys., **151**, 400 (2008).

[15] J. N. Ullom, J. A. Beall, W. B. Doriese, W. D. Duncan, L. Ferreira, G. C. Hilton, K. D. Irwin, C. D. Reintsema, and L. R. Vale, Optimized transition-edge x-ray microcalorimeter with 2.4 eV energy resolution at 5.9 keV, Appl. Phys. Lett. **87**, 194103 (2005).

[16] D. A. Wollman, K. D. Irwin, G. C. Hilton, L. L. Dulcie, D. E. Newbury, and J. M. Martinis, High-resolution, energy-dispersive microcalorimeter spectrometer for x-ray microanalysis, J. Microsc. **188**, 196 (1997).

[17] For a review, see D. E. Newbury, K. D. Irwin, G. C. Hilton, D. A. Wollman, J. A. Small, and J. M. Martinis, in *Cryogenic Particle Detection*, edited by Ch. Enss (Springer, New York, 2005).

[18] Star Cryoelectronics LLC, Santa Fe, New Mexico, USA.

[19] M. A. Reis, P. C. Chaves, and A. Taborda, Radiative auger emission satellites observed by microcalorimeter-based energy-dispersive high-resolution PIXE, X-Ray Spectrom. **40**, 141 (2011).

[20] G. C. Hilton, John M. Martinis, K. D. Irwin, N. E Bergren, D. A. Wollman, M. E. Huber, S. Deiker, and S. W. Nam, Microfabricated transition-edge x-ray detectors, IEEE Trans. Appl. Supercond. **11**, 739 (2001).

[21] J. N. Ullom, W. B. Doriese, G. C. Hilton, J. A. Beall, S. Deiker, W. D. Duncan, L. Ferreira, K. D. Irwin, C. D. Reintsema, and L. R. Vale, Characterization and reduction of unexplained noise in superconducting transition-edge sensors, Appl. Phys. Lett. **84**, 4206 (2004).

[22] High Precision Devices Inc., Boulder, Colorado, USA.

[23] J. W. Fowler, B. K. Alpert, W. B. Doriese, Y.-I. Joe, G. C. O'Neil, J. N. Ullom, and D. S. Swetz, J. Low Temp. Phys. **184**, 374 (2016).

[24] J. L. Campbell, N. I. Boyd, N. Grassi, P. Bonnick, and J. A. Maxwell, The Guelph PIXE software package IV, Nucl. Instrum. Methods Phys. Res., Sect. B **268**, 3356 (2010).

[25] H. Paul and J. Sacher, Fitted empirical reference cross sections for K-shell ionization by protons, At. Data Nucl. Data Tables **42**, 105 (1989).

[26] I. Orlic, C. H. Sow, and S. M. Tang, Experimental L-shell x-ray production and ionization cross sections for proton impact, At. Data Nucl. Data Tables **56**, 159 (1994).

[27] N. J. G. Pearce, W. T. Perkins, J. A. Westgate, M. P. Gorton, S. E. Jackson, C. R. Neal, and S. P. Cheney, A compilation of new and published major and trace element data for NIST SRM 610 and NIST SRM 612 glass reference materials, Geostandards Newsletter **21**, 115 (1997).

[28] J. H. Hubbell and S. M. Seltzer, http://physics.nist.gov/xaamdi.

[29] N. Kallithrakas-Kontos, X-ray chemical shift determination by energy dispersive detection, Spectrochim. Acta B Atom. Spectros. **51**, 1655 (1996).

[30] J. Hasegawa, T. Tada, Y. Oguri, M. Hayashi, T. Toriyama, T. Kawabata, and K. Masai, Development of high-efficiency high-resolution particle-induced x-ray emission system for chemical state analysis of environmental samples, Rev. Sci. Instrum. **78**, 073105 (2007).

[31] S. Contarini, P. A. W. van der Heide, A. M. Prakash, and Larry Kevan, Titanium coordination in microporous and mesoporous oxide materials by monochromated x-ray photoelectron spectroscopy and x-ray Auger electron spectroscopy, J. Electron Spectrosc. Relat. Phenom. **125**, 25 (2002).

[32] S. Fukushima, T. Kimura, K. Nishida, V. A. Mihai, H. Yoshikawa, M. Kimura, T. Fujii, H. Oohashi, Y. Ito, and

M. Yamashita, The valence state analysis of Ti in $FeTiO_3$ by soft x-ray spectroscopy, Microchim. Acta **155**, 141 (2006).
[33] K. F. J. Heinrich, C. E. Fiori, and R. L. Myklebust, Relative transition probabilities for the x-ray lines from the K level, J. Appl. Phys. **50**, 5589 (1979).
[34] L. Rebohle, U. Lehnert, and G. Zschornack, $K\beta/K\alpha$ intensity ratios and chemical effects of some 3d elements, X-Ray Spectrom. **25**, 295 (1996).
[35] O. Sogut, E. Büyükkasap, and H. Erdogan, Chemical-effect variation of $K\beta K\alpha$ x-ray intensity ratios in 3d elements, Radiat. Phys. Chem. **64**, 343 (2002).
[36] G. Brunner, M. Nagel, E. Hartmann, and E. Arndt, Chemical sensitivity of the $K\beta/K\alpha$ x-ray intensity ratio for 3d elements, J. Phys. B **15**, 4517 (1982).
[37] J. Kawai, Chemical effects in the satellites of x-ray emission spectra, Nucl. Instrum. Methods Phys. Res., Sect. B **75**, 3 (1993).
[38] R. L. Kauffman, J. H. McGuire, P. Richard, and C. F. Moore, Projectile and target dependence of the $K\alpha$ satellite structure, Phys. Rev. A **8**, 1233 (1973).
[39] Y. Awaya, T. Kambara, and Y. Kanai, Multiple K- and L-shell ionizations of target atoms by collisions with high-energy heavy ions, Int. J. Mass Spectrom. **192**, 49 (1999).
[40] R. L. Watson, T. Chiao, and F. E. Jenson, Chemical Effect on $K\alpha$ X-Ray Satellites: New Evidence for Interatomic Transitions, Phys. Rev. Lett. **35**, 254 (1975).
[41] O. Benka, R. L. Watson, and R. A. Kenefick, Resonant Electron Transfer in Ionic Fluorine Compounds following $1s2p$ Ionization, Phys. Rev. Lett. **47**, 1202 (1981).
[42] G. Demortier, Review of the recent applications of high energy microprobes in arts and archaeology, Nucl. Instrum. Methods Phys. Res., Sect. B **54**, 334 (1991).
[43] T. O. Ziebold, Precision and sensitivity in electron microprobe analysis, Anal. Chem. **39**, 858 (1967).
[44] P. J. Statham, in *X-ray Spectrometry in Electron Beam Instruments*, edited by D. B. Williams, J. I. Goldstein, and D. E. Newbury (Plenum, New York, 1995).
[45] K. M. Buettner and A. M. Valentine, Bioinorganic chemistry of titanium, Chem. Rev. **112**, 1863 (2012).

PII

MINIMUM DETECTION LIMITS AND APPLICATIONS OF PROTON AND HELIUM INDUCED X-RAY EMISSION USING TRANSITION-EDGE SENSOR ARRAY

by

M. Käyhkö, M. R. J. Palosaari, M. Laitinen, K. Arstila, I. J. Maasilta, J. W. Fowler, W. B. Doriese, J. N. Ullom, T. Sajavaara

Nucl. Instr. Meth B - 406 130–134 (2017)

MINIMUM DETECTION LIMITS AND APPLICATIONS OF PROTON AND HELIUM INDUCED X-RAY EMISSION USING TRANSITION-EDGE SENSOR ARRAY

M. Käyhkö[a], M. R. J. Palosaari[b], M. Laitinen[a], K. Arstila[a], I. J.Maasilta[d], J. W. Fowler[c], W. B. Doriese[c], J. N. Ullom[c], T. Sajavaara[a]

[a] *University of Jyvaskyla, Department of Physics, Postal address: P.O. Box 35, Postal code: FI-40014, City (postal office): University of Jyvaskyla, Country: Finland*
[b] *Stresstech Oy Tikkutehtaantie 1, 40800 Vaajakoski, Finland*
[c] *National Institute of Standards and Technology, 325 Broadway, Boulder, CO 80305, USA*
[d] *University of Jyvaskyla, Department of Physics, Nanoscience Center, Postal address: P.O. Box 35, Postal code: FI-40014, City (postal office): University of Jyvaskyla, Country: Finland*

Abstract

We have determined minimum detection limits, MDLs, for elements $14 \leq Z \leq 86$ using a transition-edge sensor array, TES array, and as a comparison using an Amptek X-123SDD silicon drift detector, SDD. This was done using a 3 MeV proton beam and a 5.1 MeV helium beam. MDLs were determined for a thin film sample on top of C substrate, and for a bulk sample containing mostly Al. Due to the smaller peak-to-background ratio, lower detection limits were obtainable using the TES array for most of the elements. However, for elements $30 \leq Z \leq 45$ the performance of the TES array was not as good as the SDD performance. This is due to the limitations of the TES used at energies > 10 keV. The greatest advantage of TES comes, however, when detecting low intensity peaks close to high intensity peaks. Such a case was demonstrated by measuring a fly ash with overlapping Ti, V, Ba, and Ce peaks, where minimum detection limits of V, Ba, and Ce were decreased by factor of 620, 400, and 680, respectively compared to the SDD.

Keywords: PIXE, TES, Minimum Detection Limit, Helium-induced X-ray Emission

1. Introduction

Particle-induced X-ray emission, PIXE, is a technique capable of detecting concentrations even in parts per million level [1]. Studying small concentration levels is essential in many situations, such as when studying biological samples, atmospheric aerosols, art or archaeological objects [1]. There are many factors limiting the minimum detection limit MDL: the main elemental composition of the sample, peak-to-background ratio, detection efficiency, etc. [1]

Transition-edge sensor, TES, having wide-energy range and great energy resolution has been demonstrated to be a good tool in X-ray spectroscopy [2, 3]. Energy resolution of 3.09 eV was previously demonstrated in our setup [4], and even sub eV resolution has been demonstrated by other authors [5] for detectors operating at lower energies. Good energy resolution makes it easier to separate X-ray lines close in energy, such as Ti Kβ (4.9318 keV) and V Kα (4.9522 keV). This makes the detection of trace elements close to minor or major elements easier than with the commonly used silicon drift detectors, SDDs. On the downside, a single TES pixel is not capable of such high count rates as SDDs, the non-linear energy response adds complexity and each pixel in a TES array detector has its unique behavior.

2. Experimental methods

The measurement setup consists of array of 160 TES pixels detailed in Refs. [4, 3]. Pixels are read with a time division multiplexed SQUID read-out [6]. The measurement chamber with the TES array, silicon drift detector, and sample holder as the main components is illustrated in Fig. 1. In all measurements,

Email address: marko.kayhko@jyu.fi (M. Käyhkö)

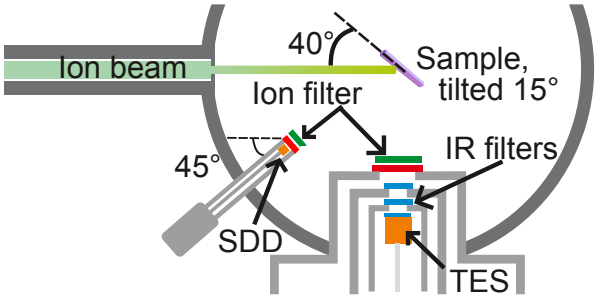

Figure 1: A schematic view of the measurement chamber. The sample is at 40 degree angle with respect to the beam and tilted 15 degree relative to the 2D measurement plane. Transition-edge sensor array, TES, is at 90 degree angle with respect to the beam and the detector chip is 203 mm away from the sample. Silicon drift detector, SDD, is at 45 degree angle compared to the beam and the detector crystal is 199 mm away from the sample. Be filters are used in front of both detectors with 100 μm and 125 μm thicknesses for SDD, and TES, respectively. Between the sample and TES, there is also 3 infrared filters with 225 nm thick Al on 280 nm thick SiN on each, and AP3.3 vacuum window from Moxtek. Silicon drift detector has 12.5 μm thick Be window.

the refrigerator was cooled down to 65 mK with the TES array operated at 100 mK. In the analysis, 98–102 pixels were used, while 120 pixels were read. The pixels that were rejected either had some problems with the line shape, SQUID locking or the pixels did not produce any pulses.

All measurements were done with the 1.7 MV Pelletron accelerator at the University of Jyväskylä. The proton beam was produced using the Pelletron light ion source PELLIS [7], and a 3.01 MeV $^1H^+$ beam was used in all proton measurements. The He-beam was produced with Alphatross, and a 5.11 MeV $^4He^{2+}$ beam was used in all He measurements. The beam was focused to the sample using two quadrupoles after the accelerator, and using a collimator with a 2 mm diameter located before the sample holder. A sample consisting of thin films of Ti, Cr, Cu, and Ge on a Si wafer was measured in the beginning of every measurement day to obtain an energy calibration for the TES array. The details of the measurements are given in Fig. 1 and in Table 1. The target current was not measured, and the accumulated charge was estimated using known reference materials, solid angles, detector efficiencies and X-ray yields. The estimated charges are shown in Table 1.

Table 1: Details of the performed measurements done using 3.01 MeV proton beam and 5.1 MeV He beam. The Au sample is a thin gold foil on carbon substrate manufactured by Institute for Reference Materials and Measurements, IRMM, and the certificated Au thickness was (52.5 ± 2.1) $\mu g/cm^2$. The Al sample is manufactured by NIST, and its standard reference material number is SRM 1255b.

Sample	Au, H	Al, H	Au, He	Al, He
Time, min	60	54	83	103
Cnts/pixel/s	2.97	5.62	0.46	4.16
Good pixels	100	102	98	101
Beam Q/μC	84(4)	40.8(11)	20.5(10)	35.5(10)

3. Analysis methods

3.1. Pulse-processing

All measured pulse shapes for the TES were saved and analyzed later offline. For the pulse processing, home made software was used with optimal filtering algorithm that is orthogonal to constants as described in [8]. After optimal filtering, energy calibration for each pixel was obtained using a known calibration sample containing Si, Ti, Cr, Cu, and Ge. The energy calibration is done after every cooling cycle. Due to the complex nature of the superconducting transition, a cubic spline function is fitted for every pixel. This provides a good energy calibration for the fit region, but does not extrapolate very well outside the fit region, however.

Due to small drifts in the baselines, a drift correction was used. This is mainly caused by the slight drift (10 μK) in the bath temperature of the refrigerator during long measurements. Here, a new algorithm was used for correcting the baseline drift caused by the drift in the temperature. Traditionally this is determined as

$$ph_{dc} = ph[1 + \alpha(B_j - B_0)], \quad (1)$$

where ph is the estimated pulse height, ph_{dc} is the corrected pulse height, B_0 is the baseline level in the beginning of the measurement, B_j is the baseline level for the current pulse, and α is a calibration constant for each pixel [9]. The problem we have had with this approach is that when working in a wide energy-range, the correction has not been satisfactory. The new algorithm is based on the energy calibration of the detector. Let's define a energy calibration function cal so that $E = cal(ph)$, where E is the energy of the photon hitting the detector. The drift corrected energy is calculated as

$$E_{dc} = cal\,(ph + \alpha \cdot \Delta) - cal\,(\alpha \cdot \Delta)\,, \quad (2)$$

where $\Delta = B_j - B_0$, and α is a constant calibrated separately for each pixel. When the baseline changes by Δ, then in the energy calibration curve we move from the point Δ to $ph + \Delta$, instead of just moving from 0 to ph. When thinking about this curve in its physical meaning, the pulse height is related to the temperature of the detector. Since a pulse with height Δ and the constant drift of Δ in the base level do not have the same thermal response, a correction term α is used. In practice, it is often found that the energy calibration curve using standard cubic spline fitting can behave badly close to the zero energy. Thus, two calibration curves are used, one with a cubic spline fitting for higher energies (term $cal\,(ph + \alpha \cdot \Delta)$, and another, 2nd order polynomial fit for lower energies (term $cal\,(\alpha \cdot \Delta)$).

Pile-up pulses and other bad pulses are rejected from the analysis. Due to this, a dead time correction is needed in quantitative analysis. The dead time correction is defined by the number of accepted events divided by the number of photons arrived at the detector $\chi = {}^{N_{good}}/_{N_{ph}}$. The number of photons arrived at the detector can be approximated with the equation

$$N_{ph} \approx \frac{N_{ev}}{1 - \tau \cdot {}^{N_{ev}}/_{T}}, \tag{3}$$

where N_{ph} is the actual number of photons arrived at the detector, N_{ev} is the number of events (some with pile-up) in the saved data, τ is the recorded pulse length (16.384 ms in all measurements), and T is the measurement time as shown in Table 1. The obtained corrections for the proton beam measurements were 0.820 for the thin film sample, and 0.827 for the bulk sample. The corrections for helium beam measurements were 0.949 for the thin film sample, and 0.848 for the bulk sample.

3.2. Minimum detection limit calculations

We use the common definition for minimum detection limit yield Y_{MDL}

$$Y_{MDL} = 3\sqrt{Bg_{fwhm}}, \tag{4}$$

where Bg_{fwhm} is the background area in the full width at half maximum region [1]. This definition is valid in the situation where the peak height is much higher than the background level and the peaks are well separated [10]. The X-ray yield for a thin target can be written as

$$Y_{MDL} = Y_{it}\,(Z) \cdot m_{a,MDL} \cdot \gamma\,(Z)\,, \tag{5}$$

where $m_{a,MDL}$ is the concentration (in ${}^{g}/_{cm^2}$), $Y_{it}\,(Z)$ is theoretical yield in unit ${}^{1}/_{str \cdot C {}^{g}/_{cm^2}}$ containing cross sections and known physical constants, and γ is the experimental yield (in unit $C \cdot str$) calibrated using standards, containing experimental parameters like solid angle, filter transmission, and detector efficiency [1]. Now we can write

$$m_{a,MDL} = \frac{3\sqrt{Bg_{fwhm}}}{Y_{it}\,(Z, E_0)\,\gamma\,(Z)}. \tag{6}$$

The same equation holds for a thick target specimen, with the exception that the theoretical yield is in unit ${}^{1}/_{str \cdot C \cdot ppm}$ [1].

The extraction of peak areas for the TES spectra were done using fityk version 1.3.0 [11]. The peaks were fitted using Voigt profiles. The X-ray background was fitted using a self-made computer code, the X-ray yields were calculated using GUPIXwin version 2.2.4 [12] and SDD spectra were analyzed using GUPIXwin, except for the background determination which was fitted using the self-made code.

3.2.1. TES area corrections

K shell

Kα transition is split into two lines: Kα_1, and Kα_2 and the ratio is circa 100/50 [13]. In minimum detection calculations it is thus always beneficial to include both of these lines in the calculation. When one includes Kα_2 in the calculation, the increase in area is 50%, and the increase in required area for the detection limit (due to the increased background area) of an element increases in the worst case by $\sqrt{2} \approx 41$ %. The width of the analysis area is then defined as

$$W = FWHM + \min\left(\Delta E_{K\alpha 1 - K\alpha 2}, FWHM\right), \tag{7}$$

where $FWHM$ is the full width at half maximum, and $\Delta E_{K\alpha 1 - K\alpha 2}$ is the energy difference of the $K\alpha_1$, and $K\alpha_2$ lines. In other words this means the energy region spans from $E_{K\alpha 2} - HWHM$ to $E_{K\alpha 1} + HWHM$, when $\Delta E_{K\alpha 1 - K\alpha 2} < FWHM$, where $HWHM$ is the half width at half maximum. When $\Delta E_{K\alpha 1 - K\alpha 2} > FWHM$, we analyze the FWHM region around both $K\alpha_1$, and $K\alpha_2$ peaks. Since the integration area for different elements is now different relative to the full intensities, we use a correction term A. The correction term is defined so that completely separated Kα_1, and Kα_2 peaks have $A = 1$. Assuming Gaussian line shapes we get

$$A = \frac{\left[erf\left(\sqrt{\ln 2}\right) + erf\left(\frac{\Delta' + \sqrt{2 \ln 2}}{\sqrt{2}}\right)\right]}{2 \cdot erf\left(\sqrt{\ln 2}\right)}, \tag{8}$$

when $\Delta' = \frac{(E_{K\alpha_1} - E_{K\alpha_2})}{\sigma} < 2\sqrt{2\ln 2}$. When we have $\Delta' = \frac{(E_{K\alpha_1} - E_{K\alpha_2})}{\sigma} > 2\sqrt{2\ln 2}$ we obtain

$$A = 1 + \frac{\left[erf\left(\frac{\Delta' + \sqrt{2\ln 2}}{\sqrt{2}}\right) + erf\left(-\frac{\Delta' + \sqrt{2\ln 2}}{\sqrt{2}}\right)\right]}{2 \cdot erf\left(\sqrt{\ln 2}\right)}. \quad (9)$$

L shell

Lα is split into two lines: Lα_1, and Lα_2 and the ratio is circa 100/11 [13]. Thus in minimum detection calculations we want to use only the $L\alpha_1$ line. But since for lighter elements these lines overlap, we will include an area correction term like we did for the K shell. The case where $L\alpha_1$, and $L\alpha_2$ are completely separated has a correction $A = 1$. The obtained correction is now

$$A = \frac{erf\left(\sqrt{\ln 2}\right) + \frac{1}{18}\left[erf\left(H_3\left(\delta\right)\right) - erf\left(H_2\left(\delta\right)\right)\right]}{erf\left(\sqrt{\ln 2}\right)},$$

where $H_3 = \frac{\sqrt{2\ln 2} + \delta}{\sqrt{2}}$, and $H_2 = \frac{-\sqrt{2\ln 2} + \delta}{\sqrt{2}}$, and $\delta = \frac{(E_{L\alpha 1} - E_{L\alpha 2}) \cdot 2\sqrt{2\ln 2}}{\mathrm{FWHM}}$.

3.2.2. Multiple ionization corrections

For a 5.1 MeV He beam, the multiple ionization [14, 15] becomes a notable effect and requires corrections for the TES analysis. Since the majority of the observed x-rays are from single ionization transitions, the used correction term is the KL^0 fraction, i.e. the fraction of photons from single ionization. This was determined for the calibration sample, and it was 0.55(2), 0.76(8), 0.81(3), 0.83(3), for Si, Ti, Cr, and Cu, respectively. For this data, we fitted a phenomenological function $f\left(Z\right)$ for the KL^0 fraction obtaining

$$f\left(Z\right) = 1 - a_0 \cdot Z^{-a_1} \quad (10)$$

with $a_0 = 21.033$ and $a_1 = 1.453566$.

The multiple ionization correction for the L-shell could not be estimated due to the lack of Lα transitions in the measured spectra. The multiple ionization of Lα has been studied little [16], and we could not find previous studies that would have given the answer for this.

3.2.3. Full widths at half maximum

In the contex of minimum detection limit determination, with full width at half maximum (FWHM) we mean the convolution of instrumental FWHM, natural line widths [17], and X-ray fine structure (α_1, and α_2). The instrumental resolution was determined from the proton measurements for Si Kα, Al Kα , and Cr Kα. Si, and Al peaks were fitted with two Voigt profiles (Kα_1 and Kα_2), whereas Cr Kα complex was fitted with 7 peaks (5 Kα_1 and 2 Kα_2 peaks) [18]. The obtained instrumental energy resolutions were: (6.59 ± 0.09) eV (Si Kα), (6.90 ± 0.06) eV (Cr Kα) in the first measurement day, and (6.45 ± 0.07) eV (Al Kα), (6.36 ± 0.03) eV (Si Kα) in the second measurement day. In the analysis, we used the average value 6.6 eV for the instrumental resolution. An example of fitted Si Kα, and Cr Kα peaks is shown in Fig. 2.

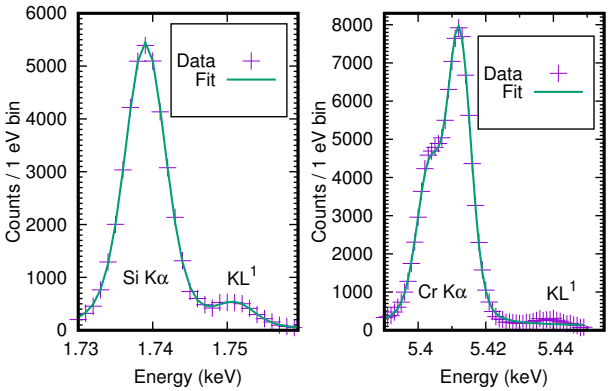

Figure 2: Fitted Si Kα and Cr Kα peaks with fitted FWHMs being (6.36 ± 0.03) eV, and (6.90 ± 0.06) eV, respectively. For the Si Kα complex, two Voigt profiles were used (α_1, and α_2) and for the Cr Kα complex seven Voigt profiles were used: 5 for α_1 and 2 for α_2 [18]. Both spectra were measured using a 3.01 MeV proton beam.

For SDD the FWHM was estimated by GUPIXwin, where it was fitted using the equation $FWHM = {}^{2.355}/_{A2}\sqrt{A4 + A5 \cdot E}$, where $A2 = 143.674\,{}^{1}/_{\mathrm{keV}}$, $A4 = 33.1219$, and $A5 = 9.6594\,{}^{1}/_{\mathrm{keV}}$ are calibration constants.

4. Results and Discussion

The minimum detection limits for both samples are plotted in Figs. 3, and 4. The shape of the minimum detection limit curve is mainly influenced by the x-ray yield and the shape of the background. Both x-ray yield and background decrease with increasing Z. At first the nearly exponential background decrease (see Fig. 5) dominates and improves the minimum detection limits until at some point the background is near zero and x-ray yield starts to dominate and worsens the detection limits. Thus two "U-shapes"

are formed, one for the K-shell and the another for the L-shell.

A comparison of proton and helium backgrounds for SRM 1255b sample (bulk Al) is show in Fig. 5. The background from the helium measurement is lower than for the proton beam, which allows lower detection limits with He beam in some cases.

We measured trace elements in a fly ash sample with 50:50 ratio of bio and peat fuel. The full spectrum is shown in Fig. 6 and zoomed in 4.2–5.7 keV region is shown in Fig. 7. The overlapping of Ti K lines, V K lines, Ba L lines, and Ce L lines is evident in Fig. 7. In the case of overlapping peaks, the equation (4) does not hold [10]. We follow the definitions in [10]: If peak separation, *sep*, $>$ 2 FWHM peaks are separated, if $sep < {}^{\mathrm{FWHM}}/_{10}$ the overlap is severe, otherwise there is some overlap. For the α_1 peaks of the previously mentioned elements, this means that for Ti, V, and Ba there is no overlap, and for Ce there is some overlap in the TES spectrum. For SDD, there is some overlap for Ti, V, Ba and severe overlap for Ce. The MDL in these situations can be written as

$$MDL = cons \cdot FWHM^n, \tag{11}$$

where $n = 0.5$ for non overlapping peaks, $n = 1.5$ for severe overlap of two peaks, and n =0.5–1.5 when there is some overlapping [10]. This equation assumes that the peak areas are roughly the same, and that the background level is high relative to the peaks. Using resolutions of 6.6 eV for the TES and 145 eV for the SDD, and assuming the same detection geometry and efficiency, we can calculate that the MDL improves by a factor of 620 ($n = 1.4825$ for SDD), 400 ($n = 1.3947$ for SDD), and 680 ($n = 0.5$ for TES) for V, Ba, and Ce, respectively. The n values for peaks with some overlap were approximated linearly using values $n = 0.5$ at $sep = 2 \cdot FWHM$, and $n = 1.5$ at $sep = 0.1 \cdot FWHM$.

5. Conclusions

We have observed improvements in the detection limits for the TES array compared to the SDD detector for the most elements in the case of well separated peaks. Elements $30 \leq Z \leq 45$ are the hardest to detect because of the limitations in detection efficiency for high energy X-rays with our type of TES and high absorption for low energy X-rays in the current setup. When comparing the helium and the proton beam, the helium beam is better for thin film samples whereas the proton beam is better for bulk samples due to the deeper penetration depth.

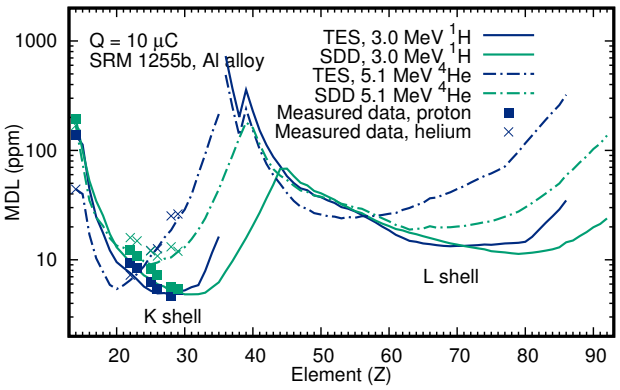

Figure 3: Minimum detection limits for elements $Z \geq 14$ using Kα and Lα peaks in the analysis (both shown for SDD) for elements in matrix made mostly of Al (SRM 1255b). The odd behaviour in MDL for TES at $Z = 38$ is due to the Bi M-shell absorption edge (Bi is the absorber material in the TES detector) . At the peak positions ($Z \approx 40$), the L-shell detection limits start to be lower than the K-shell detection limits.

The advantage of TES becomes clear when detecting overlapping peaks of trace and minor elements. In this case, the minimum detection limit scales as $FWHM^n$, where $0 \leq n \leq 1.5$ for two identical peaks. Such an example is the measured fly ash sample with overlapping Ti, V, Ba, and Ce peaks at around 5 keV energy. In this case, there was an overlap of Ti, V, Ba, and Ce lines. An improvement in the detection limit of 620, 400, and 680 was calculated for V, Ba, and Ce, respectively for the measured fly ash. In this analysis, however, there were slightly different experimental parameter for the detectors: different detection angles, different X-ray filters (ion filter in Fig. 1), and different vacuum windows. These effects were not taken into account in the normalization. Also the different detection angles lead to slightly different secondary electron Bremsstrahlung background, which also affects the detection limits.

Acknowledgements

This work was partly supported by the Academy of Finland Centre of Excellence in Nuclear and Accelerator Based Physics (Ref. 251353). We thank Jyväskylän Energia Oy for providing the fly ash sample.

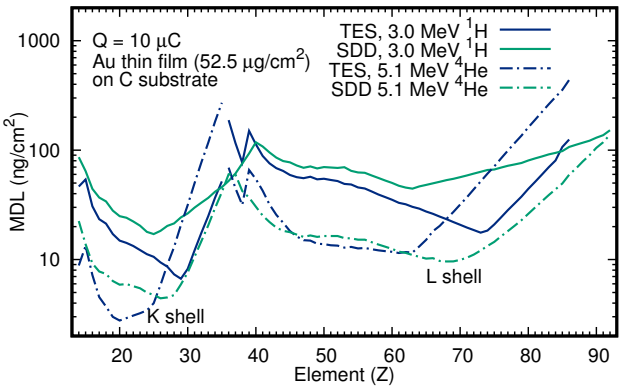

Figure 4: Minimum detection limits for elements $Z \geq 14$ using Kα and Lα peaks in the analysis (both shown for SDD) for thin gold film on carbon substrate. The odd behaviour in MDL for TES at $Z = 38$ is due to the Bi M-shell absorption edge. At the peak positions ($Z \approx 40$), the L-shell detection limits start to be lower than the K-shell detection limits.

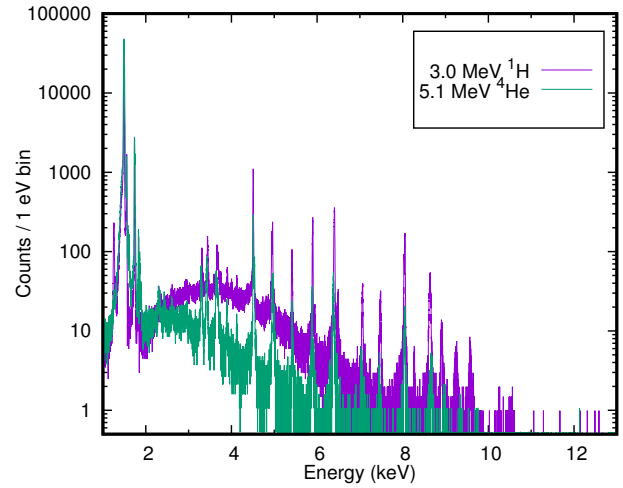

Figure 5: Background comparison of the He and proton beams for the TES detector with 3.0 MeV proton and 5.1 MeV He beams for the bulk Al sample. Both spectra are normalized to $Q = 10\,\text{particle} \cdot \mu\text{C}$.

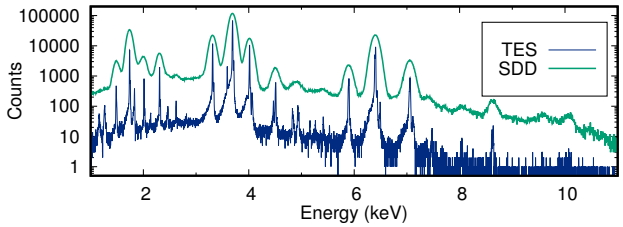

Figure 6: Measured fly ash spectra for SDD and TES. Measured fly ash contained bio / peat fuel with 50:50 ratio.

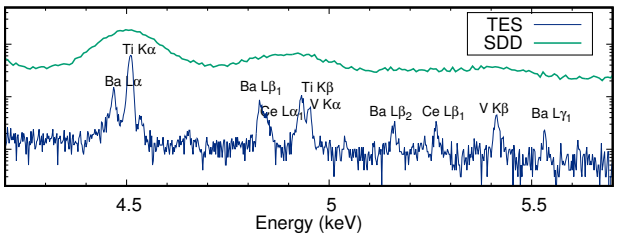

Figure 7: Measured fly ash spectra for SDD and TES, zoomed.

References

[1] Sven A. E. Johansson, John L. Campbell, and Klas G. Malmqvist. *Particle-Induced X-Ray Emission Spectrometry (PIXE)*. A Wiley-Interscience Publication, New York, 1995.

[2] G.C. Hilton, D.A. Wollman, K.D. Irwin, L. L. Dulcie, N. F. Bergren, and J.M. Martinis. Superconducting transition-edge microcalorimeters for x-ray microanalysis. *IEEE Transactions on Applied Superconductivity*, 9(2):3177–3181, 1999.

[3] M. R. J. Palosaari, M. Käyhkö, K. M. Kinnunen, M. Laitinen, J. Julin, J. Malm, T. Sajavaara, W. B. Doriese, J. Fowler, C. Reintsema, D. Swetz, D. Schmidt, J. Ullom, and I. J. Maasilta. Broadband ultrahigh resolution spectroscopy of particle induced x-rays: Extending the limits of non-destructive analysis. *Physical Review Applied*, accepted.

[4] M. R. J. Palosaari, K. M. Kinnunen, J. Julin, M. Laitinen, M. Napari, T. Sajavaara, W. B. Doriese, J. Fowler, C. Reintsema, D. Swetz, D. Schmidt, J. Ullom, and I. J. Maasilta. Transition-Edge Sensors for Particle Induced X-ray Emission Measurements. *Journal of Low Temperature Physics*, 176(3-4):285–290, 2013.

[5] S. J. Lee, J. S. Adams, S. R. Bandler, J. A. Chervenak, M. E. Eckart, F. M. Finkbeiner, R. L. Kelley, C. A. Kilbourne, F. S. Porter, J. E. Sadleir, S. J. Smith, and E. J. Wassell. Fine pitch transition-edge sensor X-ray microcalorimeters with sub-eV energy resolution at 1.5 keV. *Applied Physics Letters*, 107(22):223503, 2015.

[6] W. B. Doriese, J. A. Beall, W. D. Duncan S. Deiker, L. Ferreira, G. C. Hilton, K. D. Irwin, C. D. Reintsema, J. N. Ullom, L. R. Vale, and Y. Xu. Time-division multiplexing of high-resolution x-ray microcalorimeters: Four pixels and beyond. *Appl. Phys. Lett.*, 85:4762, 2004.

[7] T. Kalvas, O. Tarvainen, J. Komppula, M. Laitinen, T. Sajavaara, H. Koivisto, A. Jokinen, and M. P. Dehnel. Recent negative ion source activity at JYFL. In *AIP Conference Proceedings*, volume 1515, pages 349–358. AIP Publishing, 2013.

[8] B. K. Alpert, R. D. Horansky, D. A. Bennett, W. B. Doriese, J. W. Fowler, A. S. Hoover, M. W. Rabin, and J. N. Ullom. Filters for High Rate Pulse Processing. *Journal of Low Temperature Physics*, 184:374–381, 2016.

[9] J. W. Fowler, B. K. Alpert, W. B. Doriese, Y.-I. Joe, G. C. O'Neil, J. N. Ullom, and D. S. Swetz. The Practice of Pulse Processing. *Journal of Low Temperature Physics*, 184:374–381, 2016.

[10] P. J. Statham. Quantifying Benefits of Resolution and Count Rate in EDX Microanalysis. In David B. Williams, Joseph I. Goldstein, and Dale E. Newbury, editors, *X-Ray Spectrometry in Electron Beam Instruments*, pages 101–

126. Springer US, 1995. DOI: 10.1007/978-1-4615-1825-9_8.

[11] Marcin Wojdyr. *Fityk* : a general-purpose peak fitting program. *Journal of Applied Crystallography*, 43(5):1126–1128, 2010.

[12] J. L. Campbell, N. I. Boyd, N. Grassi, P. Bonnick, and J. A. Maxwell. The Guelph PIXE software package IV. *Nuclear Instruments and Methods in Physics Research Section B: Beam Interactions with Materials and Atoms*, 268(20):3356–3363, 2010.

[13] A. C. Thompson. *X-ray Data Booklet*. Lawrence Berkeley National Laboratory, University of California, 2009.

[14] P. G. Burkhalter, A. R. Knudson, D. J. Nagel, and K. L. Dunning. Chemical Effects on Ion-Excited Aluminum K X-Ray Spectra. *Physical Review A*, 6(6):2093–2101, 1972.

[15] P. Richard, J. Bolger, D. K. Olsen, and C. F. Moore. Molecular structure effects of aluminum $K\beta$ x-ray spectra produced in proton and alpha particle excitation. *Physics Letters A*, 41(3):269–271, 1972.

[16] T. Hanada, M. Mogi, Kawai Jun, K. Maeda, Y. Sasa, and M. Uda. Nickel Lα spectra measured by a high resolution particle induced X-ray emission (PIXE) spectrometer. *Nuclear Instruments and Methods in Physics Research Section B: Beam Interactions with Materials and Atoms*, 75(1):35–37, 1993.

[17] M. O. Krause and J. H. Oliver. Natural widths of atomic k and l levels, ka x-ray lines and several kll auger lines. *Journal of Physical and Chemical Reference Data*, 8(2):329–338, 1979.

[18] G. Hölzer, M. Fritsch, M. Deutsch, J. Härtwig, and E. Förster. $K\alpha_{1,2}$ and $K\beta_{1,3}$ x-ray emission lines of the 3d transition metals. *Physical Review A*, 56(6):4554–4568, 1997.

PIII

HEAVY ION INDUCED TI X-RAY SATELLITE STRUCTURE FOR TI, TIN, AND TiO_2 THIN FILMS

by

M. Käyhkö, M. R. J. Palosaari, M. Laitinen, K. Arstila, I. J. Maasilta, T. Sajavaara

Accepted for publication in X-ray spectrometry

Heavy ion induced Ti X-ray satellite structure for Ti, TiN, and TiO_2 thin films

Abstract

X-ray emission spectra of three different titanium-containing thin films, Ti, TiO_2, and TiN, were measured using 5.1 MeV $^{7}Li^{2+}$, 4.4–6.8 MeV $^{12}C^{3+}$, 6.8 MeV $^{16}O^{3+}$ and 11.9 MeV $^{63}Cu^{6+}$ beams as excitation. The energy spectra were collected using a high energy resolution transition-edge sensor array. In all measurements, the average L-shell vacancy fraction was higher for the metallic Ti than for the other samples, whereas the difference between TiN and TiO_2 was negligible. The universal variable X_n of the geometrical model was used to study the systematics of the average L-shell vacancy fraction at the time of Kα emission. Our experiments expands previously studied X_n values, and a fairly good agreement with previous studies was found.

1. Introduction

Particle-induced X-ray emission (PIXE) is a routine ion beam analysis (IBA) technique for quantitative elemental analysis [1]. In addition, PIXE has been demonstrated to be useful for chemical speciation already in the 1970s using high energy resolution wavelength-dispersive detectors which operate in a narrow energy-region [2, 3, 4, 5].

The chemical sensitivity of PIXE can emerge either from energy shifts of the X-rays [2, 3], from the relative intensity changes of different diagram lines [6] (lines caused by a single electron vacancy), or from the relative intensity changes of X-ray satellite lines [4] (lines with two or more electron vacancies). In the first case, the shift is typically 0.1–1 eV [7]. In the second case, the ratio of, for example, Kα and Kβ transitions is monitored. This ratio has been reported to differ up to 10 % between different compounds [6]. In the last case, heavy ions with greater energy loss (He or heavier) are used to achieve multiple ionization of the target atoms. In multiple ionization, along with the inner-shell electron, also outer-shell electrons can be excited to vacuum level. Depending on how many outer-shell electrons are excited, the energy of the emitted photon is changed, and instead of a single peak, multiple peaks appear in the energy spectrum. These can be resolved if the energy-resolution of the detector is sufficient. The rearrangement of the outer-shell electrons that happen prior to the X-ray emission is also affected by the chemical environment of the atom, either because the electrons are directly involved in bonds or because of interatomic electron transitions [4]. These rearrangements can cause significant changes in relative intensities between different satellite lines, making the technique sensitive to the chemical environment.

Previously several studies, e.g. [4, 8, 9, 10, 11, 12, 13], have reported the effect of different chemical environments on Kα X-ray satellite structures. Most of these studies have focused on the 3rd-row elements (a total of 15 was calculated in a review by Raman [14]), but a few studies has been carried out on the 4th-row elements, like V [10], Cr [15] and Mn [16]. Some studies of Kα X-ray satellite structures have been made for elemental metals, like Ti [17, 18].

In this work, we have used energy-dispersive superconducting transition-edge sensor (TES) array to study Ti Kα X-ray satellite structures of three titanium-containing thin films by heavy ion bombardment. Titanium compounds have been measured earlier with a proton beam [19, 20, 21], but no studies for these compounds using heavy ions exist. We report Ti Kα X-ray satellite line intensities for 50 nm thick TiN, TiO_2, and Ti thin films, as well as energy shifts of these lines for four different incident ions, 5.1 MeV $^{7}Li^{2+}$, 4.4–6.8 MeV $^{12}C^{3+}$, 6.8 MeV $^{16}O^{3+}$ and 11.9 MeV $^{63}Cu^{6+}$.

2. Experimental methods

The TES array at the University of Jyväskylä consists of 160 individual pixels with time-division multiplexed SQUID read-out. The TES array was at 90-degree angle relative to the beam direction and the sample surface normal was at 40-degree angle with respect to the beam direction and tilted 15 degrees relative to the horizontal plane. The used detector system is described in more detail in references [21, 22].

During the measurements, the TES array was cooled down to approximately 100 mK and circa 100 pixels were used in the analysis. Between the detector and the sample, there was a 125 μm thick Be foil, an AP3.3 vacuum window from MOXTEK Inc., and three in-house fabricated infrared-filters with a 225 nm thick Al layer on top of a 280 nm thick silicon nitride film on each.

The measurements were performed with the 1.7 MV Pelletron accelerator at the University of Jyväskylä. Before each measurement, an energy calibration sample containing Si, Ti, Cr, Cu, and Ge was measured using a 3.0 MeV proton beam. The beam spot size in the measurements was circa 30 mm^2. All measurements were performed under approximately 10^{-6} mbar pressure, and the samples were grounded to avoid charging.

The thin film samples were grown on top of a silicon wafer. The TiN and TiO_2 thin films were deposited using atomic layer deposition (ALD), and the Ti film was deposited using electron-beam evaporation. All the films had a thickness of circa 50 nm. The film compositions were verified by time-of-flight elastic recoil detection analysis [23].

All the samples were measured with 11 different ion beams: 5.1 MeV $^{7}Li^{2+}$, 6.8 MeV $^{16}O^{3+}$, 11.9 MeV $^{63}Cu^{6+}$, 4.4 MeV $^{12}C^{2+}$, 4.8 MeV $^{12}C^{2+}$4.8 MeV $^{12}C^{3+}$, 5.2 MeV $^{12}C^{3+}$, 5.6 MeV $^{12}C^{3+}$, 6.0 MeV $^{12}C^{3+}$, 6.4 MeV $^{12}C^{3+}$ and 6.8 MeV $^{12}C^{3+}$. The measurement time per sample varied from 1 hour to 3 hours. The count rate was 8–10 Hz/pixel during most measurements, except for the 11.9 MeV $^{63}Cu^{6+}$ beam, where the count rate was smaller because smaller beam current available at the time. The target current was estimated using either measured or predicted cross-sections [25, 24, 26]. The average current in the target was calculated to be 2–40 particle $\cdot$ nA in each measurement, and the total accumulated charge was estimated to be between 10 and 500 μC. The beam current and beam fluence was selected to have good statistics in collected spectra and due to large variation in X-ray production cross sections between different ion/energy combinations, variations in the used ion beam currents between different measurements were high.

The measured pulse shapes were saved and analyzed. For the pulse-processing, an analysis code was used with optimal filtering orthogonal to constants described in Ref. [27]. The extraction of peak areas and positions were done using Fityk version 1.3.0 [28]. Multiple ionization satellite lines were fitted using the Voigt profile. The Gaussian component width is assumed to be mainly a detector feature, and the Lorentzian component width is assumed to originate from the natural linewidth [18]. In the fit, the Gaussian width and exponential tail parameters (detector features [29]) were fixed. The width of the Lorentzian component, the peak position, and the peak area were free parameters. The Gaussian width (6 eV) and exponential tail parameter values were determined from Ti Kα peak measured using a 3.0 MeV proton beam prior to each heavy ion measurement. The fit included two peaks (Ti Kα_1, Ti Kα_2) with fixed intensity ratio and positions.

An example of measured X-ray emission spectra from Ti film on Si substrate excited with three different ion beams is shown in Fig. 1. Satellite peaks are clearly seen at energies above the diagram lines (Si Kα, Si Kβ, Ti Kα, and Ti Kβ).

3. Analysis methods

When studying intensity distributions, a useful parameter is the apparent average L vacancy fraction p_L at the time of Kα X-ray emission (for KαL transitions)

$$p_L = \frac{1}{N}\sum_n n f_n, \tag{1}$$

where N is the number of L-shell electrons in the ground state (8 for Ti) and f_n the fractional intensity of the nth satellite line [4]. The average L vacancy fraction increases rapidly with an increasing incident ion atomic number and reaches the maximum around $Z_1 \approx Z_2$, where Z_1 is the atomic number or effective charge of the incident ion and Z_2 the atomic number of the target atom [14].

Theoretical model known as the geometrical model (GM) was developed to study the systematics of the p_L [30]. The model predicts that the number of spectator vacancies at shell n ($n = 1\,(\mathtt{K}), 2\,(\mathtt{L}), 3\,(\mathtt{M}), ...$) is a function of the universal variable X_n

$$X_n = \frac{4V\sqrt{G\,(V)}Z_1}{nv_1}, \tag{2}$$

where v_1 is the velocity of the incident ion, v_2 is average velocity of electron in n shell, $V = {}^{v_1}/_{v_2}$, Z_1 the atomic number or effective charge of the incident ion, and $G\,(V)$ is the binary encounter approximation (BEA) scaling

function in equation [31]

$$\sigma = \frac{NZ_1^2\sigma_0}{U^2} G\left(V\right), \tag{3}$$

where σ is the ionization cross-section, $N = 8$ for L-shell, $\sigma_0 = \pi e^4$ is a constant, and U is the electron binding energy. The universal variable can be interpreted as the measure of the perturbation strength that characterizes the collision. The universal variable has been fitted to equation

$$p_L = \frac{a}{1 + \left(b/X_n\right)^c} \tag{4}$$

by Horvat et al. [18] with parameters $a = 0.537 \pm 0.006$, $b = 2.11 \pm 0.08$, and $c = 2.02 \pm 0.03$. In this work we take the same approach as in Ref. [18]: Z_1 is the incident ion atomic number, v_2 is calculated from L3 shell binding energy (455 eV) [32], and $G\left(V\right)$ is calculated using Eq. (6) from Reference [31].

GM can be used to explain the effect of the incident ion, and the incident ion energy, but not the effect of chemical environment. To study chemical environment, the average total valence-electron density D_V of a compound is a parameter that has been shown to correlate with p_L values. It can be calculated as [4]

$$D_V = 0.602 \frac{n_v \rho}{\mu_{mol}}, \tag{5}$$

where n_v is the total number of valence electrons, ρ the mass density and μ_{mol} the molecular weight.

One approach to explain the shape of the ionization structure is to use the binomial distribution [14]. We define that the ionization probability for the 2s electrons is P_{2s} and the ionization probability for the 2p electrons is P_{2p}. Now the probability to ionize n_1 electrons from the 2s-orbital and n_2 electrons from the 2p-orbital is then

$$\begin{aligned} &f = f\left(n_1, n_2\right) = \\ &\binom{2}{n_1} \cdot P_{2s}^{n_1} \left(1 - P_{2s}\right)^{2-n_1} \cdot \binom{6}{n_2} \cdot P_{2p}^{n_2} \left(1 - P_{2p}\right)^{6-n_2}. \end{aligned} \tag{6}$$

The probability to ionize a total of n electrons is

$$f_n = \sum_{n_1+n_2=n} f_{n_1 n_2}. \tag{7}$$

It should be noted that this model does not take into account the rearrangement process prior to X-ray emission or the varying fluorescence yield for differently ionized L-shell [14]. Furthermore, if we assume $P_{2s} = P_{2p}$, then $P_{2s} = p_L$. This assumption is made for simplicity and for the fact that p_L is a parameter that can be measured experimentally and therefore it is straightforward to compare the model to the experiment.

We expand the model to take into account L-hole filling prior to X-ray emission using the probability of a single hole filling P_f and the number of available outer shell electrons χ. The probability to have n holes at the time of X-ray emission is

$$f_n^* = f_n + f_{gain} - f_{lost}, \tag{8}$$

where

$$f_{gain} = \sum_{j=n+1}^{8} f_j \cdot \binom{\chi}{j-n} \cdot P_f^{j-n} \cdot \left(1 - P_f\right)^{\chi - j + n}, \tag{9}$$

and

$$f_{lost} = f_n \sum_{k=1}^{n} \binom{\chi}{k} P_f^k \left(1 - P_f\right)^{\chi - k}. \tag{10}$$

Here f_{gain} is the probability to end with n vacancies when more than n vacancies were generated in the impact, and f_{lost} is the probability to end up with less than n vacancies when n vacancies were generated during the impact.

4. Results

The measured X-ray spectra of Ti, TiN and TiO_2 thin films around Ti Kα and Ti Kβ (for the $^{7}Li^{2+}$ beam) are shown in Figures 2–3 and an example of a fitted spectrum is given in Fig. 4. All samples were measured with seven different $^{12}C^{3+}$ ion energies, as well as with a 4.8 MeV $^{12}C^{2+}$ beam, a 5.1 MeV $^{7}Li^{2+}$ beam, a 6.8 MeV $^{16}O^{3+}$ beam and a 11.9 MeV $^{63}Cu^{6+}$ beam.

To study the possible beam induced damage to the samples and detector energy stability, data was analyzed in a list mode. In Figure 5 a) the relative peak position of Ti KαL^0 line and in Figure 5 b) the KαL^0 fractions are plotted as a function of real time. It can be noted that some shifts occur in the energy during the measurements, but the KαL^0 fractions are stable through out the measurements, with the exception of few data points due to fit reaching a different kind of Voigtian shape compared to the other fits. It is known that the TES gain drifts during the measurements, and it can be corrected [33]. The used drift correction algorithm ([34]) is designed for narrow X-ray lines, not for complicated and wide X-ray satellite structures, and thus it is unable to correct the systematic error in gain. For this reason, the observed peak position shifts are believed to be caused by the natural TES gain drift. For these reasons, we conclude that no actual changes in the chemical environment that would hinder our experiments happened during the experiments. Due to higher uncertainty in the absolute energy of Ti KαL^0 lines, we have only reported the peak positions relative to the KαL^0 peak.

5. Discussion

The average L-shell ionization probability p_L at the time of Kα X-ray emission for the $^{12}C^{2+/3+}$ beam measurements is plotted in Figure 6. It has been observed [4] that the average valence shell electron density D_v follows p_L. Calculated values for D_v are 0.227, 0.457, and 0.456, for Ti, TiN and TiO_2, respectively. The same is seen in Figure 6, as well. Both TiO_2 and TiN have nearly identical D_v and p_L values, whereas Ti has clearly different values of D_v and p_L. The changes in p_L between different Ti-containing samples are modest in single measurements, but with multiple measurements with varying $^{12}C^{3+}$ ion energy the difference between Ti, and TiN/TiO_2 becomes clear.

For $^{63}Cu^{6+}$ and $^{7}Li^{2+}$ ions, the same correlation in the p_L values was observed. The values using the $^{63}Cu^{6+}$ beam were 0.266 ± 0.015, 0.255 ± 0.012, 0.253 ± 0.013, for Ti, TiN and TiO_2, respectively. The p_L values from the $^{7}Li^{2+}$ beam were 0.066 ± 0.003, 0.062 ± 0.002 and 0.058 ± 0.003, for Ti, TiN and TiO_2, respectively. The analyzed multiple ionization fractions are plotted in Figure 7 for the $^{63}Cu^{6+}$ beam and in Figure 8 for the $^{7}Li^{2+}$ beam.

We have studied the systematics of p_L values for the metallic titanium film using the geometrical model (GM) (Eq. (2)), and fitted the data using Eq. (4). Measured data, the best fit for our data, and fit obtained in Ref. [18] are plotted in Fig. 9. Horvat et al. [18] fitted the universal variable X_n for different p_L values and there the emphasis was on the region $X_n > 2$, whereas in this work the emphasis is on the region $X_n < 2$. The geometrical model works also in this region, and the difference between the best fit to our data, and fit obtained by Horvat et al. is fairly small (Fig. 9).

The different X-ray satellite line fractions for $^{12}C^{2+/3+}$ beam measurements are plotted in Figure 10. When the energy (and the universal variable X_n) increases from 4.4 MeV to 6.8 MeV, the KαL^2 and KαL^3 fractions increase, the KαL^1 fraction stays constant and the KαL^0 fraction decreases. For the different Ti-containing samples KαL^1, and KαL^3 fraction are very similar, whereas the biggest difference is seen in KαL^0, and KαL^2 fractions. For the purpose of chemical speciation, the Kα L^0/KαL^2-ratio, and p_L would be the most sensitive parameters to differentiate Ti from TiN and TiO_2. The fitted slope of the KαL^0/KαL^2-ratio is different for TiN and TiO_2, indicating that their separation would become larger at higher beam energies.

To further analyze the distribution we have fitted a binomial distribution as defined in equation (8) to the measured X-ray satellite intensity distribution. Binomial distribution has been used before to fit S Kα structure [14], for example, but it did not agree well with previous measurements because L-shell vacancy filling was not taken into account, and fluorescence yield was assumed to be constant for an atom with different amount of L-shell vacancies. We have expanded the model [14] to include the L-shell vacancy filling. For simplicity and due to the lack of experimental data the fluorescence yield is assumed to not depend on the number of L-shell vacancies. Equation (8) was fitted to the 6.8 MeV $^{12}C^{3+}$ Kα X-ray satellite structure, with the results shown in Figure 11. Even with the improved model, the fit is not satisfactory. The best fit was achieved when the variable P_f (probability for L-shell vacancy filling prior to X-ray emission) was zero. Because the addition of L-shell filling did not improve our model, we would need a more advanced model to fit the distribution better. In a case of fluorine compounds, molecular orbital (MO) calculations

have been shown to explain the experimental results well [35]. In the case of fluorine compounds the valence electrons (2p electrons) of fluorine are directly involved in the X-ray transition and form MOs, but for titanium the electrons directly involved in the X-ray transitions (1s, 2s, 2p) do not form MOs, and MO calculations are not relevant in our case.

The positions and intensities of Ti K$\beta_{2,5}$ and Ti Kβ'' lines relative to the K$\beta_{1,3}$ line have been used to demonstrate chemical speciation in proton measurements [20]. In our measurements, the statistics in the Kβ structure was not good enough to make a decent fit for ions other than $^7Li^{2+}$. In the case of the $^7Li^{2+}$ beam, the KβL fractions are plotted in Figure 8. It can be noted that KβL^0/KβL^1 ratio is higher with TiO_2 compared to the TiN and Ti. However, uncertainties in the Kβ fractions are rather large.

The positions of the satellite lines relative to the KαL^0 are given in Figure 12. Within the measurement uncertainty, peak positions do not change with different beam energies. The measured peak positions were compared to a empirical formula by Wang et al. [36]. The agreement between our measurements and the used formula is not satisfactory in the case of Ti Kα X-ray satellites.

6. Conclusions

In this study, we measured X-ray emission spectra of three different titanium-containing thin films with different ions and with different $^{12}C^{3+}$ beam energies. We observed a difference in the Kα X-ray satellite structure for different chemical environments, even though no chemically-important valence electrons are directly involved in the X-ray emission. Differences in relative Kα X-ray satellite intensities were observed between metal-Ti and TiO_2, but no difference between TiN and TiO_2 were observed. The change between metal-Ti and TiN/TiO_2 is explained by the interatomic transitions from valence electrons of nitrogen and oxygen. With both TiN and TiO_2, the average valence electron density is roughly twice as high as for metallic Ti. Thus, there are more free electrons available after the collision, and they can fill the ionized shell prior to the X-ray emission leading to a different X-ray satellite structure. The most sensitive parameters for chemical speciation were KαL^0/KαL^2-ratio and the p_L value, which can be used to differentiate Ti from TiN and TiO_2. The proportionality of the KαL^0/LαL^2-ratio as a function of beam energy was observed to be different for TiN and TiO_2. Thus, measurements at higher beam energies than performed in this study could result in higher sensitivity to the chemical environment of titanium. Previously it has also been demonstrated that TiN and TiO_2 can be distinguished using a proton beam [20, 21]. By combining high-resolution heavy-ion and proton PIXE, Ti, TiN, and TiO_2 can all be distinguished from each other.

The geometrical model (GM) was used to study the average L-shell ionization fraction at the time of Kα emission. The general trend could be predicted using GM, but there were small deviations from the trend, most notable with the 6.8 MeV $^{16}O^{3+}$ beam measurement.

The use of heavy ions can potentially be beneficial, with the possibility to obtain information on the chemical environment, with higher cross-sections in some cases [37] and with the possibility for simultaneous heavy-ion elastic recoil detection analysis or MeV-SIMS, for example. There are also clear drawbacks with heavy ions. The X-ray production cross-sections of heavy ions are not as well-known as proton cross-sections, hindering usability of heavy ions on quantitative elemental analysis, and heavy ions can not be used for measurements outside the vacuum like protons. The chemical speciation with heavy ion measurements is possible, at least in some cases. We demonstrated that the Ti Kα X-ray satellite structure changes with different $^{12}C^{3+}$ energies. Thus, not only the chemical environment but also the depth distribution of the chemical compound affects the X-ray satellite structure, complicating the analysis for samples where the energy loss of the incident ion is significant.

References

[1] T. B. Johansson, R. Akselsson, and S. A. E. Johansson. X-ray analysis: Elemental trace analysis at the 10^{-12} g level. *Nuclear Instruments and Methods*, 84(1):141–143, 1970.

[2] P Richard, J Bolger, D. K Olsen, and C. F Moore. Molecular structure effects of aluminum $K\beta$ x-ray spectra produced in proton and alpha particle excitation. *Physics Letters A*, 41(3):269–271, 1972.

[3] P. G. Burkhalter, A. R. Knudson, D. J. Nagel, and K. L. Dunning. Chemical Effects on Ion-Excited Aluminum K X-Ray Spectra. *Physical Review A*, 6(6):2093–2101, 1972.

[4] R. L. Watson, A. K. Leeper, B. I. Sonobe, T. Chiao, and F. E. Jenson. Effect of chemical environment on the intensities of $K\alpha$ x-ray satellites produced in heavy-ion collisions. *Physical Review A*, 15(3):914–925, 1977.

[5] J. McWherter, D. K. Olsen, H. H. Wolter, and C. F. Moore. Silicon and silicon dioxide K x-ray spectra from hydrogen, helium, and oxygen bombardment. *Physical Review A*, 10(1):200–208, 1974.

[6] F. Folkmann. Chemical effects in Cr containing samples measured by the KβKα intensity ratio and the Kβ energy shift. *Nuclear Instruments and Methods in Physics Research Section B: Beam Interactions with Materials and Atoms*, 109–110:39–41, 1996.

[7] M. Uda, O. Benka, K. Fuwa, K. Maeda, and Y. Sasa. Chemical effects in PIXE spectra. *Nuclear Instruments and Methods in Physics Research Section B: Beam Interactions with Materials and Atoms*, 22(1):5–12, 1987.

[8] A. Langenberg and R. L. Watson. Study of Mg $K\alpha$ x-ray multiplet structure observed in ion-atom collisions. *Physical Review A*, 23(3):1177–1187, 1981.

[9] J. A. Demarest and R. L. Watson. Ion-excited $K\alpha$ x-ray satellite spectra of Si, S, Cl, and Ar in the gas phase. *Physical Review A*, 17(4):1302–1313, 1978.

[10] R. L. Watson, V. Horvat, and Y. Peng. $K\alpha$ x-ray satellite and hypersatellite spectra of vanadium metal and oxides excited in heavy-ion collisions. *Physical Review A*, 78(6):062702, 2008.

[11] I. Božičević Mihalić, S. Fazinić, T. Tadić, D. Cosic, and M. Jakšić. Study of ion beam induced chemical effects in silicon with a downsized high resolution X-ray spectrometer for use with focused ion beams. *Journal of Analytical Atomic Spectrometry*, 31(11):2293–2304, 2016.

[12] I. Božičević Mihalić, S. Fazinić, and D. Cosic. High resolution K X-ray spectra of selected silicates induced by MeV proton and carbon micro-beams. *Nuclear Instruments and Methods in Physics Research Section B: Beam Interactions with Materials and Atoms*, 417:70–74, 2018.

[13] C. M. Heirwegh, M. Petric, S. Fazinić, M. Kavčič, I. B. Mihalić, J. Schneider, I. Zamboni, and J. L. Campbell. Multiple ionization X-ray satellites of magnesium, aluminum and silicon in alpha particle PIXE. *Nuclear Instruments and Methods in Physics Research Section B: Beam Interactions with Materials and Atoms*, 428:9–16, 2018.

[14] S. Raman and C. R. Vane. Implications of heavy-ion-induced satellite X-ray emission I: Introduction. *Nuclear Instruments and Methods in Physics Research Section B: Beam Interactions with Materials and Atoms*, 3(1–3):71–77, 1984.

[15] F. Folkmann. High resolution ion induced X-ray spectroscopy for chemical state analysis. *Nuclear Instruments and Methods in Physics Research Section B: Beam Interactions with Materials and Atoms*, 75(1):9–13, 1993.

[16] H. Endo and M. Uda. Atomic number dependence of l-shell vacancy rearrangement probabilities on $K\alpha$ X-ray satellites induced by 6 MeV/amu N4+ impacts. *Zeitschrift für Physik A Atoms and Nuclei*, 306(3):187–193, 1982.

[17] K. W. Hill, B. L. Doyle, S. M. Shafroth, D. H. Madison, and R. D. Deslattes. Projectile charge and energy dependence of titanium K x rays and satellites following excitation by fast heavy ions. *Physical Review A*, 13(4):1334–1343, 1976.

[18] V. Horvat, R. L. Watson, and Yong Peng. Systematics of $K\alpha$ x-ray satellite structure. *Physical Review A*, 74(2):022718, 2006.

[19] S. Fukushima, T. Kimura, K. Nishida, V. A. Mihai, H. Yoshikawa, M. Kimura, T. Fujii, H. Oohashi, Y. Ito, and M. Yamashita. The Valence State Analysis of Ti in FeTiO3 by Soft X-Ray Spectroscopy. *Microchimica Acta*, 155(1-2):141–145, 2006.

[20] L. Mandić, S. Fazinić, and M. Jakšić. Chemical effects on the $K\beta''$ and $k\beta_{2,5}$ x-ray lines of titanium and its compounds. *Physical Review A*, 80(4):042519, 2009.

[21] M. R. J. Palosaari, M. Kayhko, K. M. Kinnunen, M. Laitinen, J. Julin, J. Malm, T. Sajavaara, W. B. Doriese, J. Fowler, C. Reintsema, D. Swetz, D. Schmidt, J. N. Ullom, and I. J. Maasilta. Broadband Ultrahigh-Resolution Spectroscopy of Particle-Induced X Rays: Extending the Limits of Nondestructive Analysis. *Physical Review Applied*, 6(2):024002, 2016.

[22] M. R. J. Palosaari, K. M. Kinnunen, J. Julin, M. Laitinen, M. Napari, T. Sajavaara, W. B. Doriese, J. Fowler, C. Reintsema, D. Swetz, D. Schmidt, J. Ullom, and I. J. Maasilta. Transition-Edge Sensors for Particle Induced X-ray Emission Measurements. *Journal of Low Temperature Physics*, 176(3-4):285–290, 2013.

[23] M. Laitinen, M. Rossi, J. Julin, and T. Sajavaara. Time-of-flight – Energy spectrometer for elemental depth profiling – Jyvaskyla design. *Nuclear Instruments and Methods in Physics Research Section B: Beam Interactions with Materials and Atoms*, 337:55–61, 2014.

[24] A. C. Scafes, C. Ciortea, D. E. Dumitriu, A. Enulescu, D. Fluerasu, M. M. Gugiu, M. D. Pena, M. Pentia, and I. Pitic. K-shell ionization cross sections of Ti, Cr, Ni, Cu, and Zr in collisions with ^{16}O ions at mev/u energies. *Romanian Reports in Physics*, 66(2):455–471, 2014.

[25] Y. C. Yu, C. W. Wang, and E. K. Lin. Lithium-7 ion induced K X-ray production cross sections of Ti, Cu, Se, and Ag in the energy range 3.0—10.0 MeV. *Nuclear Instruments and Methods in Physics Research Section B: Beam Interactions with Materials and Atoms*, 79(1–4):199–202, 1993.

[26] S. J. Cipolla. ISICS2008: An expanded version of ISICS for calculating K-, L-, and M-shell cross sections from PWBA and ECPSSR theory. *Computer Physics Communications*, 180(9):1716–1717, 2009.

[27] B. K. Alpert, R. D. Horansky, D. A. Bennett, W. B. Doriese, J. W. Fowler, A. S. Hoover, M. W. Rabin, and J. N. Ullom. Filters for High Rate Pulse Processing. *arXiv:1212.1738*, 2012.

[28] M. Wojdyr. *Fityk* : a general-purpose peak fitting program. *Journal of Applied Crystallography*, 43(5):1126–1128, 2010.

[29] D. Yan, R. Divan, L. M. Gades, P. Kenesei, T. J. Madden, A. Miceli, J.-S. Park, U. M. Patel, O. Quaranta, H. Sharma, D. A. Bennett, W. B. Doriese, J. W. Fowler, J. D. Gard, J. P. Hays-Wehle, K. M. Morgan, D. R. Schmidt, D. S. Swetz, and J. N. Ullom. Eliminating the non-Gaussian spectral response of X-ray absorbers for transition-edge sensors. *Applied Physics Letters*, 111(19):192602, 2017.

[30] B. Sulik, I. Kádár, S. Ricz, D. Varga, J. Végh, G. Hock, and D. Berényi. A simple theoretical approach to multiple ionization and its application for 5.1 and 5.5 MeV/u X^{q++} Ne collisions. *Nuclear Instruments and Methods in Physics Research Section B: Beam Interactions with Materials and Atoms*, 28(4):509–518, 1987.

[31] J. H. McGuire and P. Richard. Procedure for Computing Cross Sections for Single and Multiple Ionization of Atoms in the Binary-Encounter Approximation by the Impact of Heavy Charged Particles. *Physical Review A*, 8(3):1374–1384, 1973.

[32] R. D. Deslattes, E. G. Kessler, P. Indelicato, L. de Billy, E. Lindroth, and J. Anton. X-ray transition energies: new approach to a comprehensive evaluation. *Reviews of Modern Physics*, 75(1):35–99, 2003.

[33] J. W. Fowler, B. K. Alpert, W. B. Doriese, Y.-I. Joe, G. C. O'Neil, J. N. Ullom, and D. S. Swetz. The Practice of Pulse Processing. *Journal of Low Temperature Physics*, 2015. arXiv: 1511.03950.

[34] M. Käyhkö, M. R. J. Palosaari, M. Laitinen, K. Arstila, I. J. Maasilta, J. W. Fowler, W. B. Doriese, J. N. Ullom, and T. Sajavaara. Minimum detection limits and applications of proton and helium induced X-ray emission using transition-edge sensor array. *Nuclear Instruments and Methods in Physics Research Section B: Beam Interactions with Materials and Atoms*, 406:130–134, 2017.

[35] U. Uda. Extended analysis of satellite structures in particle induced X-ray emission spectra using molecular orbital calculations. *Advances in Quantum Chemistry*, 37:31–55, 2000.

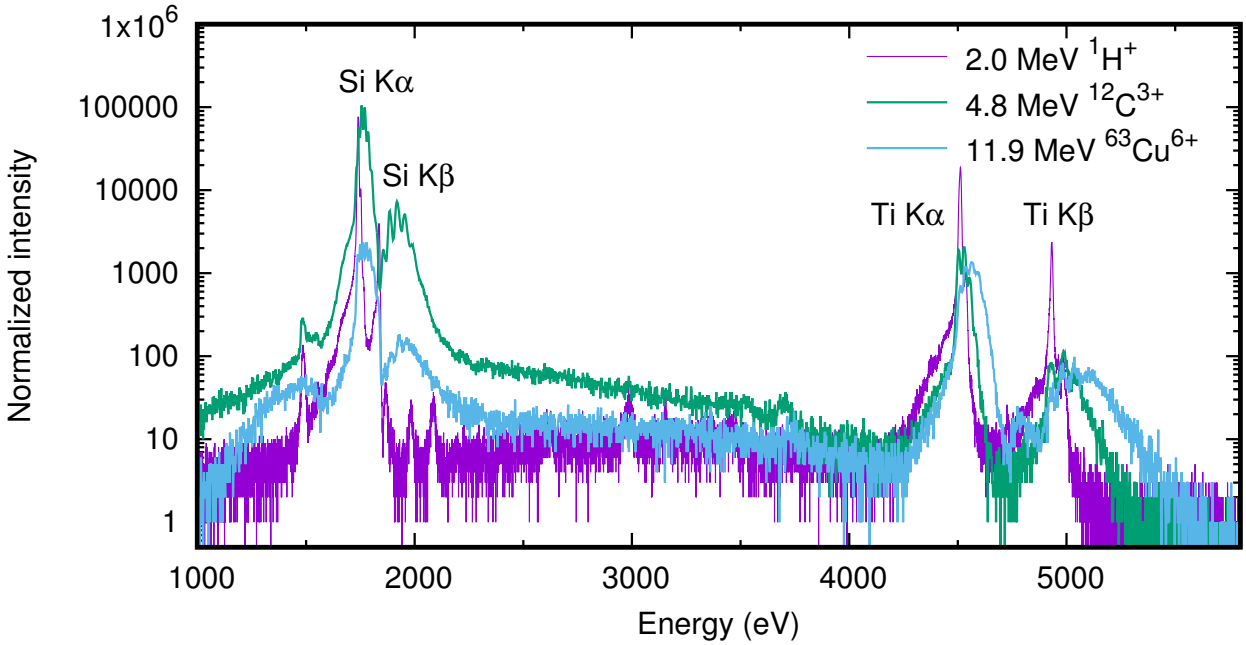

Figure 1: Spectra of a 50 nm thick Ti film on top of a Si substrate measured with 4.8 MeV $^{12}C^{3+}$ and 11.9 MeV $^{63}Cu^{6+}$ beams, and a spectrum of a 400 nm thick Ti film on top of a Si substrate measured with a 2.0 MeV $^{1}H^{+}$ beam. Note logarithmic intensity scale.

[36] Xiang-Li Wang, Chen-Zhong Dong, and Mao-Gen Su. Energy shifts of kα,β,γ x-ray satellites for atoms with $13 \leq z \leq 90$: A systematic calculation and a new analytical description. *Nuclear Instruments and Methods in Physics Research Section B: Beam Interactions with Materials and Atoms*, 280:93–97, 2012.

[37] Klas G. Malmqvist Sven A. E. Johansson, John L. Campbell. *Particle-Induced X-Ray Emission Spectrometry (PIXE)*. A Wiley-Interscience Publication, New York, 1995.

[38] J. F. Ziegler, M. D. Ziegler, and J. P. Biersack. SRIM – The stopping and range of ions in matter (2010). *Nuclear Instruments and Methods in Physics Research Section B: Beam Interactions with Materials and Atoms*, 268(11–12):1818–1823, 2010.

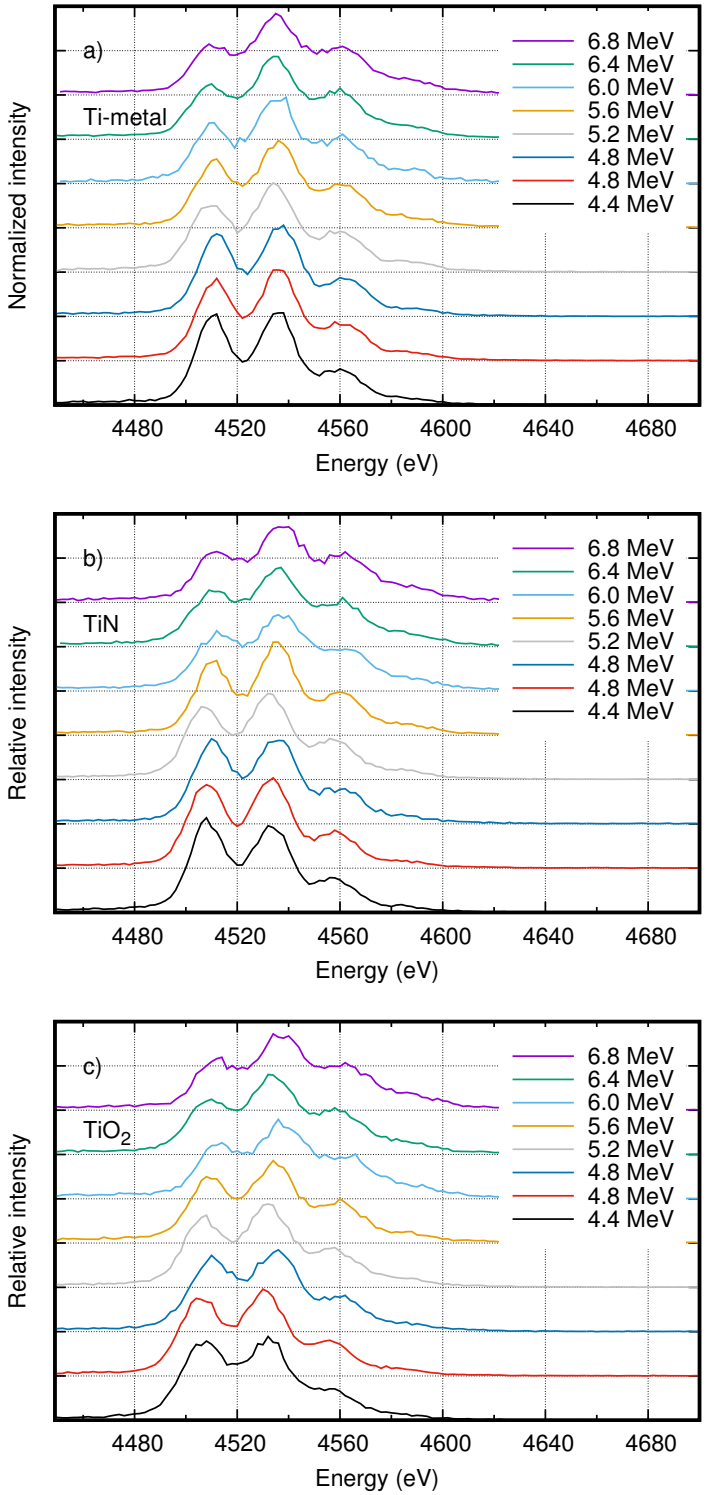

Figure 2: Measured Ti K_α X-ray satellite lines of a) Ti-metal, b) TiN and c) TiO_2 samples using $^{12}C^{3+}$ beams with energies ranging from 4.4 MeV to 6.8 MeV, and 4.8 MeV $^{12}C^{2+}$ beam (red line, 2nd from bottom). With increasing energy, intensity distribution changes.

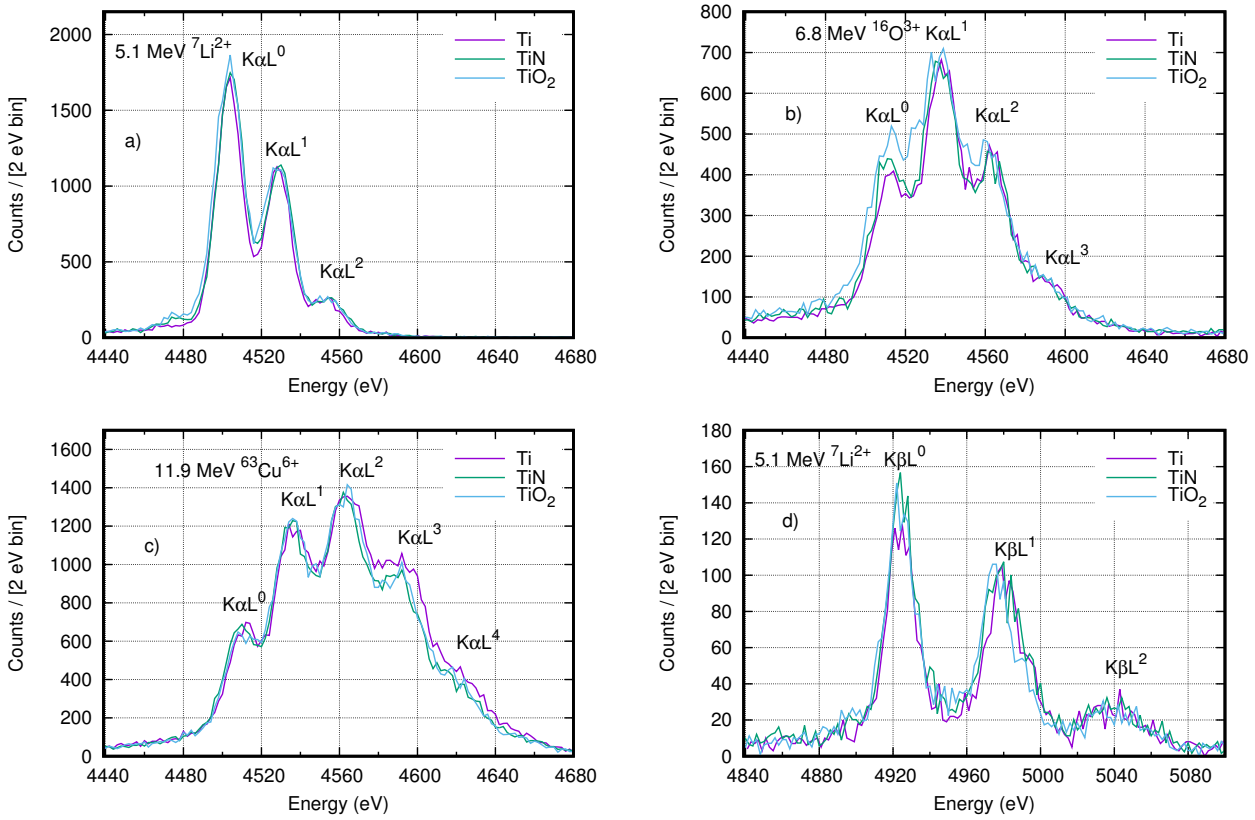

Figure 3: Measured Ti K_α X-ray satellite lines of Ti, TiN and TiO_2 samples using a) 5.1 MeV $^7Li^{2+}$, b) 6.8 MeV $^{16}O^{3+}$ and c) 11.9 MeV $^{63}Cu^{6+}$ beams, and d) Ti K_β X-ray satellite lines of Ti, TiN and TiO_2 samples using a 5.1 MeV $^7Li^{2+}$ beam. Intensity is scaled against the highest fitted satellite peak height, and the Ti sample spectra are unscaled in all cases.

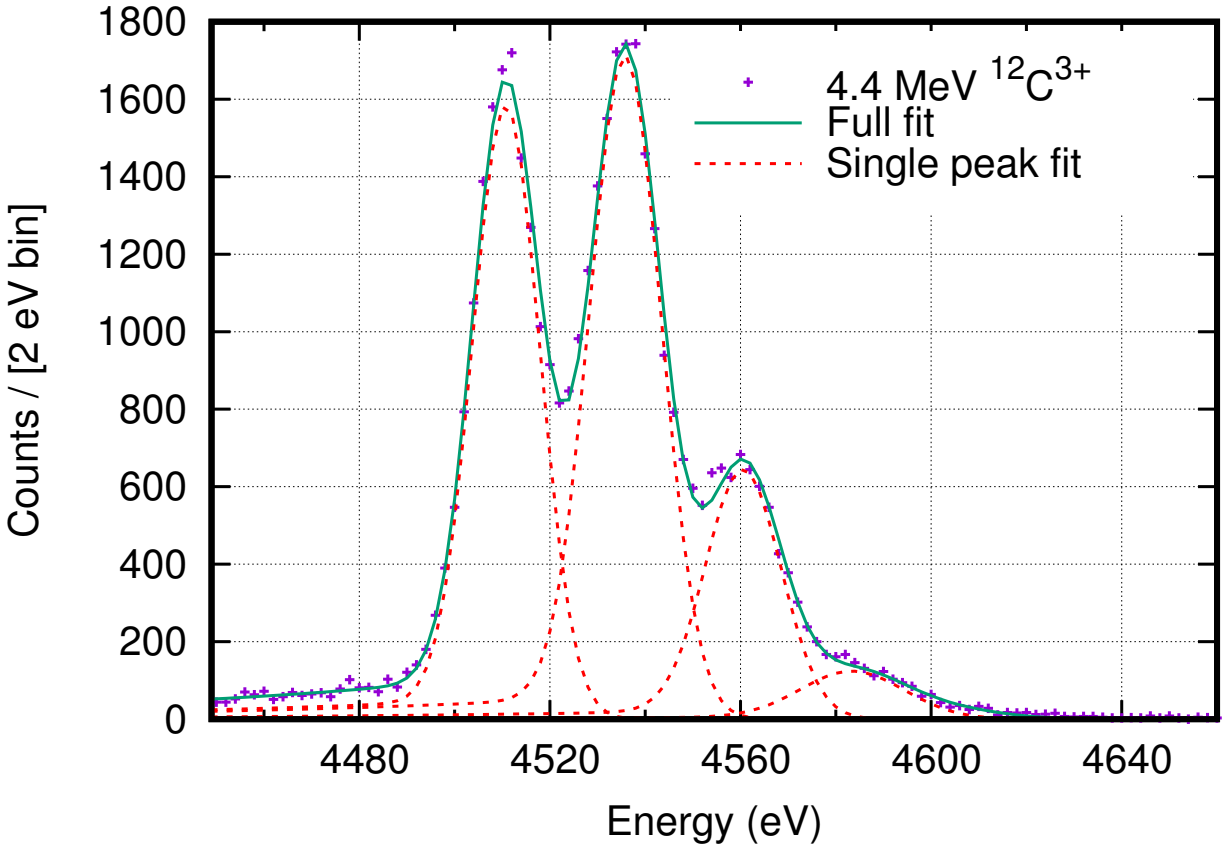

Figure 4: Fitted multiple-ionization satellite structure for a 50 nm thick Ti film measured using a 6.4 MeV $^{12}C^{3+}$ beam. The peaks are fitted using Voigt profile with a fixed Gaussian width (detector resolution, 6 eV), and freely varying Lorentzian width. An exponential tail originating from the detector [29] is included in the fit.

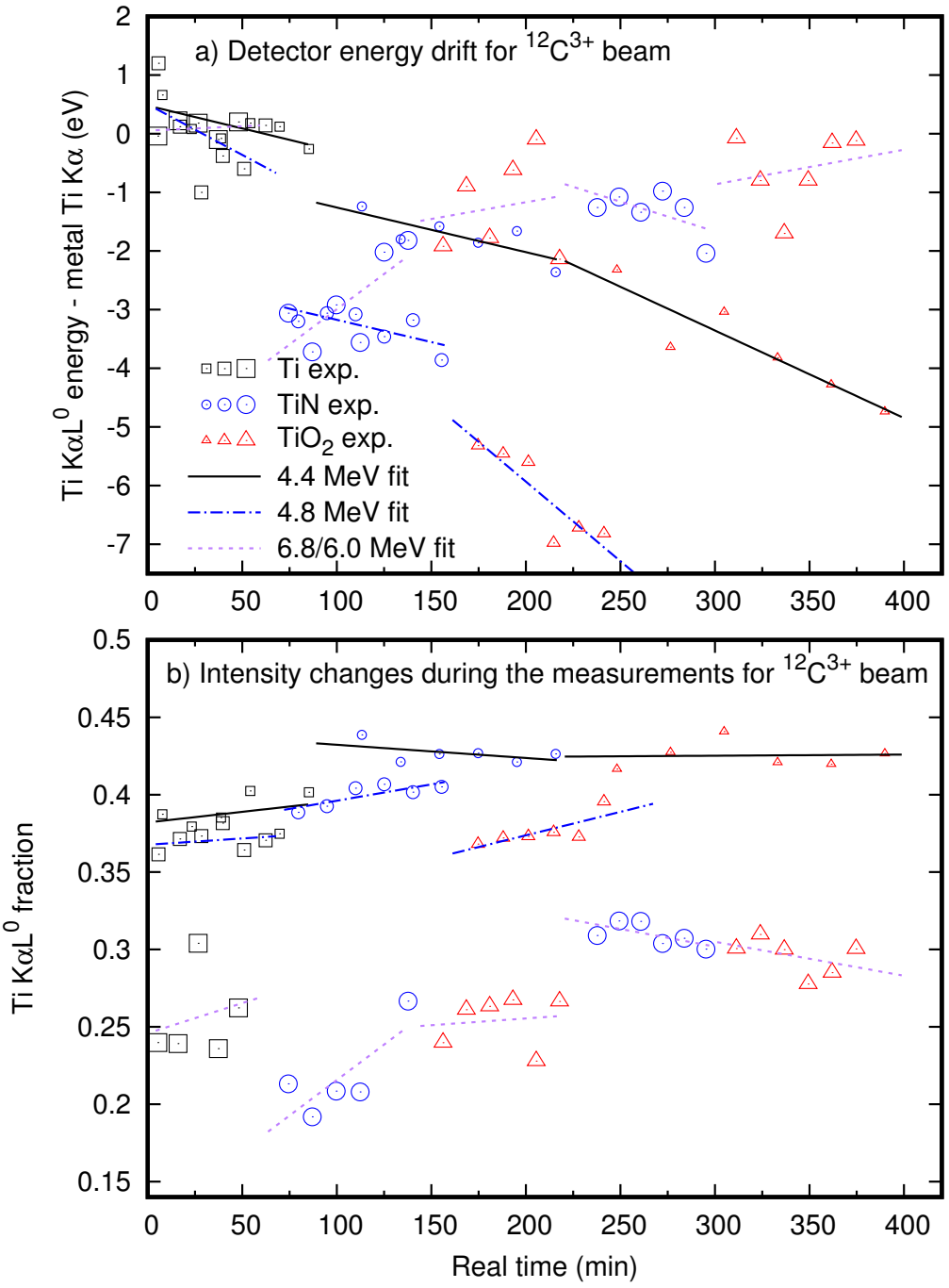

Figure 5: List mode analysis of a) relative Ti KαL^0 position, and b) Ti KαL^0 fraction from three measurement days to monitor the possible changes of the sample and detector stability during the measurements. The peak positions for Ti KαL^0 line and KαL^0 fractions for different Ti-containing samples were measured using 4.4 MeV (small symbols), 4.8 MeV (medium-size symbols), 6.0 MeV (large symbols), and 6.8 MeV (large symbols) $^{12}C^{3+}$ beams (same symbols are used both in figure a) and b)). Solid lines are fits to the data points of each sample, and the line style represents a measurement from the same day (real time starts from zero for each day). For the dashed line, first three measurements were carried out with a 6.8 MeV $^{12}C^{3+}$ beam, and final two with a 6.0 MeV $^{12}C^{3+}$ beam. Uncertainties for peak positions are 0.3–0.9 eV, and uncertainties for Ti KαL^0 fractions are 0.013–0.02. Uncertainties are omitted from the plot for clarity.

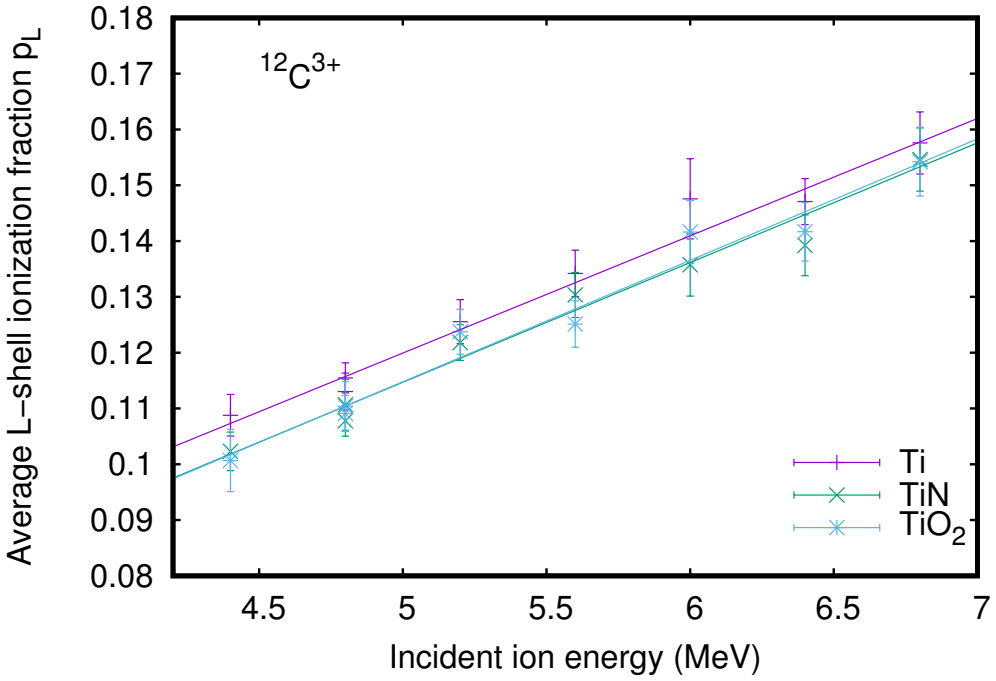

Figure 6: Measured apparent average L-shell ionization p_L during X-ray emission as a function of energy for $^{12}C^{2+/3+}$ ions. The higher the value the more ionized L-shell for titanium. All samples had a thickness of circa 50 nm and energy losses in the films were roughly 0.15 MeV in all cases (calculated with SRIM-2013 [38]).

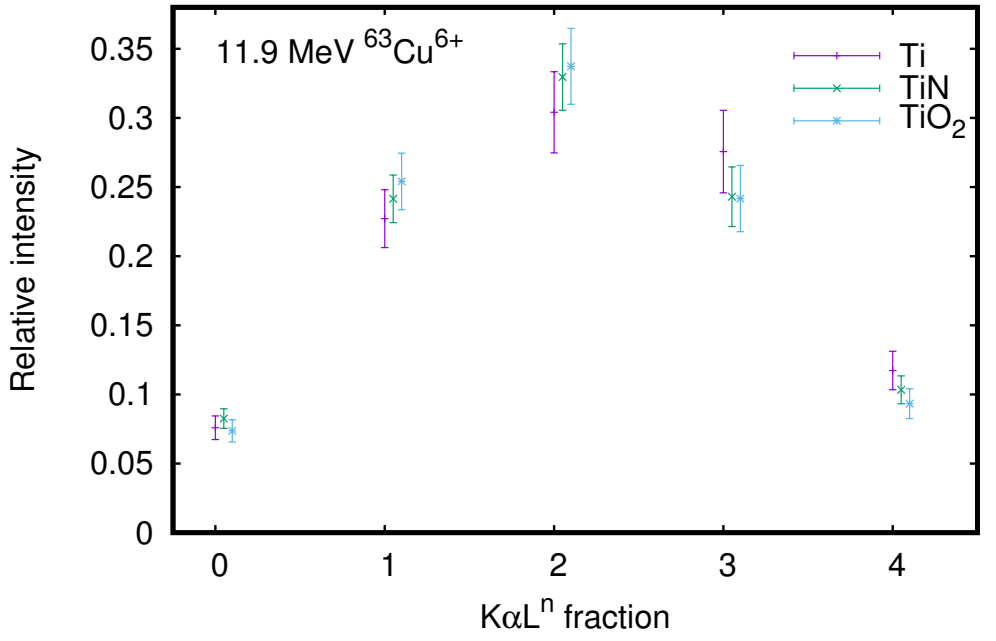

Figure 7: Measured multiple ionization satellite intensities for a 11.9 MeV $^{63}Cu^{6+}$ beam. Points for TiN, and TiO_2 samples are slightly shifted for clarity. Peaks were fitted with the Voigtian peak with an exponential tail. The Gaussian width, corresponding to instrumental resolution, was a constant 6 eV and was fitted using a calibration measurement carried out with a proton beam. All samples had a thickness of circa 50 nm and energy losses in the films were roughly 0.45–0.55 MeV in all cases (calculated with SRIM-2013 [38]).

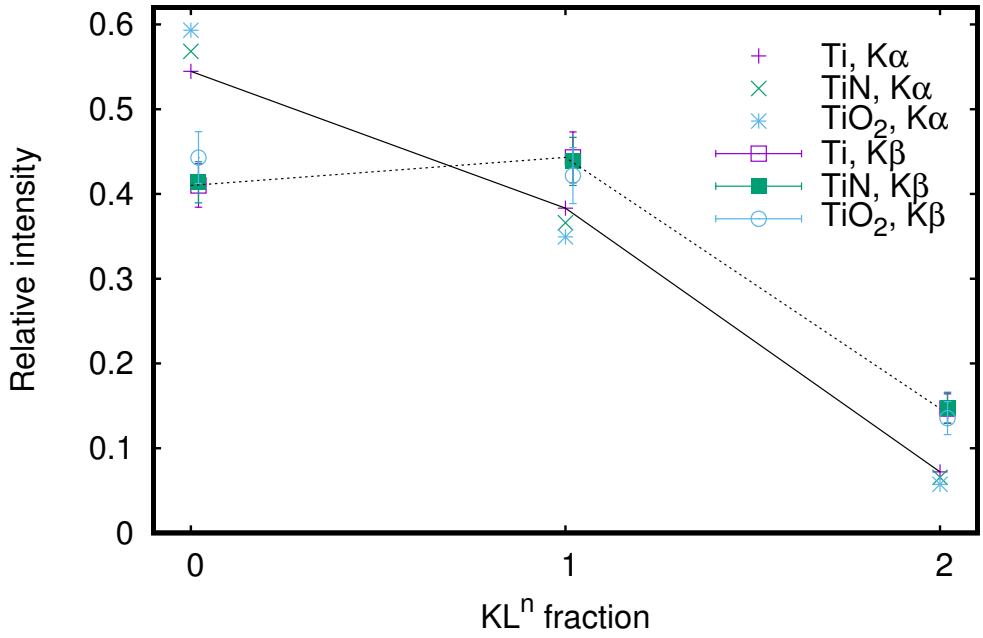

Figure 8: Measured multiple ionization satellite intensities for a 5.1 MeV $^7Li^{2+}$ beam. Uncertainties for KαL^0 and KαL^1 are 2–4% and 7–9% for KαL^2. Kβ fractions are shifted slightly for clarity. Peaks were fitted with the Voigtian peak with an exponential tail. The Gaussian width, corresponding to instrumental resolution, was a constant 6 eV and was fitted using a calibration measurement carried out with a proton beam. All samples had a thickness of circa 50 nm and energy losses in the films were between 50 and 60 keV (calculated with SRIM-2013 [38]). Lines are drawn between the Ti Kα and Ti Kβ fraction data points from Ti sample measurements to guide the eye.

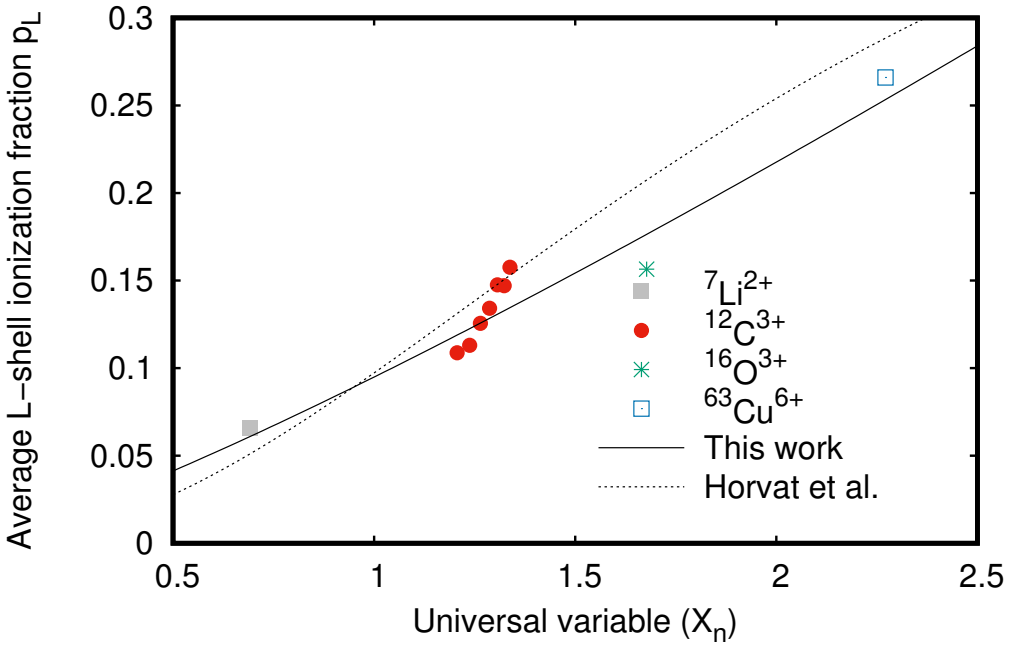

Figure 9: Measured apparent average L-shell ionization p_L at the time of Kα emission as a function of the universal variable X_n (Eq. (2)). X_n is a function of projectile energy, average speed of the L-shell electron in target atom, projectile atomic number, and binary encounter approximation function, which describes scaling of ionization cross-section. The average energy of the incident ion was used in the calculations and the energy loss was calculated using SRIM-2013 [38]. Fit to Eq. (4) were made for our data points and the previous fit made by Horvat et al. [18] is plotted as well.

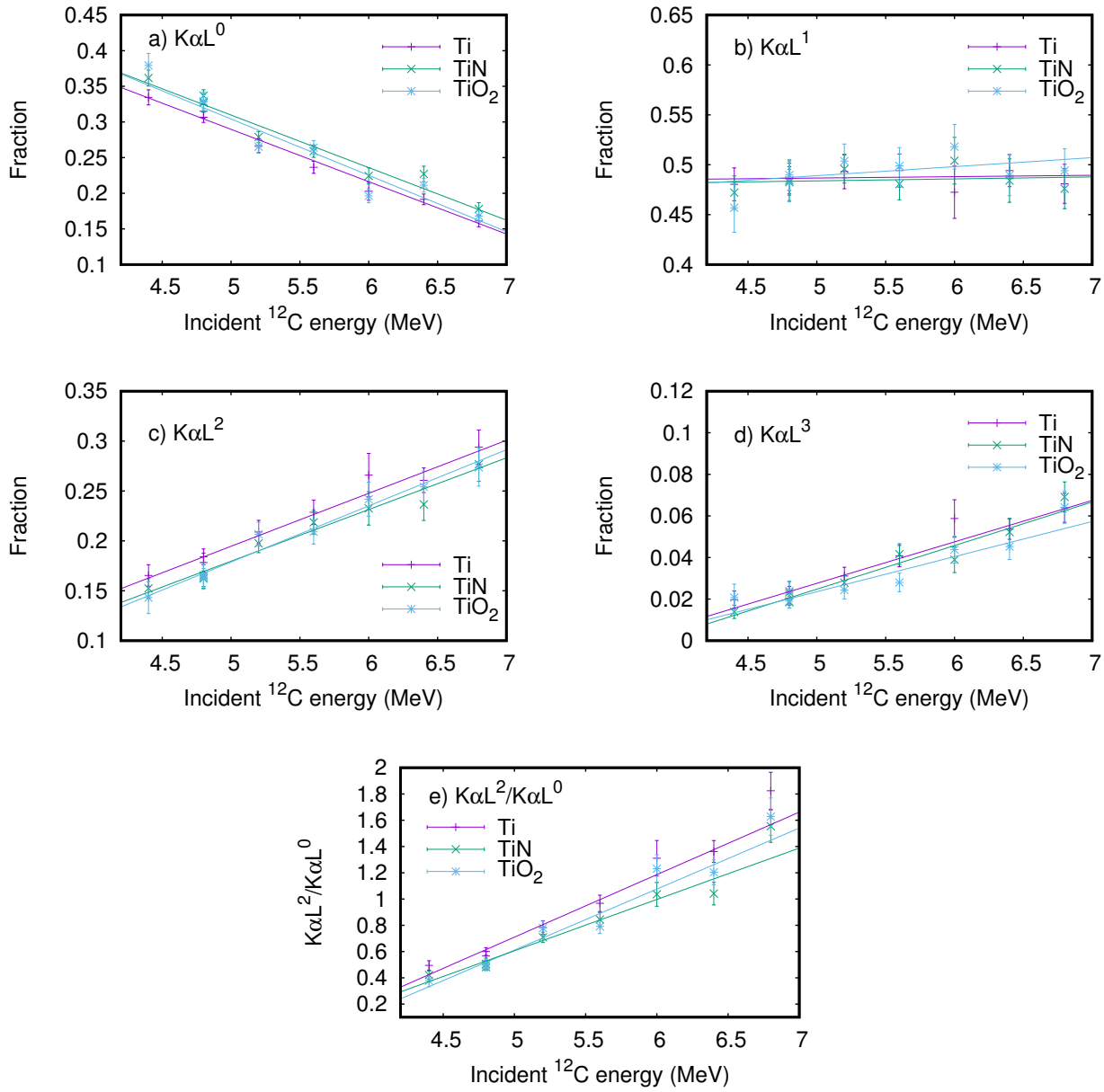

Figure 10: Measured a) $K\alpha L^0$, b) $K\alpha L^1$, c) $K\alpha L^2$, d) $K\alpha L^3$, e) $K\alpha L^2/K\alpha L^0$ fractions as a function of energy for $^{12}C^{2+/3+}$ ions. Peaks were fitted with the Voigtian peak with an exponential tail. The Gaussian width, corresponding to instrumental resolution, was a constant 6 eV and was fitted using a calibration measurement carried out with a proton beam. All samples had a thickness of circa 50 nm and energy losses in the films were roughly 0.15 MeV in all cases (calculated with SRIM-2013 [38]).

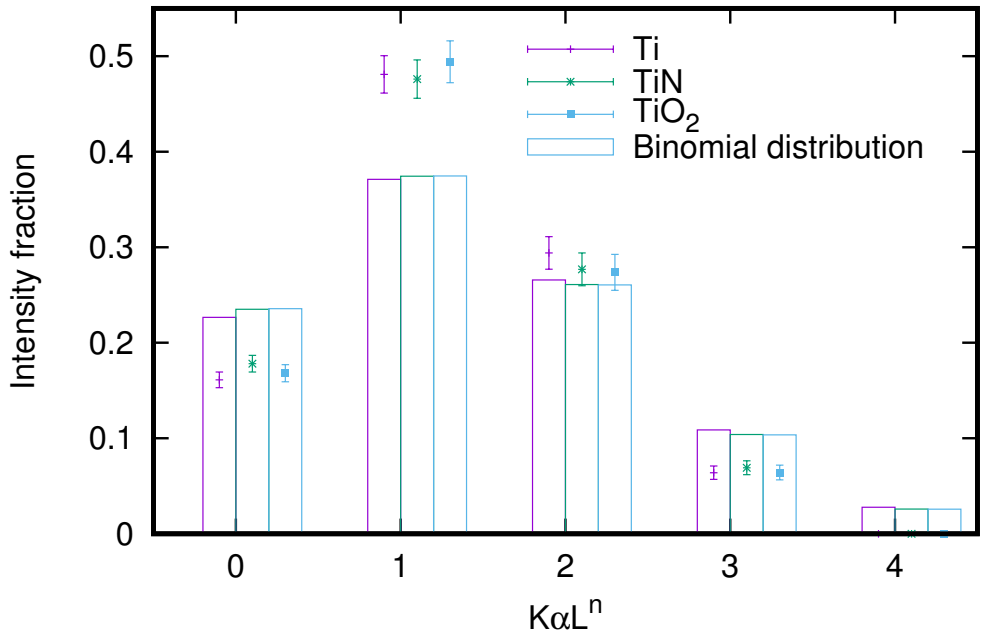

Figure 11: The intensity distribution of Ti Kα satellite lines measured using a 6.8 MeV $^{12}C^{3+}$ beam. The intensity distribution is fitted using a binomial distribution according to equation (8). The difference between experimental data and the binomial fit is clear, and this model cannot explain the multiple ionization X-ray satellite structure.

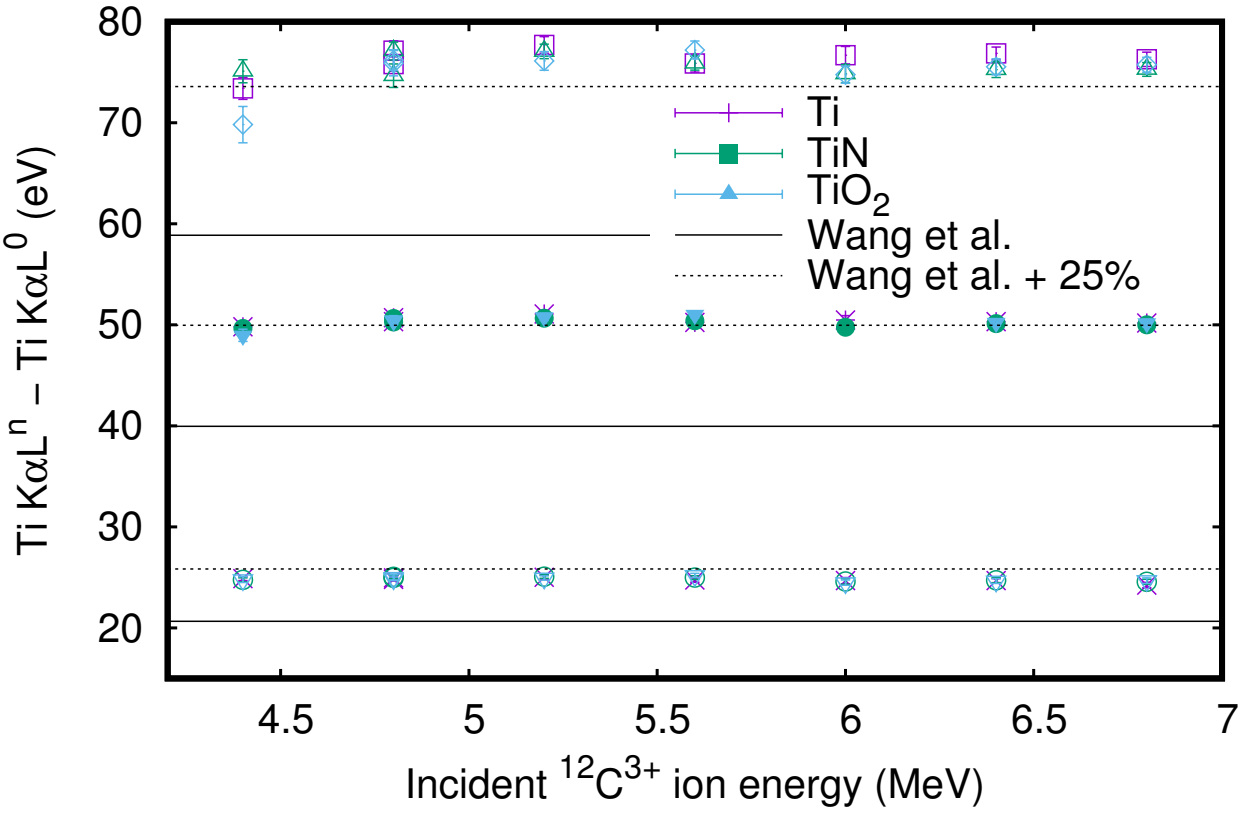

Figure 12: Peak positions of Ti KαL^1, Ti KαL^2, and Ti KαL^3 multiple ionization satellite peaks for all $^{12}C^{3+}$ beam measurements. The multiple ionization satellite peaks are measured relative to the single ionized peak of the same sample. The experimental values are compared to an empirical formula fitted by Wang et al. [36].

PIV

A NEW BEAMLINE FOR ENERGY-DISPERSIVE HIGH-RESOLUTION PIXE ANALYSIS USING POLYCAPILLARY OPTICS

by

M. Käyhkö, M. Laitinen, K. Arstila, I. J. Maasilta, T. Sajavaara

Submitted to Nucl. Inst. Meth. B

A new beamline for energy-dispersive high-resolution PIXE analysis using polycapillary optics

M. Käyhkö[a], M. Laitinen[a], K. Arstila[a], I. J. Maasilta[c], T. Sajavaara[a]

[a] *University of Jyvaskyla, Department of Physics, Postal address: P.O. Box 35, Postal code: FI-40014, City (postal office): University of Jyvaskyla, Finland*
[b] *National Institute of Standards and Technology, 325 Broadway, Boulder, CO 80305, USA*
[c] *University of Jyvaskyla, Department of Physics, Nanoscience Center, Postal address: P.O. Box 35, Postal code: FI-40014, City (postal office): University of Jyvaskyla, Finland*

Abstract

A new beamline for high energy resolution PIXE measurements is presented. This new setup includes options for both in-air and vacuum measurements. For the high energy resolution transition-edge sensor array, a polycapillary lens is used for detecting low-energy X-rays down to 0.5 keV and to increase the effective solid angle. X-ray transmission of the polycapillary lens was characterized using two calibration standards. The gain obtained by adding a polycapillary lens was 1.6–2.3 at energies between 2.1 keV and 4.5 keV. From 1.04 to 1.74 keV the gain is increased to 2.1–3.0, and at energies 4.9–8.0 keV the gain is between 1.6–0.65. The measured gain agreed well with theoretical calculations. The lightest detectable element in the new setup is oxygen at 0.525 keV.

Keywords: External-PIXE, PIXE, Transition-edge sensor, Polycapillary lens

1. Introduction

Particle-induced X-ray emission, PIXE, is a quantitative method for elemental analysis [1]. In PIXE, an energetic ion beam is used to excite inner-shell electrons, an outer-shell electron fills the produced electron hole, and a photon is emitted and detected. With PIXE, carbon and heavier elements can be detected [2] but work is mostly limited to sodium and heavier because the self-absorption is very high for X-ray energies below 1 keV.

One of the most attractive features of PIXE is the ability to perform measurements in an atmospheric pressure (known as external beam PIXE or in-air PIXE), and that the technique is delicate enough to measure precious items like museum artifacts [2]. High energy resolution detectors such as wavelength-dispersive detectors have been used with an external beam in some studies [3, 4, 5, 6], but this far microcalorimeter detectors have been operated only in a vacuum in conjunction with PIXE [7, 8, 9, 10, 11, 12, 13, 14].

High energy resolution PIXE has many advantages over conventional PIXE. The separation of peaks of complicated samples with many different elements is easier, and the minimum detection limit has been demonstrated to improve by many orders of magnitude up to a factor of 680 [9]. High energy resolution PIXE can be used for chemical speciation in many instances, like for different Ti compounds [8, 15] and S compounds [16]. Chemical speciation of light elements, like O, F, or Na, is a subject of interest, and maintaining a good X-ray detection efficiency at energies below 1 keV is desirable.

In PIXE, the detection of lighter elements (C, N, O, Na, etc.) is possible if one can filter out the detector-damaging, scattered particle beam without sacrificing X-ray transmission to the detector. This can be achieved either by using a bending magnet in combination with external beam [2] or a polycapillary lens [17]. Transition-edge sensor (TES) microcalorimeters are sensitive to external magnetic fields [18, 19] making the polycapillary lens a more appealing option for this type of a detector, and it has previously been integrated with many other TES applications [20, 21, 22, 23, 24] but not PIXE. A polycapillary lens consists of thousands of small capillaries with a diameter of a few micrometers [25]. X-rays travel through capillaries via total external reflection, somewhat similar to an optical fiber cable, and by slightly bending the capillaries X-rays can be focused [25]. Energetic ions, on the other hand, are not reflected but will stop at the lens and do not reach the detector [17]. Due to the X-ray focusing effect of the polycapillary lens, the X-ray detector can be further away from the sample and still have a high absolute efficiency.

Email address: majukayh@gmail.com (M. Käyhkö)

In this work, we have developed an energy-dispersive, high energy resolution PIXE setup at atmospheric pressure for X-ray energies between 0.5 keV and 10 keV using TES microcalorimeters. This opens up a possibility to study, for example, art, archaeological samples, aerosol samples and other delicate samples not suitable for vacuum.

2. Theoretical background

2.1. Theoretical X-ray transmission through a polycapillary lens

A polycapillary lens consists of thousands of hollow capillaries with a diameter of a few micrometers. A polycapillary lens is based on the total external reflection of X-rays. A common capillary material is a borosilicate glass for which the critical angle can be approximated using equation [25]

$$\theta_c = \frac{0.030}{E}, \tag{1}$$

where θ_c is in radians when energy E is given in keV. The critical angle is slightly different with other glass types, like leaded glass. The X-ray reflection below the critical angle is below 100% due to the X-ray absorption. The reflectivity of X-rays, where this absorption is taken into account is reported in [26]. Using that data, the reflectivity of thick borosilicate glass at three different angles, 0.25, 0.5, and 1 degrees, is plotted in Fig. 1. The absorption edges of the two main components (O and Si) cause a sudden increase in X-ray absorption, which decreases X-ray reflectivity.

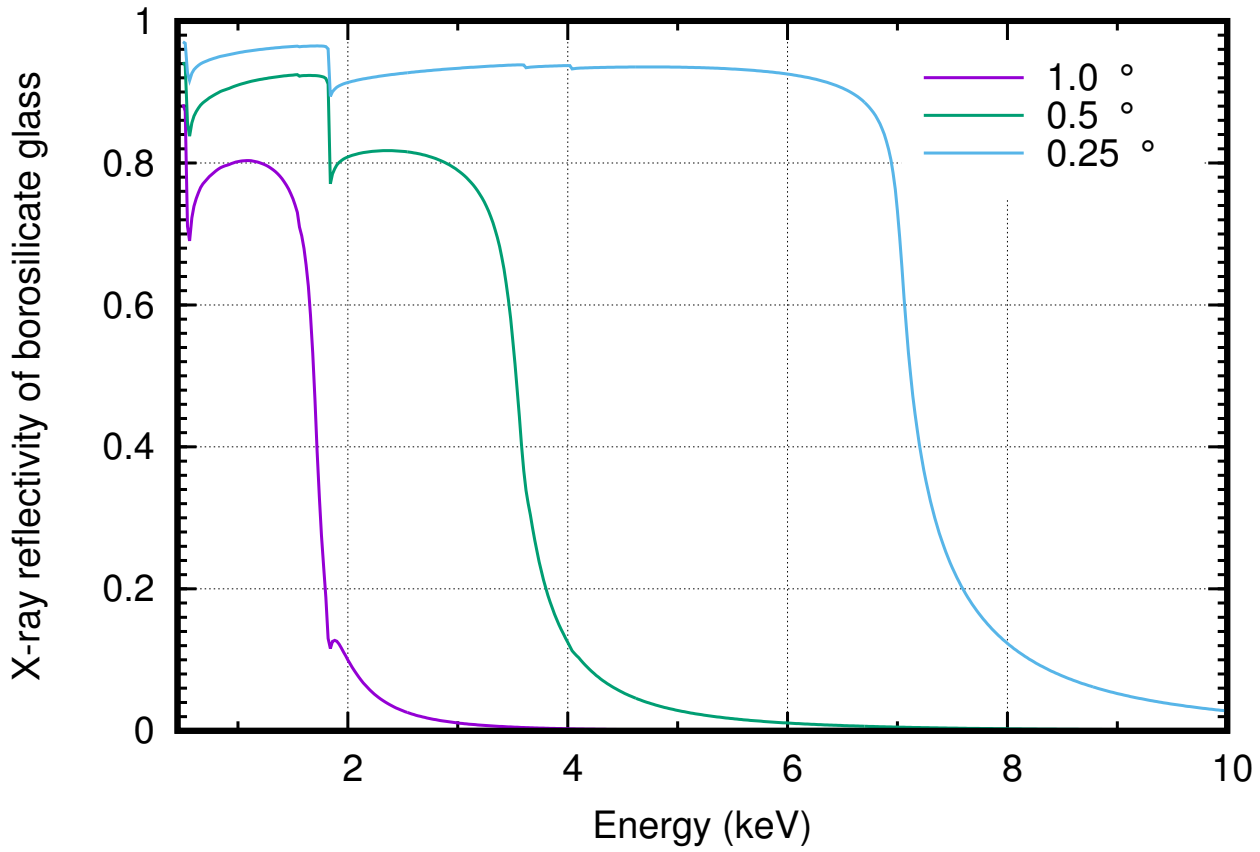

Figure 1: Reflectivity of X-rays for borosilicate glass at 0.25, 0.5, and 1.0 degrees [26]. Sharp transitions are due to the X-ray absorption edges of Si and O.

The gain of the polycapillary lens for the finite size spot can be calculated as

$$G\left(E\right) = \frac{\Omega_{lens}}{\Omega_{nolens}} \cdot \epsilon\left(E\right), \tag{2}$$

where G is the gain, E the X-ray energy, Ω_{lens} the solid angle of the polycapillary lens (input side), Ω_{nolens} the solid angle of the detector, and ϵ the transmittance of the polycapillary lens integrated over the X-ray spot. The

transmittance can be approximated as

$$\epsilon\left(E\right)=A_f\frac{\int_0^\infty \mathrm{d}r_{spot}\int_0^{2\pi}\mathrm{d}\theta\int_0^{R_{in}}\mathrm{d}r_{in}\cdot\alpha\cdot P^n\left(E,\phi\right)}{\int_0^\infty \mathrm{d}r_{spot}\int_0^{2\pi}\mathrm{d}\theta\int_0^{R_{in}}\mathrm{d}r_{in}\cdot\alpha}, \tag{3}$$

where A_f is the active area fraction of the lens (the cross-sectional area of the capillary holes divided by the cross-sectional lens area), r_{spot} the distance of the emitted X-ray from the center of the X-ray spot, P the X-ray reflectivity, ϕ the reflection angle, n the number of reflections in the capillary, and r_{in} the distance of a capillary from the lens center (input side). The parameters describing a property of a single capillary are marked with small letters, and large letters describe the macroscopic polycapillary lens (e.g. $0 \leq r_{in} \leq R_{in} = D_{in}/2$). The parameter α is used to simplify the equation and it is defined as

$$\alpha = f_y\left(r_{spot}\sin\left(\theta\right)\right) f_x\left(r_{spot}\cos\left(\theta\right)\right) r_{spot} r_{in}, \tag{4}$$

where f_x and f_y are the intensity distribution of the X-ray spot in x- and y-axis (perpendicular to the sample surface), θ is the angle of the emitted X-ray relative to the center of the X-ray spot in radial coordinates. The number of reflections is calculated as

$$n = \max\left(1;\lfloor {}^{L}/_{\lambda_1}\rfloor;\lfloor {}^{L}/_{\lambda_2}\rfloor\right), \tag{5}$$

where L is the length of the polycapillary lens,

$$\lambda_1 = \sqrt{r_b^2-(r_b-d)^2)} \tag{6}$$

is the geometrically longest possible mean free path of an X-ray in a capillary with an inner diameter d, and bending radius r_b, which can be expressed as

$$r_b = \left(R_{max}-R_{in}\right)\frac{r_{in}}{R_{in}}/(1-\cos\left(\tan^{-1}(r_{in}/f_1)\right)), \tag{7}$$

where r_{max} is the maximum diameter of the capillary and f_1 the distance from X-ray source to the lens, and

$$\lambda_2 = \emptyset\cdot f_1/r_{spot} \tag{8}$$

is the mean free path of an X-ray with an incoming angle of ϕ inside a straight capillary with an inner diameter $\emptyset$. The geometry of a capillary, including λ_1 and λ_2, is illustrated in Fig. 2.

Equation (5) means that two scenarios are compared when considering how many collisions are happening: 1) the X-ray comes inside the capillary at a straight angle in which case the amount reflections depends only on the capillary geometry (λ_1), 2) the X-ray comes inside a straight capillary with angle defined by the position of X-ray emission (λ_2). Whichever case produces the larger amount of collisions is considered to happen.

Here we have assumed that each capillary looks directly to the center of the beam spot. We have also not taken into account X-rays that initially hit the walls of the capillaries but are not absorbed, find a channel and reach the detector.

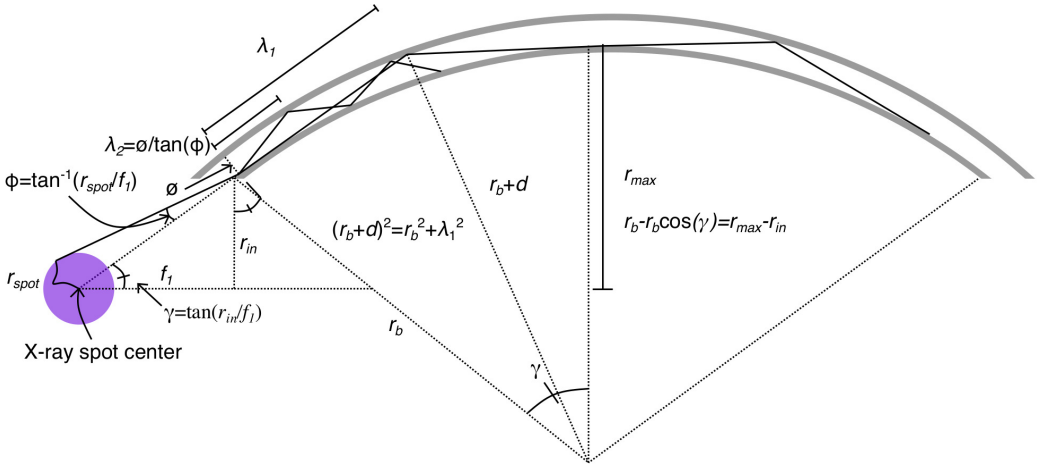

Figure 2: Geometry for an X-ray reflecting inside a capillary. The path with a minimum amount of reflections is defined by the parameter λ_1, and the number of reflections with incoming angle of ϕ is related to parameter λ_2.

2.2. X-ray transmission for different configurations of the polycapillary lens

The distance between the vacuum window of the transition-edge sensor array and the sample is 275 mm. In addition to the polycapillary lens, some X-ray absorbing matter are always present between the detector vacuum window and the sample. We are considering two general cases: a) an inert gas fills the whole 275 mm space (air or He), b) the polycapillary lens is placed in the vacuum, but a thin vacuum window (Be window or Si_3N_4 window) and small amount of inert gas (5 mm of air or He) is placed between the sample and the thin vacuum window.

We have divided the two general cases into five specific scenarios, and the X-ray transmission for the five scenarios are plotted in Fig. 3. The following scenarios are compared with each other: 1) 275 mm of He (flow) between the detector and the sample, 2) 275 mm of air between the detector and the sample, 3) 8 µm thick Be window before the polycapillary lens, the polycapillary lens in a vacuum and 5 mm of air between the Be window and the sample, 4) same as 3) but with 5 mm of He between the sample and the Be window, 5) same as 4) except a 200 nm thick Si_3N_4 vacuum window instead of the Be window. In all cases, the backscattered 2–3 MeV proton beam is stopped by the polycapillary lens, if it does not stop before it. Above 1.84 keV the highest transmission is obtained by using He, and below 1.84 keV the highest transmission is obtained with the polycapillary in a vacuum, a 200 nm thick Si_3N_4 vacuum window, and 5 mm of He between the sample and the vacuum window. Leaving the polycapillary lens in air is clearly not an option.

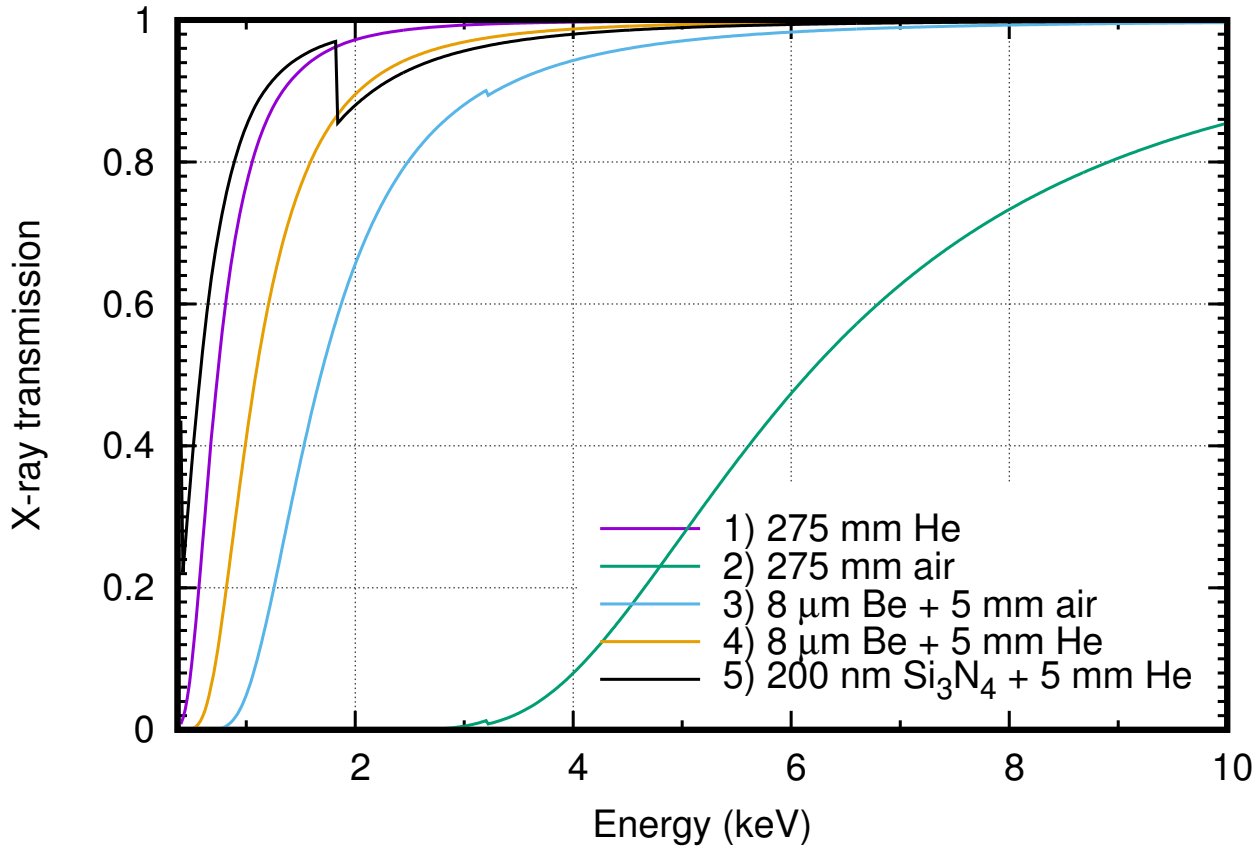

Figure 3: X-ray transmission of different possible scenarios in front of the transition-edge sensor with the polycapillary lens.

3. Experimental methods

3.1. Polycapillary lens for transition-edge sensor array

The current transition-edge sensor (TES) array at the University of Jyväskylä consists of 160 pixels with 305 µm x 320 µm collimated area on each. The array is cooled down to 100 mK by using an adiabatic demagnetization refrigeration (ADR), and sensors are voltage-biased to the transition between the superconducting and the normal state. Sensor current is read inductively using superconducting quantum interference devices (SQUID) with time-division multiplexing [27]. Pulse-shapes are saved and analyzed later on. In front of the TES array, there are three infrared filters, at 100 mK, 3 K and at 60 K, each with a composition of a 225 nm thick Al layer on top of

a 280 nm thick silicon nitride membrane. AP3.3 window from Moxtek Inc. is used for a vacuum window. A more detailed description of the detector can be found in Refs. [7, 8].

A polycapillary lens was designed in collaboration with IfG - Institute for Scientific Instruments GmbH and manufactured by IfG. The design properties for the polycapillary lens were: optimized efficiency in 0.5–8 keV energy range; the total length of a lens system, including focal lengths, 290–300 mm; optimized for a beam spot with a 0.5 mm diameter. A schematic picture with the polycapillary lens parameters is shown in Fig. 4. A photo of the encapsulated lens and two optical microscope images of capillaries are shown in Fig. 5.

The polycapillary lens alignment snout is kept in He atmosphere. A second option would to put the polycapillary lens alignment snout in vacuum, and to have a He flow between the sample and the vacuum window (see Fig 3). The chosen option has better X-ray transmission above 1.840 keV than the second option, has nearly as good transmission between 0.5 keV and 1.839 keV as the second option, has a simpler design, and has a better X-ray transmission when used in vacuum chamber configuration. Due to these reasons, the current design was chosen.

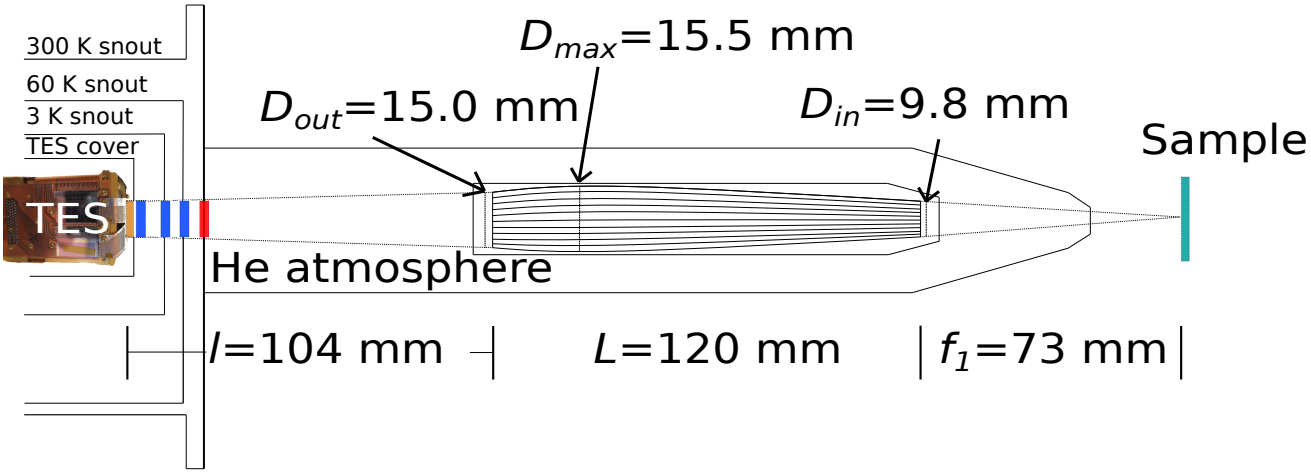

Figure 4: Definitions and values for the polycapillary lens parameters. The polycapillary lens is inside a metallic container, and the metallic container is inside a plastic polycapillary lens alignment snout. The polycapillary lens alignment snout has 8 screws to adjust the position and angle of the polycapillary lens, and He flows inside the alignment snout. Between the polycapillary and the detector there is AP3.3 vacuum window from Moxtek inc. (red line in the picture) and three infrared radiation (IR)-filters (blue lines in the picture), and the detector active area is highlighted with orange line. The picture is drawn in scale, except for D_{max} and TES snout structures were not drawn in scale for the clarity.

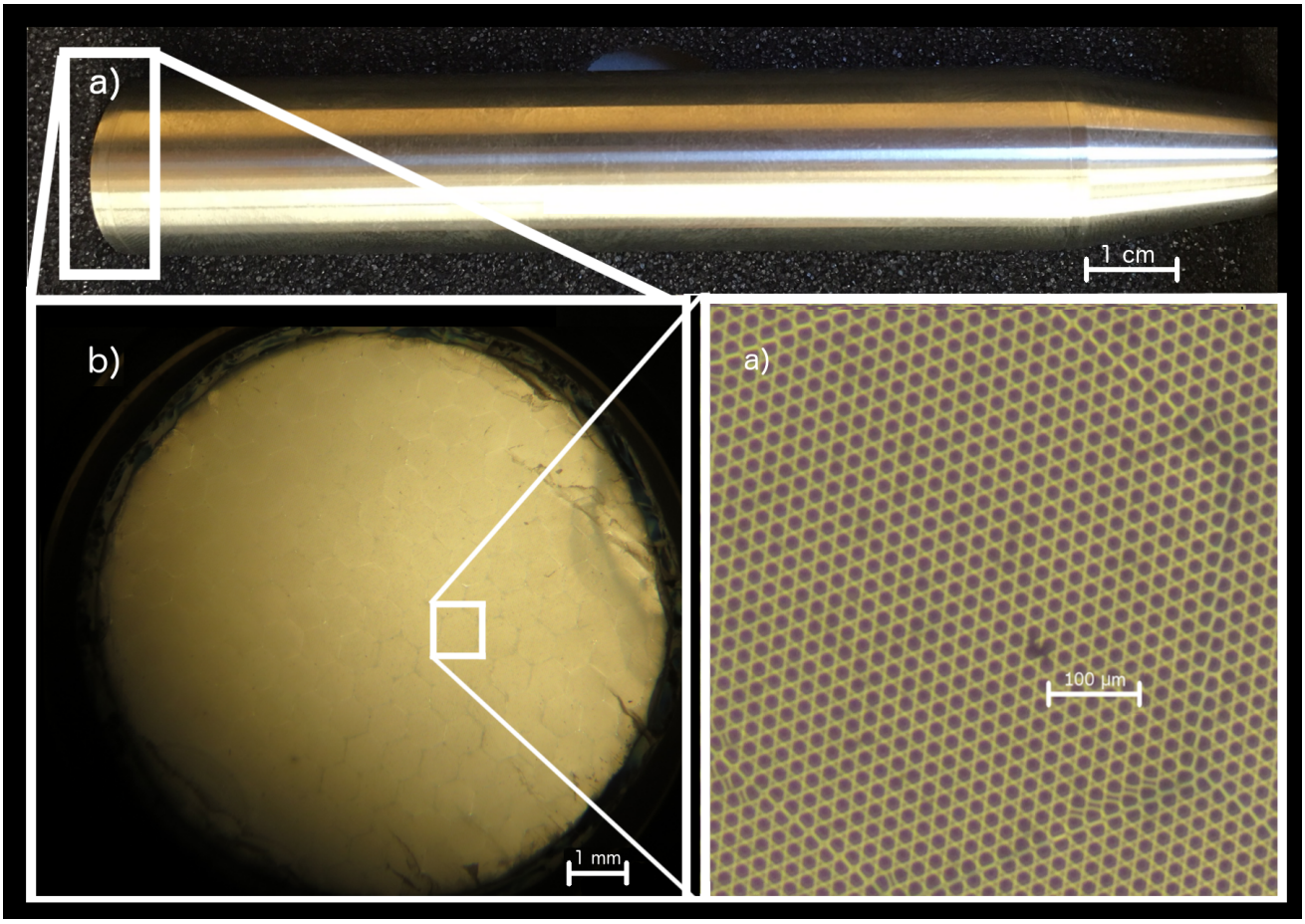

Figure 5: a) A side view of the polycapillary lens, b/c) cross-sectional optical microscope images of the polycapillary lens using two different magnifications.

3.2. New beamline for PIXE and RBS

We have built a new beamline which consists of a multi-purpose vacuum chamber followed by an external beam setup. The design of the new beamline is shown in Figures 6 and 7. The vacuum chamber can be used for both PIXE and Rutherford backscattering spectrometry (RBS) measurements, and the external beam is dedicated to PIXE measurements. High energy resolution PIXE can be done in both configurations.

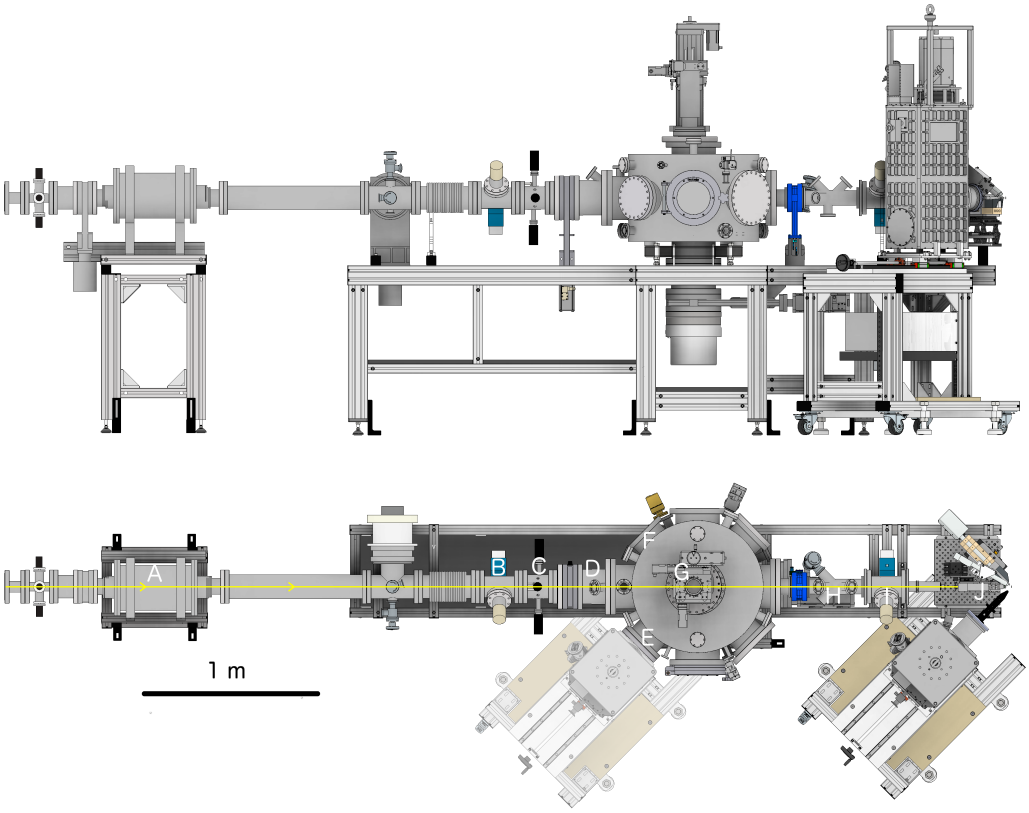

Figure 6: CAD-images of the new experimental PIXE setup at the University of Jyväskylä. In the images the ion beam comes from left to right (yellow line in the Figure). In the bottom image A = wobbler, B = beam profile meter (BPM), C = slits, D = chopper, E = mounting flange for the transition-edge sensor array, F = mounting flange for silicon drift detector or CdTe detector, G = goniometer, H = fluorescent screen, I = BPM, J = external beam setup, see Fig. 8.

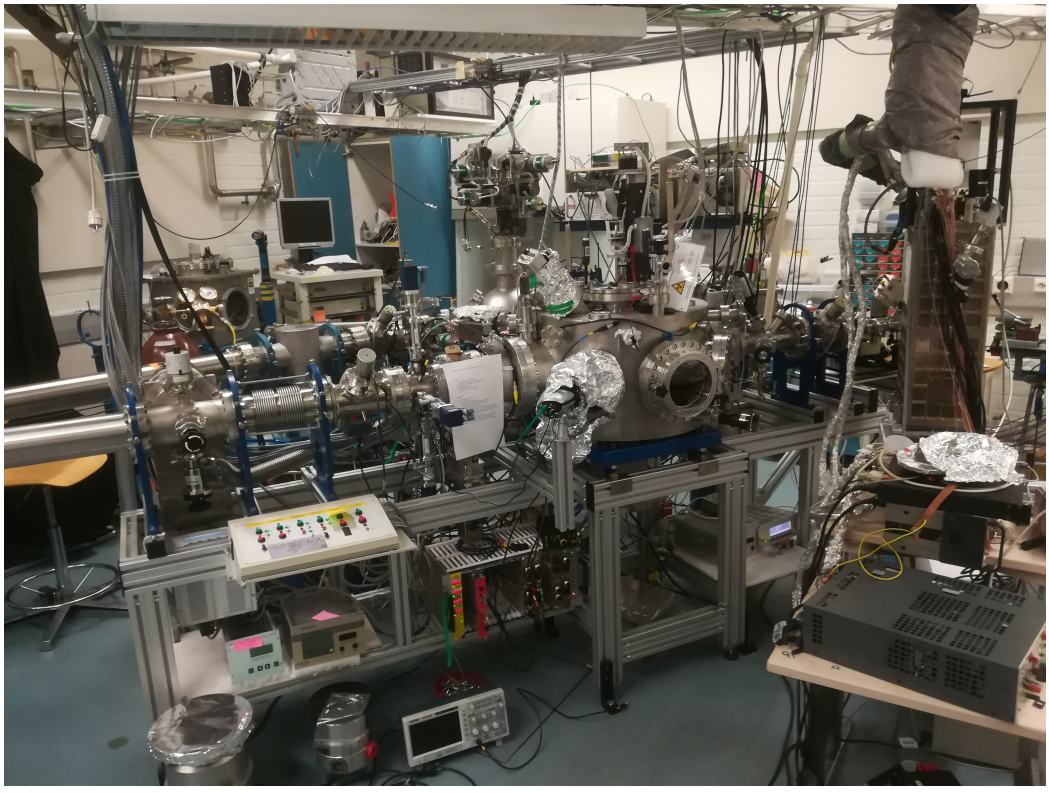

Figure 7: A picture of the finished beamline. The ion beam comes from left to right.

Table 1: Detector positions and alignments in the new external beam setup. The distances of the silicon drift detectors (SDD) can be adjusted to some degree. Here LE refers to a low energy detector, HE to a high energy detector and TES to the transition-edge sensor array.

Parameter	LE SDD	HE SDD	TES
Vertical plane angle	0 deg	30 deg	0 deg
Horizontal plane angle	45 deg	30 deg	45 deg
Distance to the sample surface	12.4 cm	3.5 cm	29.5 cm
Collimated area	50 mm^2	17 mm^2	15.616 mm^2
Absorbers	None	100 µm Be	3x(225 nm Al on 280 nm Si_3N_4)
Vacuum window	Moxtek AP3.3	Amptek C1	Moxtek AP3.3

3.2.1. External beam configuration

The external beam configuration includes the TES array and cryogenics for high energy resolution measurements, and two silicon drift detectors (SDD). The two SDDs are used for conventional PIXE measurements: one for low energy region (Ketek AXAS-D H50LE), and the other for high energy region (Amptek X-123SDD). Helium flow is used for both the TES array polycapillary and the low energy detector (Ketek). Visible light is blocked from LE detector by light-tight window from HS foils (250 nm Al on 145 nm Si_3N_4 on silicon grid with 81% open area). Third SDD (Ketek AXAS-D H30) is looking at the exit window (Si_3N_4), and beam intensity in PIXE measurements is normalized using Si K X-rays from the exit window [28]. The external beam geometry is visualized in Fig. 8.

The distance between the sample surface and the exit window is 2.2 cm, the distance between the polycapillary lens entrance and the sample is 7.3 cm and the distance between the polycapillary lens alignment snout and the sample is 0.5 cm. More details of the detector geometry are listed in Table 1. The combination of three different detectors optimized for both high and low energy X-rays makes the external beam the preferred option for PIXE measurements for most samples.

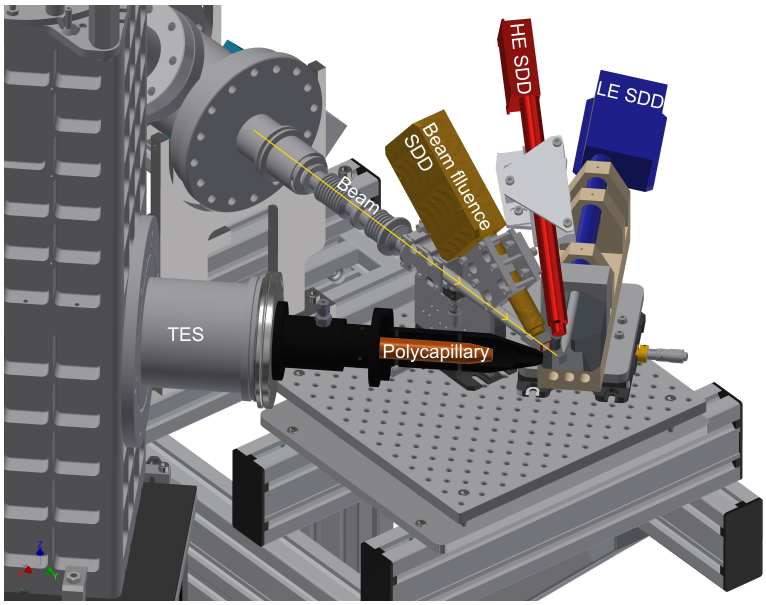

Figure 8: A CAD-image of the new external beam setup at the University of Jyväskylä. In the image positions of the transition-edge sensor (TES) array, detector monitoring beam fluence (beam fluence SDD), low energy detector (LE SDD), high energy detector (HE SDD), the polycapillary lens alignment snout (black), and the metallic polycapillary container (red) are shown.

3.2.2. Vacuum chamber configuration

In the vacuum chamber setup, we have two partially depleted passivated implanted planar silicon (Canberra PIPS®PD50-11-300 AM) detectors for Rutherford backscattering spectrometry (RBS). For PIXE, SDD (Amptek X-123SDD) and TES are used. The silicon drift detector is the same detector that is used in the external beam configuration. A CdTe (Amptek XR-100T, 25 mm^2 active area at a 36.6 cm distance from the sample surface) detector can be used for detecting high-energy X-rays or gamma-rays if required. The beam fluence is calibrated by using a chopper before the chamber. The RBS spectrum of the backscattered beam from the chopper is monitored using a 300 mm^2 silicon detector. The detector geometries are listed in Table 2. It should be noted that the

Table 2: Detector positions and alignments in the new vacuum chamber setup. All detectors are on the same vertical plane as the incoming ion beam. PIPS®detectors are used for detecting the scattered ions.

Parameter	PIPS®	PIPS®	SDD	TES
Detection angle	170 deg	$0 - 165$ deg	-135 deg	135 deg
Distance to the sample surface	10.1 cm	9.8 cm	18.2 cm	29.5 cm
Active area	50 mm^2	50 mm^2	17 mm^2	15.616 mm^2
Absorbers	None	None	100 µm Be	3x(225 nm Al on 280 nm Si_3N_4)
Vacuum window	None	None	Amptek C1	Moxtek AP3.3

polycapillary lens can be used in this configuration as well. Since the polycapillary lens stops the scattered beam, no additional filters are needed, and it is possible to see low energy X-rays even better than under He flow.

This configuration is used mainly for RBS measurements and can be used for PIXE measurements as well. The advantage of this configuration is simultaneous PIXE-RBS data collection. In this vacuum chamber, heavy-ion PIXE measurements for chemical speciation [29, 30] can be performed using the TES array.

3.3. Experimental X-ray transmission of the polycapillary lens

For determining the X-ray transmission of the polycapillary lens, we have measured two samples: an in-house prepared calibration sample and the NIST (National Institute of Standards and Technology) standard reference material SRM 611. The in-house prepared calibration sample contains the following films from top to bottom on a C substrate: 14 nm Al, 10 nm Nb, 25 nm Ag, 65 nm Ti, 115 nm Fe, 185 nm Ni, 300 nm Cu and 70 nm Cr. All films were deposited using electron beam evaporation. We used libCPIXE [31] for simulating a composition producing uniform distribution of X-ray energies in 1–8 keV range with 1.6–3.0 MeV proton beam. The nominal composition of SRM 611 matrix is 72% SiO_2, 14%Na_2O, 12%CaO, 2%Al_2O_3, and the sample has over 50 added elements at approximately 500 ppm level.

Two measurement sets for both samples were carried out. First, the samples were measured in the external beam configuration (as described in section 3.2) with the polycapillary lens installed. The second set of measurements were done in otherwise identical configuration, except the polycapillary lens was not installed (but the polycapillary lens alignment snout was still in place). Count rate in the detector measuring the beam fluence was similar in both measurements (1000–3000 counts/s).

In all measurements, 2010 keV initial proton beam energy was chosen to ensure that the proton beam stops before the detector even without the polycapillary lens. The IR-filters are able to stop 270 keV protons, and most of the energy loss takes place in the helium. With 275 mm thick helium volume and three IR filters (225 nm Al, 280 nm Si_3N_4 each) 1.6 MeV protons are stopped. By taking into account the energy loss in the air between the sample and the exit window, protons accelerated to 2.01 MeV energy are stopped. The stopping calculations were performed using SRIM-2013 [32].

3.4. Theoretical X-ray transmission of the polycapillary lens

In order to calculate the theoretical performance of the polycapillary lens, we measured the beam spot dimensions, and the polycapillary lens dimensions not shown in Fig. 4. Measurements were performed in the external beam configuration.

The beam spot profile was measured using a narrow copper wire with a diameter of 0.30 mm. The measurement was done with two different exit-window to sample distances, 17 mm (first measurement) and 21 mm (second measurement), in order to see if the beam spot size and shape stays the same at different distances. The measured X-ray intensity as a function of offset from the beam center is shown in Fig 9. The X-rays from the copper wire were measured using the high-energy SDD. The beam spot was fitted with a normal distribution, and the full-width at half-maximum values (FWHM) (0.54 ± 0.02) mm and (0.47 ± 0.02) mm were fitted. The copper wire diameter was taken into account in the fitting, and the reported FWHM values are the FWHMs of the beam spot, not the FWHMs of the measured intensity. In the second fit (at 21 mm) three points are clearly not on the fitted line. These three points were measured in the beginning, so some kind of misalignment in the measurements might have happened which went unnoticed.

The FWHM in the second measurement is smaller even though the beam was further away from the exit window. The following reasoning could explain this. The first measurement took 2 h 20 minutes, and during the measurement all accelerator parameters were unchanged. At the beginning of the measurement, the accelerator tends to be less stable and the terminal voltage can drift very slightly which makes the beam spot look wider in a long measurement. The second measurement was shorter (1 h 40 min) and also the terminal voltage was more stable. In the measurements of the in-house fabricated and NIST SRM 611 samples, both took a total of 2

hours 50 minutes to measure, so the situation resembled more the situation in the first beam spot measurement. Therefore, in the calculations the value of 0.535 mm was used for the full-width at half-maximum of the beam spot.

In order to see the 2D-shape of the beam, a white copying paper was radiated with a beam until a spot visible for the naked eye could be observed. The produced spot had a circular shape, following the exit aperture shape, and circular shape was thus used in the calculations.

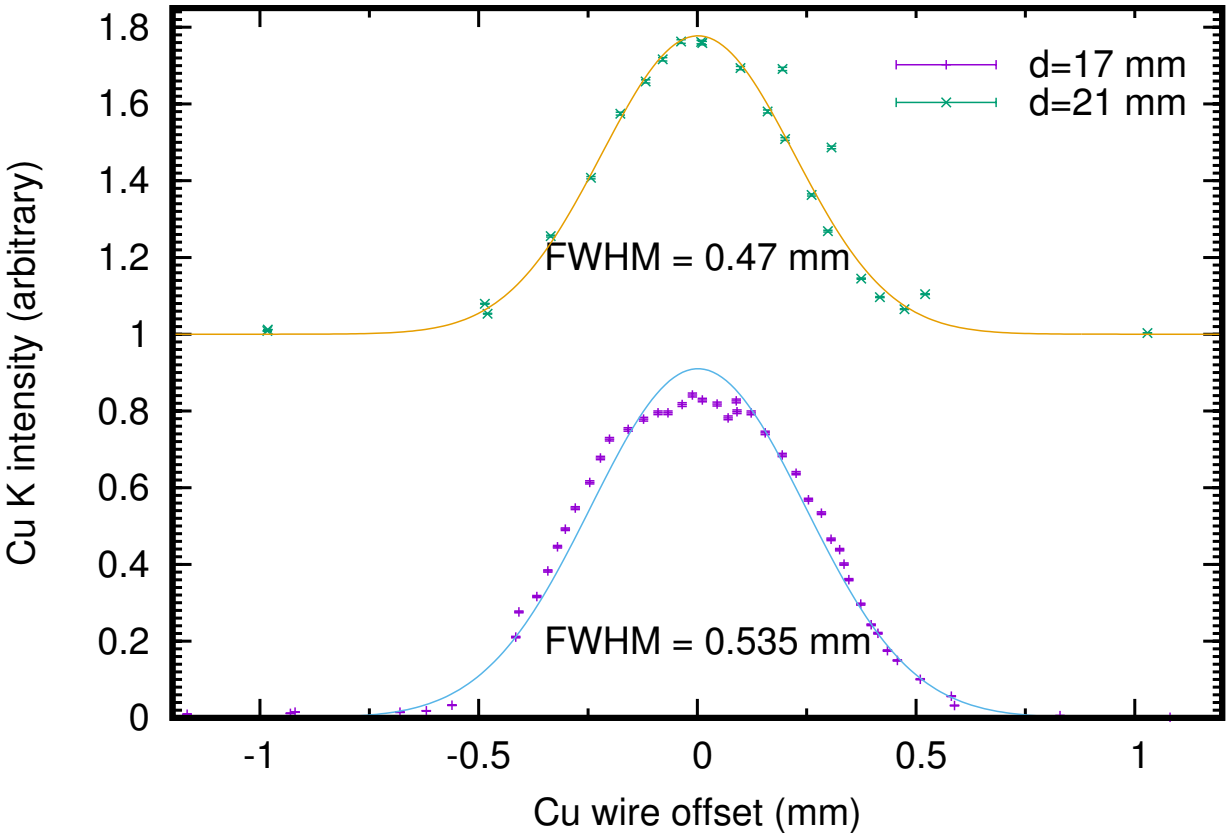

Figure 9: The measured Cu Kα intensity with two different exit-window to sample distances, 17 mm and 21 mm. The beam spot was measured using a narrow 0.3 mm diameter copper wire. The finite size of the copper wire is included in the fit, and the reported FWHM is the FWHM of the beam spot, not the FWHM of the fit function.

The polycapillary lens was imaged with an optical microscope as shown in Fig. 5. From these images, the inner diameter of a single capillary was determined to be 15.5 µm, and the open area fraction was 55%.

Combining these measured dimensions with other known lens dimensions, we calculated the theoretical gain using Equation (2). The integration of the beam spot was done over 3 full-widths at half-maximum. The calculated gain and experimental gain are shown later in Fig. 12. For the borosilicate glass (capillary material) four different compositions were used: 1) 81% SiO_2, 13% B_2O_3, 2% Al_2O_3, 2% Ca_2O, 2% K_2O; 2) 65% SiO_2, 25% B_2O_3, 2% Ca_2O, 8% K_2O; 3) 80.9% SiO_2, 13% B_2O_3, 2% Al_2O_3, 2% Ca_2O, 2% K_2O, 0.1% Pb; 4) same composition as 1) but with 1.3 nm roughness (all values are in mass percentages). The values for X-ray reflectivity were calculated with the Fresnel equation [26], X-ray atomic fractions reported by Henke et al. [26] were used, and the Nevot-Croce factor was used to calculate the effect of roughness [33]. A density of borosilicate 2.23 $\frac{\mathrm{g}}{\mathrm{cm}^3}$ was used for the simulations.

4. Results and Discussion

The measured X-ray spectra of NIST SRM 611 with and without the polycapillary lens are plotted in Fig. 10, and the spectra of the in-house prepared calibration sample are plotted in Fig. 11. Both samples were measured in the external beam configuration. The polycapillary lens stops the backscattered protons and no additional proton filter is needed, the use of helium atmosphere gives a good X-ray transmission, and as a result of these two, we were able to detect O Kα X-rays in the external beam setup (Fig. 10). We were not able to detect C Kα X-rays from the substrate of the in-house prepared calibration sample (Fig. 11). The X-ray transmission for C Kα X-rays

through the IR-filters ($2.79 \cdot 10^{-6}$ [26]) and AP3.3 vacuum window (0.47) is 1.3e-6. Thus, we do not expect to detect C Kα X-rays either in vacuum or external beam setup. The X-ray transmission for N Kα X-rays through the IR-filters and AP3.3 vacuum window (0.31) is 10^{-3} and when adding 275 mm He it is $6.3 \cdot 10^{-6}$. Thus, N or lighter elements cannot be detected in the external beam configuration, and in the vacuum chamber configuration the lightest detectable element is either N or O. X-rays from oxygen and lighter elements are absorbed easily in the measured material itself, and quantitative analysis of these elements with PIXE is problematic, and better to be done for methods like elastic recoil detection analysis (ERDA). The low energy region 0.5–1.0 keV is thus sufficient enough for qualitative analysis only.

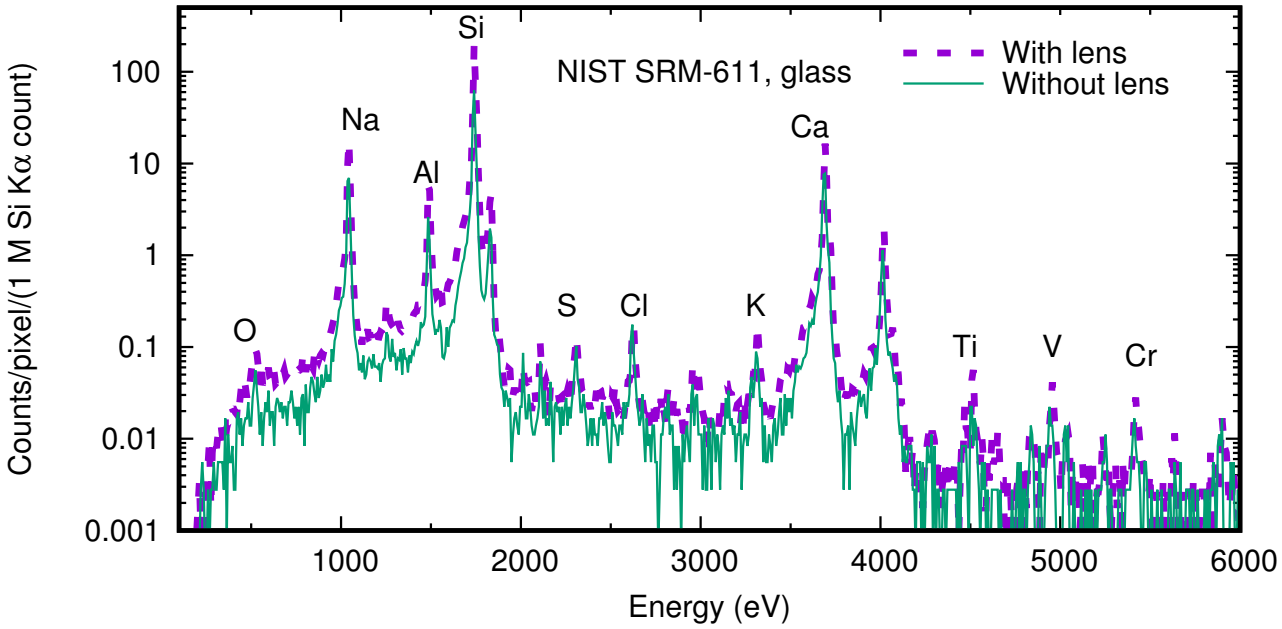

Figure 10: Measured X-ray spectra of NIST SRM 611 with 72% SiO_2, 14% Na_2O, 12% CaO, 2% Al_2O_3 nominal matrix composition. Intensity is scaled to counts per pixel per million counts in Si Kα peak area measured from the beam exit window. The dead time of the TES and the dead time of the beam fluence calibration detector are taken into account. In the spectra, 8 eV bin width is used for clarity.

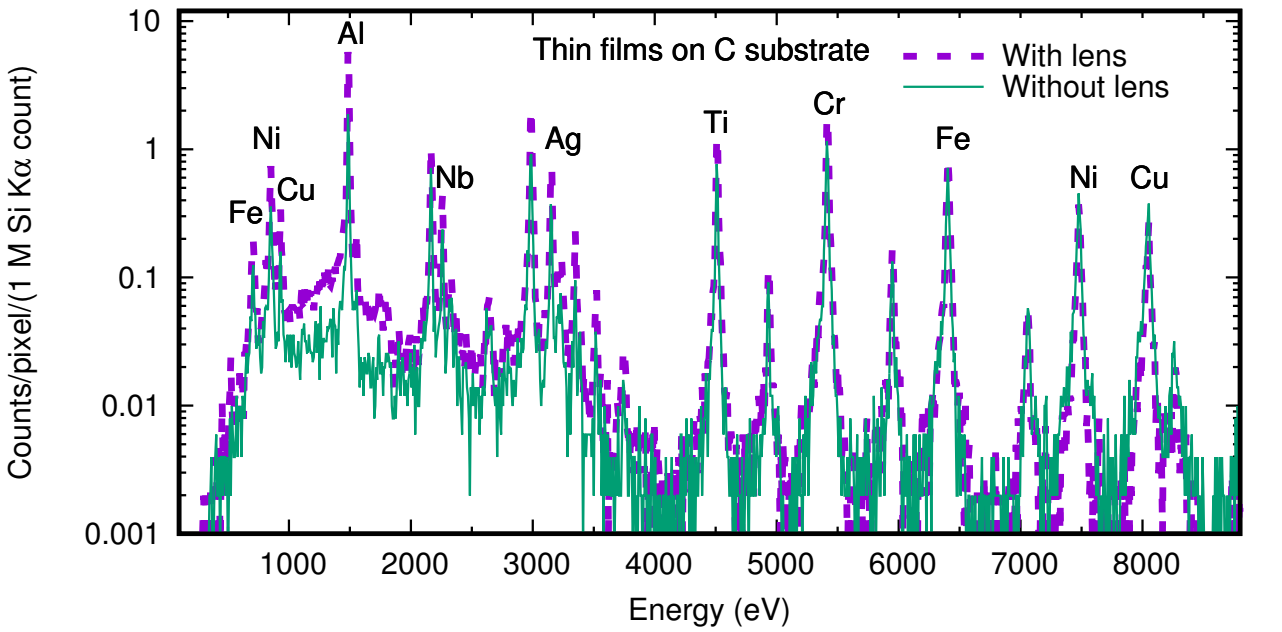

Figure 11: Measured X-ray spectra of a calibration sample with Al, Nb, Ag, Ti, Cr, Fe, Ni, Cu thin films on top of C substrate. Intensity is scaled to counts per pixel per million counts in Si Kα peak area measured from the beam exit window. The dead time of the TES and the dead time of the beam fluence calibration detector are taken into account.

The experimental and theoretical gains for the polycapillary lens are shown in Figure 12. The measured gain stays between 1.5 and 3.0 at energies from 0.5 keV to 5.5 keV, and drops below 1 at energies >7 keV. All the calculations have very similar shape below 1.8 keV, and agree well with the experimental data points. At 2–4 keV energy range the composition 2) agrees best with the data, and at energies above 4 keV all calculations fit decently to the experimental data, but the composition 2) producing gain a bit below the experimental data. The difference between compositions 1), 3), and 4) (otherwise identical composition, but 3) has 0.1% lead added and 4) has 1.3 nm RMS roughness) is quite small. It should be also noted, that some X-rays might initially hit the capillary glass without absorbing into it, and can reach the detector. This was not taken into account in the calculations. Hitting the capillary glass without absorption in the glass is more likely at higher energies, which can explain the slight deviation of the calculated values at 7.48 keV and 8.05 keV. Overall, composition 2) gives the best agreement with the experimental data, because the higher amount K_2O causes a sudden drop in intensity at 3.607 keV, which is also seen in the experiments.

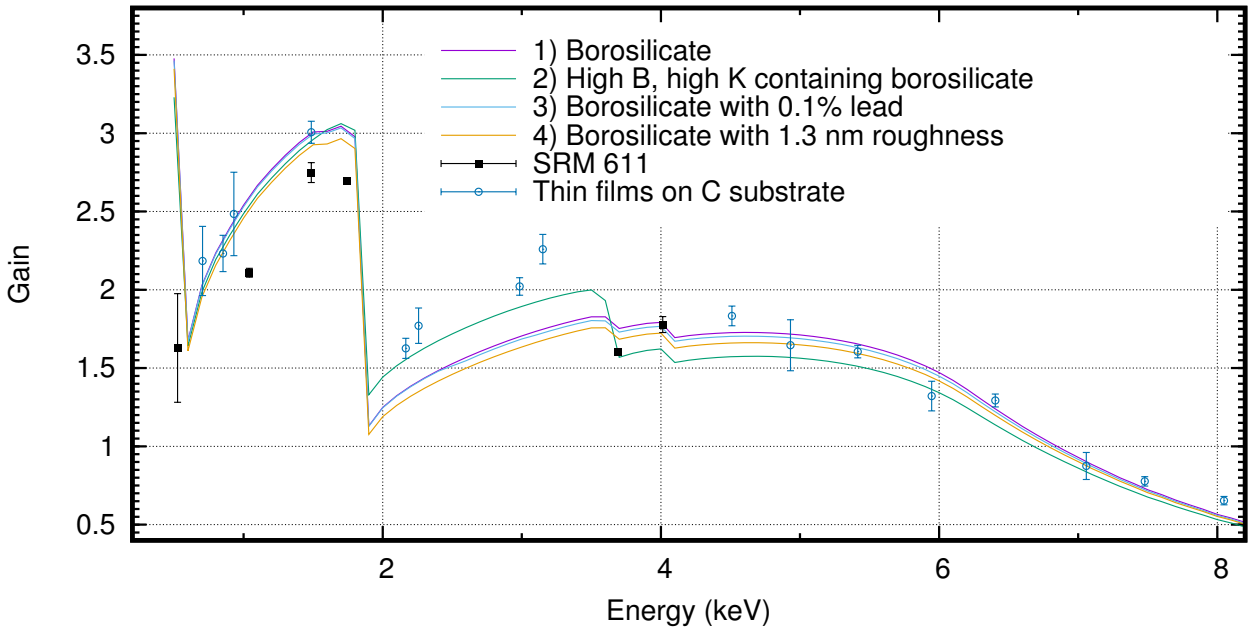

Figure 12: Measured and calculated X-ray gain for the polycapillary lens. For the theoretical calculations four different compositions for the glass material were used: 1) 81% SiO_2, 13% B_2O_3, 2% Al_2O_3, 2% Ca_2O, 2% K_2O; 2) 65% SiO_2, 25% B_2O_3, 2% Ca_2O, 8% K_2O, 3) same as 1), but with additional 0.1% Pb, 4) same as 1) but with 1.3 nm RMS roughness (all values in mass percentages).

Between 0.5–6 keV the measured gain stays between 1.5 and 3.0. In order to get a similar factor of two intensity increase without the polycapillary lens, we would need twice as big solid angle, so the detector should be at a closer distance of circa 210 mm. With the current setup the limiting factor is the TES table, and the TES array can be brought to a distance 225 mm at closest in the external beam configuration. The smallest possible detector-to-sample distance limited by the ADR-unit (and ignoring the supporting structures) at 135 degrees detector angle would be 92 mm, a factor of 10 increase in solid angle compared to 295 mm detector-to-sample distance. However, moving the detector this close to the sample would require a proton filter. Because the TES are extremely sensitive devices to external magnetic field [19], magnetic deflection is not desirable. For example, a 100 µm Be filter could be used to stop protons up to 3 MeV energies. A 100 µm Be filter has transmission less than 20% at 1.9 keV [26] and at energies below this the polycapillary becomes clearly beneficial. This low-energy region is interesting for our detector for few reasons. The energies we can detect are limited to roughly below 10 keV, and good efficiency below 2 keV is necessary for detecting elements with Kα over 10 keV and Lα below 2 keV (elements with $31 \leq Z \leq 39$). The energy response of our detector is less linear at higher energies (roughly >6 keV), making the lower energy X-ray lines more preferred for the analysis for elements with high energy K-lines (such as Ge, Ga or As) or high-energy L-lines (such as Au or Pb). Polycapillary lens can also be used in vacuum chamber configuration, making it the preferred option for our system.

In Figure 13 the total amount of good pulses (measured from the NIST SRM 611 sample) are shown for each pixel a) with the polycapillary lens, b) without the polycapillary lens. Same active pixels were used in both measurements. With the polycapillary lens, the X-rays are less homogeneously distributed. In every corner there are pixels with large amount of pulses with the polycapillary lens, which indicates that the actual focus of the polycapillary is inhomogenous instead of issues with the polycapillary alignment.

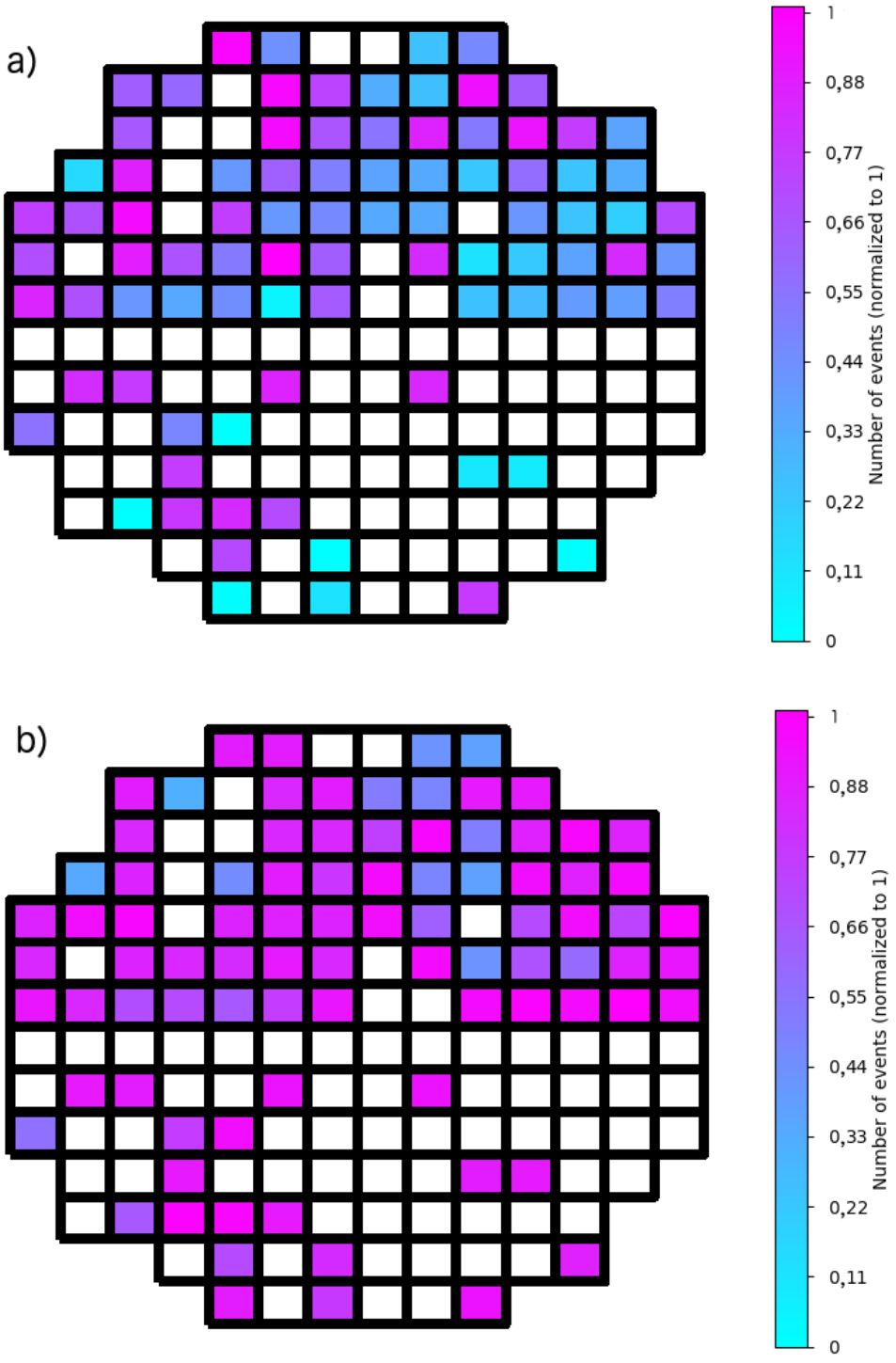

Figure 13: Measured pulses from NIST SRM 611 sample for each active pixel a) with the polycapillary lens and b) without the polycapillary lens. White pixels were not producing data during the measurement (n=54) or they were disregarded from the analysis due to bad data (n=18). The pixel with the highest amount counts is normalized to one. With the polycapillary lens, the X-rays are less homogeneously distributed among the pixels.

5. Summary

A polycapillary lens was installed for high energy resolution, energy-dispersive PIXE measurements. Measurements can be done in a vacuum or with an external beam, and the lightest element that can be detected now is oxygen, whereas previously it has been aluminium [8]. The polycapillary lens can be used also in the vacuum chamber. The limiting factor for detecting lower energies is the X-ray absorption in the IR-filters (a total of

675 nm Al and 840 nm Si_3N_4). The X-ray transmission through the polycapillary lens was measured at energies 0.5–8 keV. The agreement with the theoretical calculations and experimental data was good.

Acknowledgements

This work was partly funded by the Academy of Finland Centre of Excellence in Nuclear and Accelerator Based Physics (Ref. 251353). J. Tuunanen and J. Ihanainen are acknowledged for their contribution to the CAD designs of the new beamline. Helpful discussions with the NIST Boulder Quantum Sensors group are acknowledged.

References

[1] T. B. Johansson, R. Akselsson, and S. A. E. Johansson. X-ray analysis: Elemental trace analysis at the 10^{-12} g level. *Nuclear Instruments and Methods*, 84(1):141–143, 1970.

[2] T. Calligaro, J. D. MacArthur, and J. Salomon. An improved experimental setup for the simultaneous PIXE analysis of heavy and light elements with a 3 MeV proton external beam. *Nuclear Instruments and Methods in Physics Research Section B: Beam Interactions with Materials and Atoms*, 109-110:125–128, 1996.

[3] P. Tesauro, P. A. Mandò, G. Parrini, A. Pecchioli, and P. Sona. A compact flat-crystal X-ray spectrometer for external beam PIXE measurements. *Nuclear Instruments and Methods in Physics Research Section B: Beam Interactions with Materials and Atoms*, 108(1):197–204, 1996.

[4] K. Maeda, K. Hasegawa, H. Hamanaka, and M. Maeda. Chemical state analysis in air by high-resolution PIXE. *Nuclear Instruments and Methods in Physics Research Section B: Beam Interactions with Materials and Atoms*, 136–138:994–999, 1998.

[5] K Maeda, A Tonomura, H Hamanaka, and K Hasegawa. Chemical shift measurements of PIXE spectra using a position-sensitive crystal spectrometer. *Nuclear Instruments and Methods in Physics Research Section B: Beam Interactions with Materials and Atoms*, 150(1–4):124–128, 1999.

[6] K. Maeda, K. Hasegawa, M. Maeda, K. Ogiwara, and H. Hamanaka. Rapid chemical state analysis in air by highly sensitive high-resolution PIXE using a v. Hamos crystal spectrometer. *X-Ray Spectrometry*, 34(4):389–392, 2005.

[7] M. R. J. Palosaari, K. M. Kinnunen, J. Julin, M. Laitinen, M. Napari, T. Sajavaara, W. B. Doriese, J. Fowler, C. Reintsema, D. Swetz, D. Schmidt, J. Ullom, and I. J. Maasilta. Transition-Edge Sensors for Particle Induced X-ray Emission Measurements. *Journal of Low Temperature Physics*, 176(3-4):285–290, 2013.

[8] M. R. J. Palosaari, M. Kayhko, K. M. Kinnunen, M. Laitinen, J. Julin, J. Malm, T. Sajavaara, W. B. Doriese, J. Fowler, C. Reintsema, D. Swetz, D. Schmidt, J. N. Ullom, and I. J. Maasilta. Broadband Ultrahigh-Resolution Spectroscopy of Particle-Induced X Rays: Extending the Limits of Nondestructive Analysis. *Physical Review Applied*, 6(2):024002, 2016.

[9] M. Käyhkö, M. R. J. Palosaari, M. Laitinen, K. Arstila, I. J. Maasilta, J. W. Fowler, W. B. Doriese, J. N. Ullom, and T. Sajavaara. Minimum detection limits and applications of proton and helium induced X-ray emission using transition-edge sensor array. *Nuclear Instruments and Methods in Physics Research Section B: Beam Interactions with Materials and Atoms*, 406:130–134, 2017.

[10] M. A. Reis, L. C. Alves, N. P. Barradas, P. C. Chaves, B. Nunes, A. Taborda, K. P. Surendran, A. Wu, P. M. Vilarinho, and E. Alves. High resolution and differential PIXE combined with RBS, EBS and AFM analysis of magnesium titanate (MgTiO3) multilayer structures. *Nuclear Instruments and Methods in Physics Research Section B: Beam Interactions with Materials and Atoms*, 268(11–12):1980–1985, 2010.

[11] M. A. Reis, P. C. Chaves, and A. Taborda. Radiative auger emission satellites observed by microcalorimeter-based energy-dispersive high-resolution PIXE. *X-Ray Spectrometry*, 40(3):141–146, 2011.

[12] P. C. Chaves, A. Taborda, J. P. Marques, and M. A. Reis. H+ and he2+ induced w l x-rays intensity ratios: part i, si(li) data and eds high resolution insight. *X-Ray Spectrometry*, 42(3):141–150, 2013.

[13] P. C. Chaves, A. Taborda, J. P. Marques, and M. A. Reis. N to k uranium PIXE spectra obtained at the high resolution high energy PIXE setup. *Nuclear Instruments and Methods in Physics Research Section B: Beam Interactions with Materials and Atoms*, 318, Part A:60–64, 2014.

[14] M. A. Reis, P. C. Chaves, and A. Taborda. Review and perspectives on energy dispersive high resolution PIXE and RYIED. *Applied Spectroscopy Reviews*, 52(3):231–248, 2016.

[15] M. Kavcic, A. G. Karydas, and Ch. Zarkadas. Chemical state analysis employing sub-natural linewidth resolution PIXE measurements of kα diagram lines. *X-Ray Spectrometry*, 34(4):310–314, 2005.

[16] M. Kavčič, M. Petric, and K. Vogel-Mikuš. Chemical speciation using high energy resolution PIXE spectroscopy in the tender X-ray range. *Nuclear Instruments and Methods in Physics Research Section B: Beam Interactions with Materials and Atoms*, 417:65–69, 2018.

[17] R. Alberti, A. Bjeoumikhov, N. Grassi, C. Guazzoni, T. Klatka, A. Longoni, and A. Quattrone. Use of silicon drift detectors for the detection of medium-light elements in PIXE. *Nuclear Instruments and Methods in Physics Research Section B: Beam Interactions with Materials and Atoms*, 266(10):2296–2300, 2008.

[18] G. M. Stiehl, H. M. Cho, G. C. Hilton, K. D. Irwin, J. A. B. Mates, C. D. Reintsema, and B. L. Zink. Time-Division SQUID Multiplexers With Reduced Sensitivity to External Magnetic Fields. *IEEE Transactions on Applied Superconductivity*, 21(3):298–301, 2011.

[19] S. Zhang, M. E. Eckart, F. T. Jaeckel, K. L. Kripps, D. McCammon, K. M. Morgan, and Y. Zhou. Mapping of the resistance of a superconducting transition edge sensor as a function of temperature, current, and applied magnetic field. *Journal of Applied Physics*, 121(7):074503, 2017.

[20] D. A. Wollman, K. D. Irwin, G. C. Hilton, L. L. Dulcie, D. E. Newbury, and J. M. Martinis. High-resolution, energy-dispersive microcalorimeter spectrometer for x-ray microanalysis. *Journal of Microscopy*, 188(3):196–223, 1997.

[21] K. Maehata, K. Idemitsu, and K. Tanaka. X-ray energy dispersive spectroscopy of uranium ore using a TES microcalorimeter mounted on a field-emission scanning electron microscope. *Nuclear Instruments and Methods in Physics Research Section A: Accelerators, Spectrometers, Detectors and Associated Equipment*, 648(1):285–289, 2011.

[22] A. Takano, K. Maehata, N. Iyomoto, T. Hara, K. Mitsuda, N. Yamasaki, and K. Tanaka. X-Ray Transmission Characteristic Measurements of Polycapillary Optics Installed in an Analytical Electron Microscope. *Nuclear Science, IEEE Transactions on*, 62(4):1918–1922, 2015.

[23] A. Takano, K. Maehata, N. Iyomoto, K. Yasuda, H. Maeno, K. Shiiyama, and K. Tanaka. Characterization of Polycapillary Optics in a TES Microcalorimeter EDS System Installed on an SEM. *Journal of Low Temperature Physics*, 184(3-4):832–838, 2016.

[24] K. Maehata, T. Hara, K. Mitsuda, M. Hidaka, K. Tanaka, and Y. Yamanaka. A Transition Edge Sensor Microcalorimeter System for the Energy Dispersive Spectroscopy Performed on a Scanning-Transmission Electron Microscope. *Journal of Low Temperature Physics*, 184(1-2):5–10, 2016.

[25] C. A. MacDonald. Focusing Polycapillary Optics and Their Applications. *X-Ray Optics and Instrumentation*, (867049), 2010. DOI: 10.1155/2010/867049.

[26] B. L. Henke, E. M. Gullikson, and J. C. Davis. X-Ray Interactions: Photoabsorption, Scattering, Transmission, and Reflection at E = 50-30,000 eV, Z = 1-92. *Atomic Data and Nuclear Data Tables*, 54(2):181–342, 1993.

[27] W. B. Doriese, J. A. Beall, S. Deiker, W. D. Duncan, L. Ferreira, G. C. Hilton, K. D. Irwin, C. D. Reintsema, J. N. Ullom, L. R. Vale, and Y. Xu. Time-division multiplexing of high-resolution x-ray microcalorimeters: Four pixels and beyond. *Applied Physics Letters*, 85(20):4762, 2004.

[28] J. C. Dran, J. Salomon, T. Calligaro, and P. Walter. Ion beam analysis of art works: 14 years of use in the Louvre. *Nuclear Instruments and Methods in Physics Research Section B: Beam Interactions with Materials and Atoms*, 219-220:7–15, 2004.

[29] M. Uda, O. Benka, K. Fuwa, K. Maeda, and Y. Sasa. Chemical effects in PIXE spectra. *Nuclear Instruments and Methods in Physics Research Section B: Beam Interactions with Materials and Atoms*, 22(1):5–12, 1987.

[30] M. Kayhko, M. R. J. Palosaari, M. Laitinen, K. Arstila, I. Maasilta, and T. Sajavaara. Heavy ion induced ti x-ray satellite structure for ti, tin, and tio_2 thin films. *X-Ray Spectrometry (in peer-review)*, 2018.

[31] C. Pascual-Izarra, N. P. Barradas, and M. A. Reis. LibCPIXE: A PIXE simulation open-source library for multilayered samples. *Nuclear Instruments and Methods in Physics Research Section B: Beam Interactions with Materials and Atoms*, 249(1):820–822, 2006.

[32] J. F. Ziegler, M. D. Ziegler, and J. P. Biersack. SRIM – The stopping and range of ions in matter (2010). *Nuclear Instruments and Methods in Physics Research Section B: Beam Interactions with Materials and Atoms*, 268(11–12):1818–1823, 2010.

[33] L. Névot and P. Croce. Caractérisation des surfaces par réflexion rasante de rayons X. Application à l'étude du polissage de quelques verres silicates. *Revue de Physique Appliquée*, 15(3):761–779, 1980.